MIRA: a multi-physics approach to designing a fusion power plant

OPEN ACCESS
IOP Publishing | International Atomic Energy Agency Nuclear Fusion
Nucl. Fusion **62** (2022) 076042 (33pp) https://doi.org/10.1088/1741-4326/ac6433

MIRA: a multi-physics approach to designing a fusion power plant

F. Franza[1,*], L.V. Boccaccini[1], E. Fable[2], I. Landman[1], I.A. Maione[1], S. Petschanyi[1], R. Stieglitz[1] and H. Zohm[2]

[1] Karlsruhe Institute of Technology (KIT), Karlsruhe, Germany
[2] Max-Plank Institute for Plasma Physics (IPP), Garching, Germany

E-mail: fabrizio.franza@kit.edu

Received 23 December 2021, revised 14 February 2022
Accepted for publication 5 April 2022
Published 10 June 2022

Abstract

Fusion systems codes (SCs) are deployed to produce the baseline of the European fusion power reactor (DEMO) within its conceptual design. A DEMO baseline is mostly defined by a radial/vertical reactor sketch and major reactor parameters, such as fusion and net electric power, magnetic fields, and plasma burn time. A baseline shall also meet a set of prescribed reactor requirements, constraints, and architectural features. According to the conceptual design workflow implemented within the EU-DEMO programme, the output from the SC is transferred to the detailed physics and engineering design codes. Presently-available fusion SCs rely on rather basic physics and engineering models (mostly at zero or one-dimensional level). The design codes, instead, are very detailed but run on much longer computing times. To fill the gap between systems and design codes, the multi-fidelity systems/design tool modular integrated reactor analysis (MIRA)—has been recently developed. MIRA incorporates the physics and the engineering insights of the utmost domains of tokamak reactors and relies on a higher spatial resolution, spanning from 1D up to 3D modelling frames. The MIRA approach has been applied to the DEMO 2017 baseline, generated by the EU reference SC PROCESS and used as input to MIRA. In the paper, the architectural and mathematical insights of the MIRA package are described, along with an EU-DEMO 2017 baseline analysis.

Keywords: DEMO, fusion reactor, systems code, reactor design, MIRA

(Some figures may appear in colour only in the online journal)

1. Introduction

The development of the demonstration power plant DEMO is foreseen after ITER towards the realization of a commercial fusion power plant (FPP). DEMO is required to feature all key systems and components of an FPP and to comply with a set of general goals [1]. These goals include a few hundred megawatts of electric power generation, a closed fuel cycle, and a long pulse (or steady-state) plasma operation. The conceptual design of DEMO begins with the quantitative definition of these main goals and shall proceed by selecting the major reactor parameters. The approach adopted in the EU-DEMO programme [2] follows different steps, iteratively repeated until a certain grade of satisfaction, consistency and attractiveness are met. Hence, the beginning of the actual engineering design hinges upon the verification of these conditions.

Dedicated computational tools, referred to as systems codes (SCs), are deployed to produce a DEMO baseline, relying on the definition of reactor requirements, constraints, and architectural features. The key function of SCs is to model the interactions between plant systems and the trade-offs that necessarily occur between them, allowing an integrated solution

* Author to whom any correspondence should be addressed.

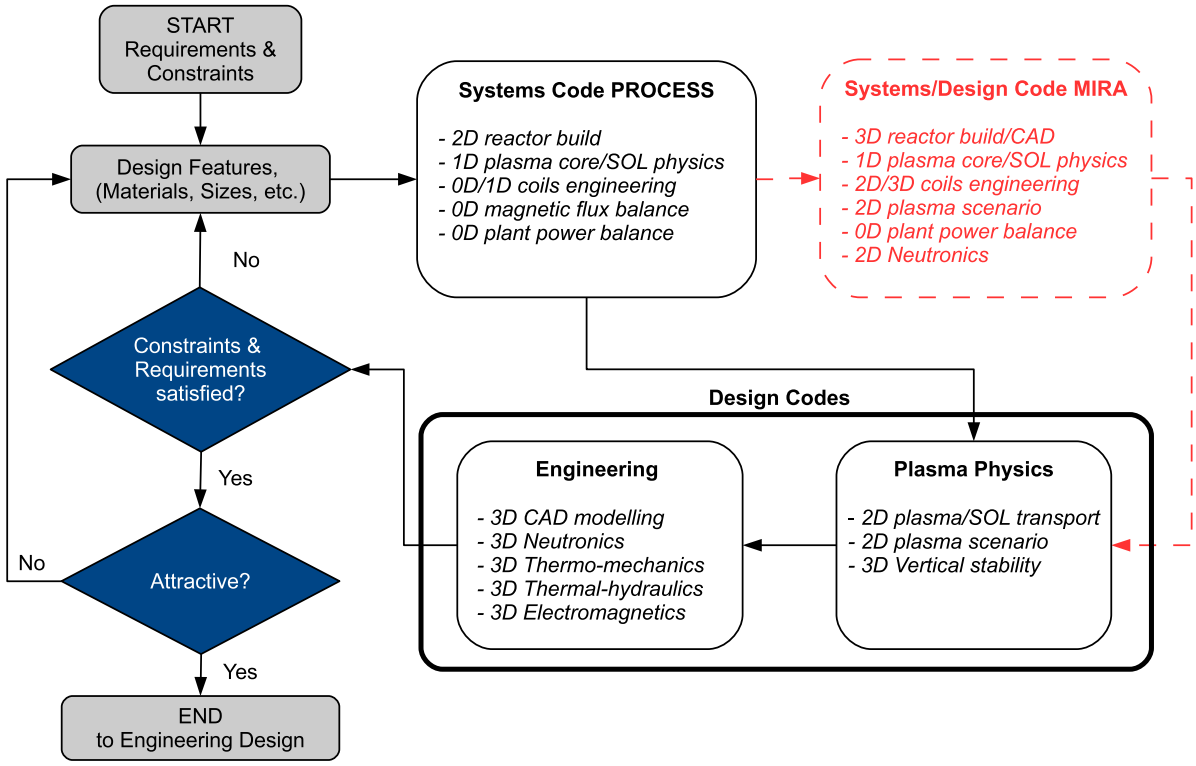

Figure 1. Conceptual design process in the EU-DEMO programme: without and with MIRA reactor analysis (black solid line path and red dashed line path, respectively).

to be found, and to do it fast enough that different reactor configurations can be explored. The SC output is then transferred to the detailed plasma transport and engineering design codes, normally in the form of a 2D reactor sketch and major reactor parameters (e.g. radial build, fusion power, major radius, and magnetic field).

Different fusion systems are presently available in the EU and worldwide to support the design of fusion reactors, each characterized by different features, architectures and scopes. The key presently-available fusion SCs are PROCESS [3, 4], SYCOMORE [5–7], ARIES systems code [8], KAERI system code [9] and JAERI system code [10]. These tools aim to explore one (or more) reactor configurations that simultaneously fulfil the plasma physics operational limits, the engineering constraints, and the plant requirements. In general, SCs rely on rather basic physics and engineering models (mostly at zero or one-dimensional level). While being very fast, SCs are currently deployed to optimise the DEMO reactor design based on specified figures of merit (e.g. minimizing the reactor sizes or the cost of electricity), and subject to engineering and physics requirements and constraints (R & C).

The physics and engineering design codes, instead, are very sophisticated and run on much longer computing times. The workflow of the current EU-DEMO conceptual design is depicted by the black solid line path in figure 1.

Due to the complexity of the design process, it is rather challenging to maintain data consistency and to keep an expedited design flow. In turn, wide modelling gaps between SCs (0D/1D, steady-state) and design codes (3D, time-dependent) might slow down and hinder the workflow, thereby increasing the number of iterations. To this end, the connections between the system and design codes can be consolidated by complementing the SCs with a more refined and intermediate system analysis tool, denoted as systems/design code (see figure 1, red-dashed line path), which can impose more consistency. The modular integrated reactor analysis code (MIRA) has been developed at KIT [11–13] and it is proposed as a new concept of advanced fusion reactors' systems/design analysis tool for the conceptual design process of DEMO. To this new category of fusion reactors' design codes belongs also BLUEPRINT [14–16], which features similar architectural and mathematical aspects and engages in the same set of goals. MIRA engages in a high modelling granularity, with reactor systems analyses up to three-dimensional sophistication. Such an approach allows scoping and parametrizing multiple reactor configurations with a more consolidated physics and engineering modelling representation at a component level, but still keeping a holistic view of the entire fusion plant. Thus, providing margins for design improvements to a higher degree.

The paper describes the systems/design code MIRA. The code architecture is presented in section 2, including a definition of the MIRA workflow. Section 3 outlines the key physics and engineering modelling features implemented in the code. Section 4 presents the results of the MIRA analysis carried out to assess the EU-DEMO 2017 baseline generated by the PROCESS code with a code-to-code comparison of the key physics and engineering parameters. The symbols

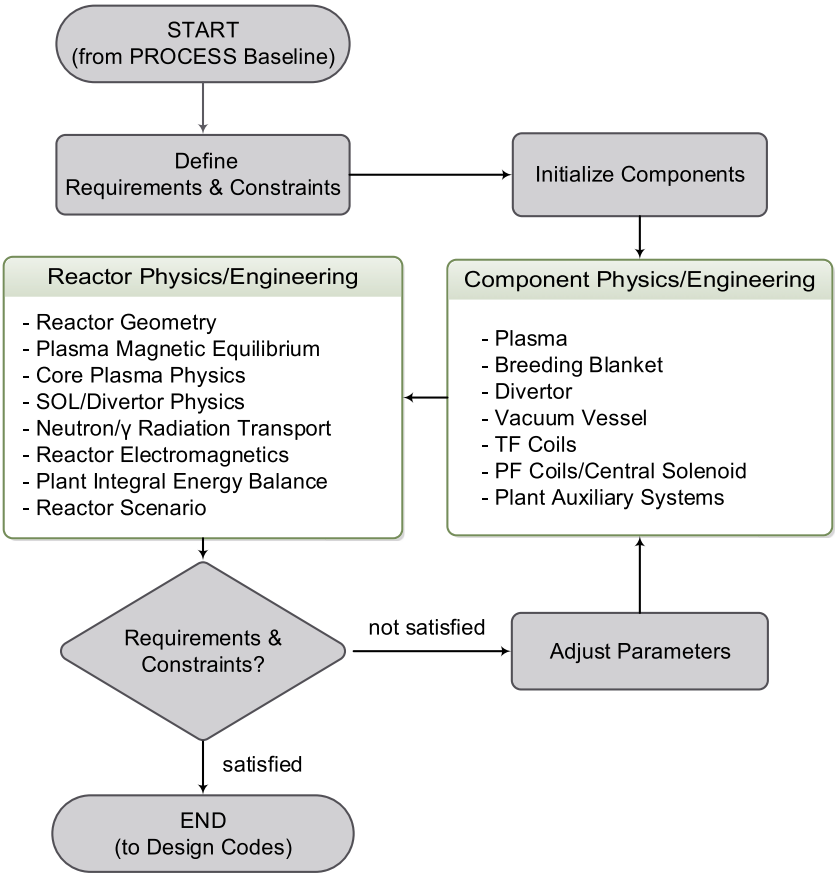

Figure 2. Organizational structure of the MIRA package.

and acronyms are given in dedicated sections at the end of the manuscript.

2. Architecture of the MIRA package

MIRA is a reactor design tool that relies on a modular structure. The workflow of a MIRA simulation is depicted in the flowchart of figure 2.

The calculation begins with a preprocessing phase, where physics and engineering R & C are first established and then the independent variables associated with each predefined reactor component are initialized. Requirements refer to specific values (or bounds) to meet the key design parameters (e.g. required net electric power), whereas constraints relate to the operational or technological limits of the defined components (e.g., minimum plasma safety factor to prevent magnetohydrodynamics (MHD) instabilities). Moving towards the data flow, the actual MIRA analysis takes place within two different modules 'containers', defined by *component and plant physics/engineering* modules. In *component* modules, all the physical components addressed by MIRA are initialized in terms of geometry, materials, R & C and any component-specific features (e.g. volume and mass calculation). *Plant* modules incorporate the analyses and methodologies established for systems or fields, where more than a single plant component is involved.

Upon each plant and component module execution, the R & Cs are scanned. If any of them is not met, the iteration variables associated with the definition of the component are properly adjusted. Currently, the parameters adjustment is performed manually through parametric scans, where the independent variables affecting the different R & Cs are identified and properly modified (e.g., with Newton–Raphson solving techniques). A MIRA run terminates successfully when all R & C are met.

3. Description of the MIRA modules

In this section, the main MIRA physics and engineering tools are outlined. A more detailed description of most of the models' implementation, verification and validation (V & V) is reported in [13].

3.1. MIRA geometric design

A MIRA analysis relies on the initialization of the radial and vertical space reservation of each physical component, i.e., plasma, breeding blanket (BB), vacuum vessel (VV), divertor, toroidal field (TF) and poloidal field (PF) coils, central solenoid (CS), as well as upper, equatorial and lower VV ports. For each of the outlined components, a set of geometric primitives is predefined to draw the 2D sketch from the plasma major radius R_0, aspect ratio A, upper and lower plasma

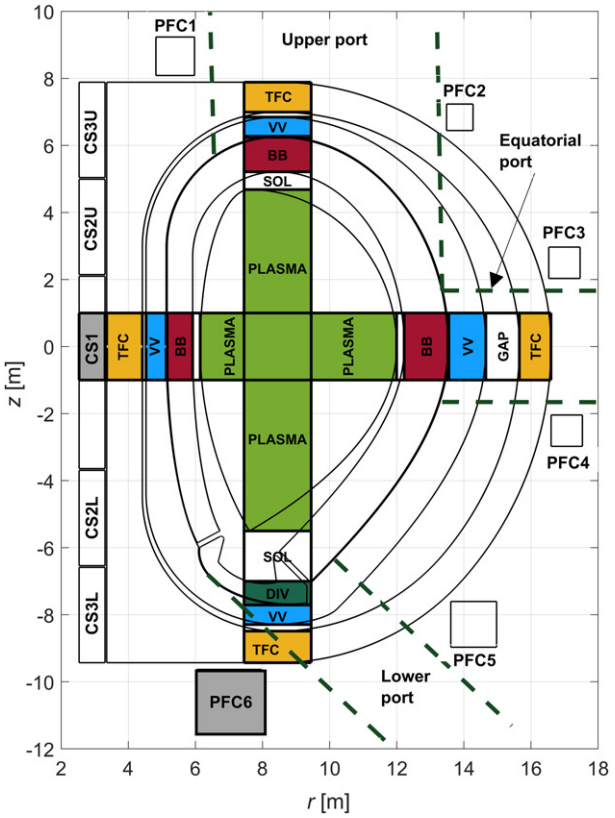

Figure 3. 2D sketch of the DEMO 2015 tokamak reactor, as per the MIRA geometry module. Reproduced with permission from [13].

edge elongation ($\kappa_{X,u}$, $\kappa_{X,l}$), plasma upper and lower triangularity ($\delta_{X,u}$, $\delta_{X,l}$) and the radial inboard/outboard and the vertical top/bottom thicknesses of all components. The reactor is built as visualized in figure 3. This sketch represents the 2D reactor build of the EU-DEMO 2015 baseline [17, 18], as per MIRA's geometric design module [13]. Additionally, each component is configured in terms of material composition and technological features.

The geometric module in MIRA acts on specific demands from the physics and engineering solvers to adapt the 2D shape of the reactor physical component according to specified physics and engineering constraints. For instance, the profile of the divertor geometry is adapted to the plasma separatrix determined by the free-boundary equilibrium (FBE) solver (section 3.2), to match the geometric design parameters (see figure 4), given by:

- inboard and outboard tilt angles, β_i and β_o,
- inboard and outboard distances ($d_{S,i}$ and $d_{S,o}$) from the strike points S_i and S_o to the plasma X-point X_1,
- targets vertical lengths, $l_{t,i}$ and $l_{t,o}$,
- baffle radius ρ_b,
- minimum cassette thickness d_c,
- inboard and outboard angles ($\alpha_{w,i}$ and $\alpha_{w,o}$) between the divertor segments facing the BB bottom terminations and the r-axis
- curvature radius of the cassette curve facing the private region, ρ_d.

The poloidal profile of the BB is constructed around the plasma separatrix and divertor shape. The FW profile is built specifying the inboard, outboard and top thickness of the scrape-off layer (SOL) region, which are defined on the mid-equatorial and vertical planes, as visualized in figure 3. The lower parts of the BB adjacent to the divertor profile are drawn from the tangency angles derived from $\alpha_{w,i}$ and $\alpha_{w,o}$ and imposing a gap orthogonally from the geometric points $D_{i,4}$ and $D_{o,4}$, defined on the divertor profile. The outer BB shape is obtained by offsetting outward the inner curve segments based on the inboard, outboard and top BB thickness. On top of the BB and divertor shapes, the VV ports for remote maintenance operation (upper, lower and equatorial) are also placed and sized poloidally. The upper and lower ports are inherited from the BB segment and divertor poloidal overall widths, respectively. The equatorial port is vertically centred on the mid-equatorial plane and its poloidal extension is specified as an input parameter. The radial and vertical extensions of the VV ports are used in the geometry module simply to identify space regions where the PF coils are not allowed to be placed.

The VV inner shape is a simple envelope of the outer BB and divertor bottom profiles, accounting for the void gaps between BB and VV and divertor and BB (user-defined). The outer VV shape and the inner TFC shape follow the same geometric rules (relying on the associated inboard/outboard/top/bottom widths), as well as the outer TFC shape, which includes a straight line to represent the inboard TFC leg.

Finally, for each PF coil i, the size and position are given as inputs, i.e. indicating the radial and vertical coordinates of the mass centre, $r_{m,i}$ and $z_{m,i}$, and their radial and vertical widths, Δr_i and Δz_i. Also, a feature in the geometry module allows moving the coils radially and/or poloidally, based on a specified minimum offset from the outer TF coil shape and the presence of the VV ports.

3.2. Plasma free-boundary equilibrium

MIRA incorporates a 2D FBE problem, for as a static magnetic equilibrium configuration between pressure gradients and Lorentz forces is sought in terms of toroidal current densities in plasma and coils regions. In axisymmetric radial, vertical and toroidal coordinates (r, z, ϕ) and in SI units such a problem is outlined by the Grad–Shafranov equation (GSE) and reads as (reference [19], p 25):

$$\begin{cases} r^2\nabla\cdot\left(\dfrac{\nabla\Psi}{r^2}\right) = -2\pi r\mu_0 J_\phi(r,\Psi) \\ \Psi|_{\partial\mathcal{D}} = 0 \end{cases}, \qquad (1)$$

where Ψ is the poloidal magnetic flux, $\mu_0 = 4\pi\times10^{-7}\,\mathrm{H\,m^{-1}}$ is the vacuum magnetic permeability and J_ϕ indicates the toroidal current density field in the (r, z) space. $\partial\mathcal{D}$ is the boundary enclosing the domain $\mathcal{D}$, defined by the union of plasma $\mathcal{D}_p$, coils $\mathcal{D}_c$ and vacuum $\mathcal{D}_0$ regions.

The weak formulation of equation (1) is solved through the finite-element method (FEM) to allow for a solution of curved domains characterizing tokamak plasma. Accordingly,

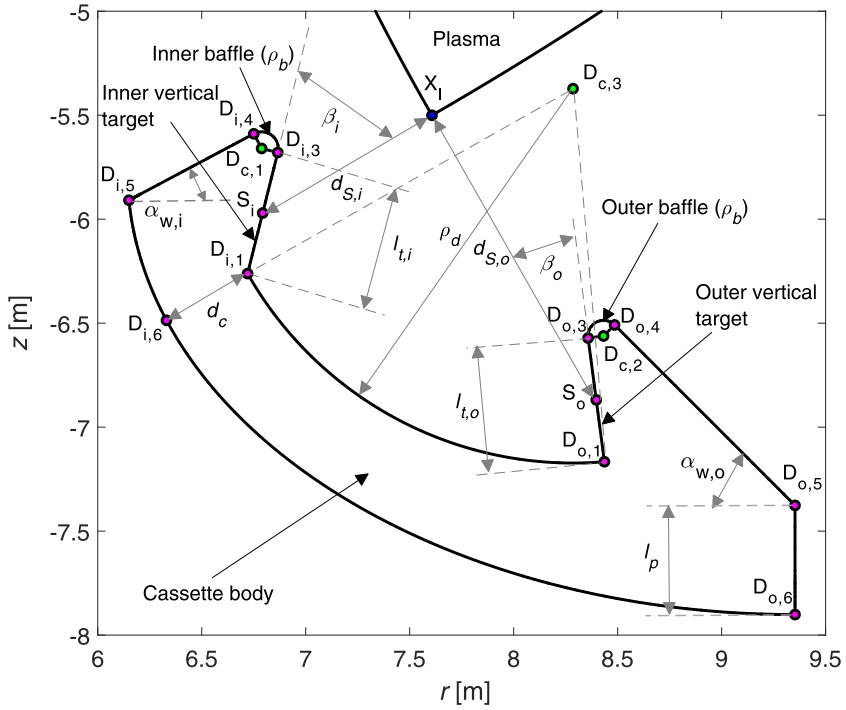

Figure 4. EU-DEMO 2015 divertor poloidal profile as per MIRA geometry module, with construction points and geometric input parameters in evidence. Reproduced with permission from [13].

it is defined as [20]

$$\begin{cases} \displaystyle\int_{\mathcal{D}_\mathrm{p}} \frac{1}{r} \nabla\Psi \cdot \nabla v \,\mathrm{d}r\,\mathrm{d}z = 2\pi\mu_0 \int_{\mathcal{D}} J_\phi\left(r,\Psi\right) v \,\mathrm{d}r\,\mathrm{d}z \\ \Psi|_{\partial\mathcal{D}} = \Psi_\mathrm{b} \end{cases}, \quad (2)$$

where v is the basis element function of the functional subspace $\mathcal{V} = \left\{ v \in H^1\left(\mathcal{D}\right) | v|_{\partial\mathcal{D}} = 0 \right\}$ of the Sobolev space $H^1\left(\mathcal{D}\right)$. Equation (2) is solved using the FreeFEM++ open-source partial differential equation solver [21], which is interfaced with MIRA. Since J_ϕ depends nonlinearly on Ψ in the plasma region $\mathcal{D}_\mathrm{p}$ (section 3.2.1), the solution is addressed via Picard iterations until a converging solution of Ψ is obtained.

The toroidal current density, J_ϕ is prescribed in each region of $\mathcal{D}$ as:

$$J_\phi = \begin{cases} 0, & \forall\ (r,z) \in \mathcal{D}_0 \\ J_{\phi,\mathrm{c}} & \forall\ (r,z) \in \mathcal{D}_\mathrm{c}, \\ J_{\phi,\mathrm{p}} = 2\pi r p' + \dfrac{\mu_0}{2\pi r} FF' & \forall\ (r,z) \in \mathcal{D}_\mathrm{p} \end{cases} \quad (3)$$

with $J_{\phi,\mathrm{c}}$ indicating the current density in each coil's conductor, $p' = \mathrm{d}p/\mathrm{d}\Psi$, with p indicating the plasma pressure and $F' = \mathrm{d}F/\mathrm{d}\Psi$, where $F(\Psi) = rB_\phi$ denotes the covariant component of the toroidal magnetic field B_ϕ. At the plasma boundary $F_\mathrm{b} = rB_\mathrm{t}$, where B_t is the magnetic field at the plasma centre, i.e., at $r = R_0$ and $z = 0$.

Henceforth, the goal of the FBE solver is to calculate $J_{\phi,\mathrm{c}}$ and $J_{\phi,\mathrm{p}}$ that fulfil equation (1) and produce a stable magnetic equilibrium for a plasma with a prescribed set of shape parameters. The resolution of the problem takes place in two iterating steps:

(a) Resolution of the fixed-boundary equilibrium/transport problem, where the plasma separatrix $\partial\mathcal{D}_\mathrm{p}$ is known and denotes the boundary of the resolution domain of the GSE, i.e., $\mathcal{D} \equiv \mathcal{D}_\mathrm{p}$. Here, p' and FF' are calculated from the plasma pressure p and safety factor q computed in the core physics module (section 3.3).

(b) Calculation of the PF coils and CS currents $\mathbf{I_c}$ required to fulfil the plasma shape requirements, the two-hour burn time limit (long-pulse plasma operation [1]), and the coils technological constraints [22].

3.2.1. 2D fixed-boundary equilibrium. The variables p' and FF' entering in $J_{\phi,\mathrm{p}}$ are prescribed in the form 1D profiles along a normalized flux coordinate $x \in [0,1]$, spanning from zeros on the plasma magnetic axis to one on the plasma boundary (see figure 5). In MIRA, x is derived from the poloidal flux Ψ to outline p' and FF' in equation (1). Accordingly, x reads as (reference [19], p 33):

$$x = \sqrt{\frac{\Psi_\mathrm{ax} - \Psi}{\Psi_\mathrm{ax} - \Psi_\mathrm{b}}}, \quad (4)$$

where, Ψ_ax and Ψ_b denote the poloidal flux at the plasma magnetic axis and plasma boundary, respectively.

The fixed-boundary equilibrium model calculates the profiles of p' and FF' to use in equation (1), based on the following parameters:

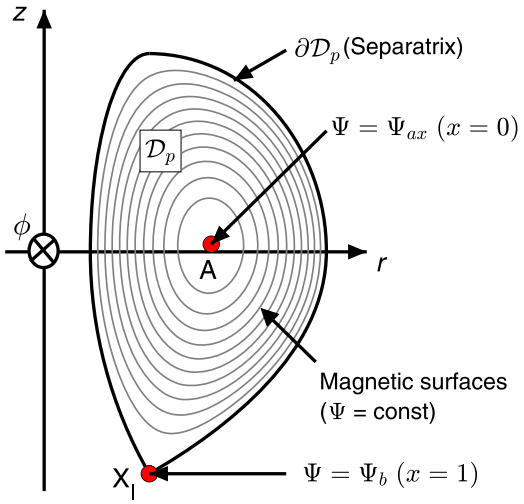

Figure 5. Schematic view of the plasma confining region and flux surface topology. Reproduced with permission from [13].

- plasma separatrix profile $\partial\mathcal{D}_\mathrm{p}(r,z)$,
- vacuum toroidal field at the plasma centre B_t,
- pressure profile $p(x)$,
- safety factor profile $q(x)$,

where x relates to the normalized flux coordinate reported in equation (4). The plasma boundary is calculated in the geometry module relying on a set of pre-built primitives which draw the poloidal contour as a function of $R_0, A, \kappa_{X,\mathrm{u}}, \kappa_{X,\mathrm{l}}, \delta_{X,\mathrm{u}}$ and $\delta_{X,\mathrm{l}}$. The geometric parametrization proposed by Johner [23] is adopted in MIRA to determine the poloidal profiles of elongated plasmas. Alternatively, it can be prescribed as a set of (r,z) pairs for a given number of separatrix points N_b. The latter setting is enabled when solving the whole equilibrium problem in the FBE mode (section 3.2), where the plasma shape is extracted from a global poloidal flux configuration. The plasma pressure and safety factor are obtained from the mass, energy and poloidal flux conservation laws, resolved in the MHD transport code PLASMOD [24], fully integrated into MIRA as a core physics block (section 3.3). B_t can be either set as input or calculated from the constraining condition imposed by the maximum magnetic field in the TF coil conductor $B_\mathrm{max,TFC}$ such that

$$B_\mathrm{t} \leqslant B_\mathrm{max,TFC}\frac{r_\mathrm{WP,ib}}{R_0}, \tag{5}$$

where, $r_\mathrm{WP,ib}$ is the innermost radial coordinate of the TF coil's winding pack (WP) on the inboard leg. The inequality constraint implies that pure equality would neglect the effects of the TF ripple (equation (37)) which are fully accounted for in the 3D magnetostatic module (section 3.6).

The mathematical approach adopted to compute p' and FF' is derived from [25] and slightly readapted to the MIRA structure for solving the fixed-boundary equilibrium problem. The method consists of solving the 2D GSE and its 1D flux-surface-averaged form iteratively. For fluid readability, the full derivation of p' and FF' from p and q (denoting the key coupling between plasma equilibrium and transport) is reported in appendix A.1, along with the aforementioned iteration scheme. Here, we report only their final expressions. Accordingly, FF' reads as:

$$FF' = -\frac{\mu_0}{g_3}p' + \frac{1}{4\pi^2 g_3}\frac{\partial}{\partial V}\left(g_2\frac{H}{q}\right), \tag{6}$$

where $V(\Psi)$ indicates the plasma volume profile, $H = \partial\Phi/\partial V$, $\Phi(\Psi)$ is the toroidal magnetic flux, $g_2(\Psi) = \left\langle |\nabla V|^2/r^2 \right\rangle$ and $g_3(\Psi) = \left\langle 1/r^2 \right\rangle$ are metric coefficients of the poloidal flux configuration $\Psi(r,z)$, and $\langle\cdot\rangle$ indicates the flux-surface averaging operator. p' is calculated as $p' = \partial p/\partial\Psi$, where $\Psi(x)$ is the radial poloidal flux profile calculated from the 1D GSE (equation (A.6)).

Some key plasma integral parameters are normally representative of confinement and stability plasma properties. These are computed in the fixed-boundary equilibrium model and are outlined as:

- Poloidal beta $\beta_\mathrm{p} = 2\mu_0\langle p\rangle / \left\langle B_\mathrm{p}^2\right\rangle_\mathrm{l}$, with p indicating the volume-averaged plasma pressure and $\left\langle B_\mathrm{p}^2\right\rangle_\mathrm{l} = \mu_0 I_\mathrm{p}/l_\mathrm{p}$ is the line-averaged poloidal field, l_p is the plasma perimeter.
- Toroidal beta $\beta_\mathrm{t} = 2\mu_0\langle p\rangle / B_\mathrm{t}^2$.
- Plasma internal inductance $l_\mathrm{i} = 2/\mu_0 I_\mathrm{p}^2 r_\mathrm{ax}\int_{\mathcal{D}_\mathrm{p}} B_\mathrm{p}^2\,\mathrm{d}V$ [26], where r_ax is the location of the axis defined by the axis magnetic null given by $\boldsymbol{B}_\mathbf{p} = (B_r, B_z) = (0,0)$, with B_r and B_z denoting the radial and vertical magnetic field components.
- Edge safety factor q_{95}, that is calculated at 95% poloidal flux surface, i.e., $q_{95} = q\left(x = \sqrt{0.95}\right)$. An operational limit is normally prescribed on $q_{95} \geqslant 3$. This limit is to prevent kink and sawtooth MHD instabilities [27].

The numerical solution of equation (2) could be easily verified against analytical solutions of the Biot–Savart equation (or Green's functions solution). Furthermore, the fixed-boundary equilibrium solver has been benchmarked against the Solov'ev equilibrium solution, for which analytical formulas can be found in the literature (e.g. [28]). A detailed description of the verification studies for the fixed-boundary equilibrium model is reported in [13].

3.2.2. A numerical solver for the PF coils and CS currents configuration. Based on the target plasma shape $\partial\mathcal{D}_\mathrm{p}^t$ [either calculated in the geometric module or set as input (r,z) vectors], and a given set of coils' sizes and positions, the toroidal current densities $J_{\phi,\mathrm{c}}$ shall meet the plasma shaping requirements and the coils technological limits. The shaping requirements are posed on a prescribed value of plasma elongation κ_{95}, triangularity δ_{95} and volume V_p, where κ_{95} and δ_{95} denote the elongation and triangularity calculated at 95% flux surface $(x = \sqrt{0.95})$, and $V_\mathrm{p} \equiv V(x = 1)$. For DEMO coils scenario analysis, the PF coils/CS technological limits are prescribed in terms of:

- maximum current density $J_\mathrm{c,max} = 12.5$ MA m^{-2} [22],
- magnetic field $B_\mathrm{max} \sim 6$ T for the PF coils [29] and $B_\mathrm{max} \sim 13$ T for the CS [30],

- max vertical forces on single PF coils $F^{\mathrm{PF}}_{z,\max} = 450$ MN [22],
- maximum vertical force and maximum separation force on the CS stack, i.e., $F^{\mathrm{CS}}_{z,\max} = 300$ and $F^{\mathrm{CS,sep}}_{z,\max} = 350$ MN [22], respectively.

The N_c toroidal currents $\mathbf{I_c} = \left[I_{\mathrm{c},1}, \ldots I_{\mathrm{c},N_\mathrm{c}}\right]$ carried by the N_c PF coils and the CS elements are to be calculated based on such R & C. The total current in the coil i relates to current density $J^i_{\phi,\mathrm{c}}$ in domain $\mathcal{D}_{\mathrm{c},i}$ of coil i, such that $I_{\mathrm{c},i} = J^i_{\phi,\mathrm{c}} \cdot \Delta r_i \cdot \Delta z_i$, with Δr_i and Δz_i being the radial and vertical width of the current-carrying cross-section. If $\partial\mathcal{D}^{\mathrm{t}}_{\mathrm{p}}$ is discretized into N_b points, $\mathbf{I_c}$ must be such that the poloidal flux $\Psi_k = \Psi(r_k, z_k)$ on each kth point (r_k, z_k) is required to be constant and equal to a prescribed value $\Psi^{\mathrm{t}}_{\mathrm{b}}$. If $N_\mathrm{b} > N_\mathrm{c}$ (and that is normally the case to closely replicate $\partial\mathcal{D}^{\mathrm{t}}_{\mathrm{p}}$), the problem becomes over-constrained (or ill-posed) and finding the solution $\mathbf{I_c}$ becomes an optimization problem, where a linear least-square solution method has been implemented. Accordingly, the shaping problem becomes a constrained optimization one, defined as:

$$\min_{\mathbf{I_c}} \mathcal{L}(\partial\mathcal{D}^{\mathrm{t}}_{\mathrm{p}}, \mathbf{I_c}, J_{\phi,\mathrm{p}}) \text{ s.t. } \begin{cases} \Psi_X(\mathbf{I_c}, J_{\phi,\mathrm{p}}) = \Psi^{\mathrm{t}}_{\mathrm{b}} & \\ B_{j,X}(\mathbf{I_c}, J_{\phi,\mathrm{p}}) = 0 & \\ |I_{\mathrm{c},i}| \leqslant I_{\mathrm{c,max}} & j = r, z \\ |B_{\mathrm{peak},i}(\mathbf{I_c}, J_{\phi,\mathrm{p}})| \leqslant B_{\mathrm{max},i} & i = 1, .., N_\mathrm{c} \\ \left|F^{\mathrm{PF}}_{z,g}(\mathbf{I_c}, J_{\phi,\mathrm{p}})\right| \leqslant F^{\mathrm{PF}}_{z,\max} & i = 1, .., N_\mathrm{c} \\ \left|\sum_{g}^{N_{CS}} F^{\mathrm{CS}}_{z,g}(\mathbf{I_c}, J_{\phi,\mathrm{p}})\right| \leqslant F^{\mathrm{CS}}_{z,\max} & g = 1, \ldots, N_{\mathrm{PF}} \\ \sum_{i=1}^{g} F^{\mathrm{CS}}_{z,i}(\mathbf{I_c}, J_{\phi,\mathrm{p}}) \leqslant F^{\mathrm{CS,sep}}_{z,\max} & \\ \sum_{i=1}^{g} F^{\mathrm{CS}}_{z,N_{\mathrm{CS}}-i+1}(\mathbf{I_c}, J_{\phi,\mathrm{p}}) \geqslant -F^{\mathrm{CS,sep}}_{z,\max} & g = 1, \ldots, N_{\mathrm{CS}} \end{cases} \tag{7}$$

with $\mathcal{L}$ defining the Euclidean norm of the residual error function (being the objective function of the constrained optimization problem) calculated on the N_b target separatrix point and given by:

$$\mathcal{L}(\boldsymbol{I_c}) = \frac{1}{2N_\mathrm{b}} \left(\sum_{k}^{N_\mathrm{b}} \left| \Psi_\mathrm{k}\left(\mathbf{I_c}, J_{\phi,\mathrm{p}}\right) - \Psi^{\mathrm{t}}_{\mathrm{b}} \right|^2 \right) + \left\| \hat{\mathbf{\Gamma}} \cdot \boldsymbol{I_c}^2 \right\|. \tag{8}$$

The term $\left\| \hat{\mathbf{\Gamma}} \cdot \mathbf{I_c}^2 \right\|$ relates to the Tikhonov regularization term [31], which can be enabled for any suitably defined Tikhonov matrix $\hat{\mathbf{\Gamma}}$. As in other equilibrium solvers [16], $\hat{\mathbf{\Gamma}}$ is defined as a multiple of the identity matrix $\hat{\mathbf{\Gamma}} = \gamma\mathbf{I}$, with γ being a small user-defined constant ($\sim 10^{-7}$) used to give preference to solutions of $\mathbf{I_c}$ with smaller norms.

Ψ_X, $B_{r,X}$ and $B_{z,X}$ indicate the flux Ψ and the radial and vertical field components B_r and B_z calculated at the fixed target X-points (one lower X-point for single-null divertor configurations). $B_{\mathrm{peak},i}$ is the peak magnetic field calculated at the edge of each PF and CS coil, $F^{\mathrm{PF}}_{z,g}$ and $F^{\mathrm{CS}}_{z,g}$ the vertical force acting on the gth PF or CS coil, and N_{PF} and N_{CS} the total number of PF and CS coils. All the coils' limits are calculated in MIRA according to the formalism reported in [22]. Note that because of the linearity of the magnetostatic problem outlined in equation (1), the poloidal flux and fields at any given poloidal location can be expressed as a linear combination of the flux and field contributions from each coil current $I_{\mathrm{c},i}$ and from the plasma current I_p, such that

$$\Psi_k \equiv \Psi(r_k, z_k) = \sum_{i=1}^{N_\mathrm{c}} \mathcal{G}_{\Psi,k,i} \cdot I_{\mathrm{c},i} + \mathcal{G}_{\Psi,k,p} \cdot I_\mathrm{p} \tag{9}$$

and

$$\begin{aligned} B_{j,k} &\equiv B_j(r_k, z_k) \\ &= \sum_{i=1}^{N_\mathrm{c}} \mathcal{G}_{B_j,k,i} \cdot I_{\mathrm{c},i} + \mathcal{G}_{B_j,k,p} \cdot I_\mathrm{p}, \quad \text{with } j = r, z. \end{aligned} \tag{10}$$

The coefficients $\mathcal{G}_{\Psi,k,i}$ and $\mathcal{G}_{\Psi,k,p}$ are the Green's functions of the elliptic operator of the GSE. These are calculated at the poloidal location $k = (r_k, z_k)$ and they are associated with the coil i and plasma currents, respectively. $\mathcal{G}_{B_j,k,i}$ and $\mathcal{G}_{B_j,k,p}$ are similarly defined to evaluate the radial and the vertical fields B_r and B_z. Equations (9) and (10) are used to apply in equation (7) the equality constraints on the Ψ_X and $B_{j,X}$ and to calculate in equation (8) the poloidal flux on the N_b target boundary points for shaping purposes Furthermore, recalling the definition of the volumetric Lorentz force's vertical component $f_z(r, z) = -J_\phi(r, z) \cdot B_r(r, z)$, the same concept can be applied to calculate the vertical force $F_{z,i}$ acting on the coil i as a nonlinear combination of the coils' currents. Accordingly,

$F_{z,i}$ can be expressed as

$$F_{z,i} = I_{c,i} \cdot \left(\sum_{j \neq i}^{N_c} \mathcal{G}_{F_z,j \to i} I_{c,j} + \mathcal{G}_{F_z,p \to i} I_p \right), \qquad (11)$$

where $\mathcal{G}_{F_z,j\to i}$ and $\mathcal{G}_{F_z,p\to i}$ are the coefficients relating the mutual vertical forces between the coil pairs (i, j) and (i, p), and 'p' refers to the plasma. Thus, based upon a pre-built set of mutual force coefficients, equation (11) is used for applying the nonlinear vertical force constraints of equation (7). The full derivation of all Green's functions for the calculation of the poloidal flux, field and vertical force is reported in appendix A.2.

The constrained optimization problem related to the coils' current resolution is solved in MIRA using the interior point algorithm [32]. The fixed-boundary equilibrium and coils currents calculation are iteratively executed over the plasma shape and the plasma current density, until all coil currents, δ_{95}, κ_{95} and V_p converge to a constant value. Within the mth iteration step, the plasma separatrix is known from the previous iteration $\partial\mathcal{D}_p^{(m-1)}$, as well as the target separatrix $\left(\partial\mathcal{D}_p^t\right)^{(m-1)}$. The plasma separatrix needed in the first step ($m = 1$) is set to the initial target separatrix $\left(\partial\mathcal{D}_p^t\right)^{(0)}$, which is calculated from the reference values of R_0 and A and from an initial guess of upper and lower edge elongations ($\kappa_{X,u}^{(0)}$, $\kappa_{X,l}^{(0)}$) and triangularity ($\delta_{X,u}^{(0)}$, $\delta_{X,l}^{(0)}$). Edge elongations and triangularities are used to control κ_{95} and δ_{95}, by adjusting the target separatrix shape to use in equation (7), whereas R_0 is used to match the shaping requirement posed on V_p. In summary, the following steps outline the overall iteration scheme implemented in MIRA for the FBE solver:

(a) Calculate the Green's functions $\mathcal{G}_{\Psi,k,p}^{(m)}$, $\mathcal{G}_{B_r,k,p}^{(m)}$, $\mathcal{G}_{B_z,k,p}^{(m)}$, the mutual force coefficients and $G_{F_z,p\to i}^{(m)}$ from $J_{\phi,p}$ calculated in the previous iteration $\left(\boldsymbol{J}_{\phi,p}^{(m-1)}\right)$.

(b) Compute the PF/CS coils current configuration $\boldsymbol{I}_c^{(m)}$ (equation (7)).

(c) Solve equation (2) to get $\Psi^{(m)}$ with J_ϕ calculated from the new PF coils currents $\boldsymbol{I}_c^{(m)}$ and plasma current density from the previous iteration $J_{\phi,p}^{(m-1)}$.

(d) If the κ_{95}, δ_{95} and V_p plasma shape requirements are enabled, calculate $\kappa_{95}^{(m)}$, $\delta_{95}^{(m)}$ and $V_p^{(m)}$ from $\Psi^{(m)}$ and adjust $\kappa_{X,u}$, $\kappa_{X,l}$, $\delta_{X,u}$, $\delta_{X,l}$ and R_0 to match the prescribed values of κ_{95}^t, δ_{95}^t and V_p^t and recalculate new profile of target separatrix $\left(\partial\mathcal{D}_p^t\right)^{(m)}$. Between each iteration, the adjustment of such parameters is performed with a simple proportional control scheme and employing under-relaxation.

(e) Find the new plasma separatrix profile $\partial\mathcal{D}_p^{(m)} = \{r, z\} \,|\, \Psi^{(m)} = \Psi_b^t$.

(f) Solve 2D fixed-boundary equilibrium + 1D transport as per the iteration scheme outlined in section 3.3.5 and get the new plasma boundary $\partial\mathcal{D}_p^{(m)}$ to update $\partial\mathcal{D}_p^{(m-1)} \leftarrow \partial\mathcal{D}_p^{(m)}$ and new plasma profiles $p^{(m)}$ and $q^{(m)}$.

(g) From $p^{(m)}$ and $q^{(m)}$ get the new plasma current density profile $J_{\phi,p}^{(m)}$ to update $J_{\phi,p}^{(m-1)} \leftarrow J_{\phi,p}^{(m)}$.

(h) Repeat all steps from (a) to (g) until the iteration error, calculated on each value of $\boldsymbol{I}_c$, and on κ_{95}, $\delta_{95}$and V_p, is below a certain upper limit, normally fixed to $\sim 10^{-4}$–10^{-5}.

Currently, the FBE solver does not optimize the PF coils' size, position and number to maximize the plasma shaping capabilities or any other figures of merit. Nevertheless, the PF coils and CS elements are adapted to the TF coils outer profile and VV ports. Hence, the reactor configurations coming from a full MIRA analysis are normally rather close to those found in detailed DEMO scenario analyses [22], in terms of sizes and positions.

The FBE implemented in MIRA calculates the PF coils' currents based on two-dimensional plasma shaping criteria applied to realistic elongated plasmas, and with the plasma current density obtained from p' and FF' profiles fully consistent with MHD plasma transport. In several equilibrium solvers (e.g. [33]), instead, the equilibrium solution is obtained prescribing some pre-defined polynomial expressions of $J_{\phi,p}$ whose coefficients are computed constraining certain key plasma integral parameters, such as I_p, β_p, l_i and q_{95} to a target value. Also, the PF coils' current, field, and vertical forces technological constraints are fully constrained. Overall, this modelling sophistication helps significantly to characterize a reactor pulse and provides two-dimensional insights that enhance the design of the reactor physical components considerably.

3.3. Core and SOL physics

SCs often attempt to tackle the key core physics processes with a simplified 0D approach, where prescribed profiles parametrizations are set to reproduce some expected electron and ions density and temperatures, and scaling laws are used to have crude predictions on the energy confinement (e.g., ITER Physics Basis IPB98 scaling law [34]). Formerly, such an approach has been part of the MIRA core physics modelling, too [13]. Recently, this approach has been fully replaced by a plasma transport solver. The core physics module currently implemented in MIRA incorporates the 1D MHD transport and equilibrium code PLASMOD [24, 35], inherited from the transport code ASTRA [36].

A one-dimensional approach is vital to assess reactor designs, as the profiles effects play a key role in the evaluation of the integral plasma parameters, such as fusion and radiation power. Also, the core and pedestal physics are very different and cannot be properly captured by global scaling laws. Finally, reliable predictions of the bootstrap current are needed to fully characterize the demands of inductive fractions and depict the capabilities to operate plasma with long pulses. These can be computed properly only by calculating the plasma profiles from MHD transport solutions.

In PLASMOD, four major blocks are incorporated and appropriately coupled to produce a consistent plasma configuration. These are:

- A 1D transport solver for the radial profiles of the ion temperature $T_i(\rho)$, electron temperature $T_e(\rho)$, and electron density $n_e(\rho)$ along the normalized flux coordinate

$\rho = \sqrt{\Phi/\Phi_b}$, with $\Phi(\rho)$ denoting the toroidal flux profile and Φ_b the toroidal flux at plasma boundary.

- A 1D current diffusion equation (CDE) solver, for the conservation law of the poloidal flux Ψ.
- A 2D equilibrium solver for the resolution of the GSE in Ψ and the calculation of the metric coefficients g_2 and g_3 and volume V to use in the transport and CDEs.
- A 0D model to compute the power load to the divertor due to advective/conductive transport losses across the separatrix.

In this section, the four models are outlined, along with an integration scheme proposed for integrating PLASMOD into the MIRA framework.

3.3.1. 1D transport solver. In the 1D transport solver, the flux-surface-averaged steady-state conservation laws for electron density n_e, electrons temperature T_e and ions temperature T_i are solved in the following one-dimensional form [25]:

$$\frac{1}{V'}\frac{\partial\left(V'\Gamma_Y\right)}{\partial\rho} = S_Y(\rho, Y), \tag{12}$$

where, $V' = \partial V/\partial\rho$, $Y(\rho)$can be n_e, T_e or T_i, Γ_Y is the transport flux of Y and S_Y denotes the sum of sinks and sources of Y. Γ_Y is the transport flux and is calculated as the sum of advection and conduction contributions [35], such that $\Gamma_Y = -\chi_Y\partial Y/\partial\rho + v_Y Y$, where χ_Y is the diffusivity and v_Y is the convective velocity.

The core transport processes, such as turbulence, collisions, ideal and resistive MHD modes, determine the steady-state temperature and density profiles from the magnetic axis ($\rho = 0$) to the pedestal top position $\left(\rho = \rho_{ped}\right)$. The transport coefficients are calculated employing a simple gyro-Bohm scaling (e.g., $\chi_Y \sim T_e^{3/2}/B^2$ [37, 38]), and they are re-scaled to match the temperature and the density profiles obtained in previous theoretical studies [24, 39, 40]. The pedestal top at $\rho = \rho_{ped}$ acts as a boundary for equation (12). The electron density at the pedestal top $n_{e,ped}$, can be either set as a fraction $f_{GW,ped}$ of the Greenwald density with $n_{GW} = I_p/\pi a^2$ [41] set as an input. In the former case, $f_{GW,ped} = n_{e,ped}/n_{GW}$, where $f_{GW,ped} \leqslant 1$ represents a key plasma operational limit to prevent thermal instabilities [42]. The electrons and ions temperatures at pedestal height $T_{e,ped}$ and $T_{i,ped}$ are assumed equal and can be either set as inputs or calculated using the scaling law reported in [43], derived from a large set of runs performed with the MHD pedestal code EPED [44]. The plasma density at the plasma separatrix ($\rho = 1$) is also prescribed in terms of Greenwald fraction $f_{GW,sep}$, and the temperature T_{sep} is again fixed as input parameter and assumed equal for both ions and electrons. Furthermore, an upper limit is normally posed in the normalized beta limit $\beta_N = \beta_t/\left(I_p/aB_t\right)$, such that $\beta_N < 4l_i$ to avoid pressure-driven MHD instability modes [45, 46].

Fueling and auxiliary heating sources are modelled in PLASMOD specifying their radial profiles and the integral deposition (power or injection rate). In particular, a Gaussian distribution along ρ outlines the radial behaviour, where the mean deposition location $\overline{\rho}$ and the standard deviation σ_ρ are user-defined parameters. In addition, PLASMOD allows specifying NBI power deposition, which is deployed for fueling, auxiliary heating and current drive purposes. Pellet injection and electron cyclotron heating can be also readily enabled.

The steady-state power density source terms $\dot{q}_e$ and $\dot{q}_i$ for electrons and ions are computed as

$$\begin{aligned}\dot{q}_e &= \dot{q}_{\alpha,e} + \dot{q}_{add,e} + \dot{q}_{oh} - \dot{q}_{rad} - \dot{q}_{e,i}\\ \dot{q}_i &= \dot{q}_{\alpha,i} + \dot{q}_{add,i} + \dot{q}_{e,i}\end{aligned}, \tag{13}$$

where, $\dot{q}_{\alpha,e}$ and $\dot{q}_{\alpha,i}$ are the shares of fusion alpha power density absorbed by electrons and ions, $\dot{q}_{add,e}$ and $\dot{q}_{add,i}$ are the additional heating powers deposited to electrons and ions, $\dot{q}_{oh}$ is the ohmic heating power density, $\dot{q}_{rad}$ is the radiation power density and $\dot{q}_{e,i}$ is the classical equipartition power from electrons to ions. The alpha fusion power $\dot{q}_\alpha = \dot{q}_{fus}/5$ is calculated from the total fusion power $\dot{q}_{fus}$ defined as:

$$\dot{q}_{fus} = E_{fus,DT} n_D n_T \langle\sigma v(T_i)\rangle_{DT}, \tag{14}$$

where n_D and n_T are the deuterium and tritium density profiles, $E_{fus,DT}$ being the fusion reaction energy, and $\langle\sigma v\rangle_{DT}$ is the velocity-averaged DT fusion cross-section (e.g., scaling laws from [47, 48]). For the sake of simplicity, it is assumed that a fuel composition includes only deuterium and tritium and that the fusion energy is uniquely produced via DT fusion reactions. Nevertheless, PLASMOD accounts for DD contributions, too. The repartition between ions and electrons of $\dot{q}_\alpha$ is computed in PLASMOD taking into account the alphas slowing downtime and the collisionality, similarly to ASTRA [36].

The auxiliary heating power density $\dot{q}_{add}$ is modelled through the total additional heating power P_{add} and the profile's mean value and standard deviation. The ion/electron repartition of the total auxiliary heating power density $\dot{q}_{aux}$ is assumed to be distributed in a 60/40 ratio [49]. The ohmic heating power $\dot{q}_{oh}$ is found as $q_{oh} = I_p \cdot f_{ind} \cdot U_{loop}/V_p$, with f_{ind} being the inductive fraction of the plasma current, and U_{loop} the loop voltage (equation (22)).

The equipartition power $\dot{q}_{e,i} \propto n_e(T_e - T_i)/\tau_{eq}$ relates to the net energy exchange between electrons and ions due to Coulomb collisions, where $\tau_{ei} \sim 1/\nu_{ei}$ is associated with the electron/ion's collision frequency $\nu_{eq} \propto n_i/T_e^{3/2}$ (reference [50], p 132).

The radiation loss term $\dot{q}_{rad}$ is defined as

$$\dot{q}_{rad}(\rho) = \dot{q}_{brem}(\rho) + \dot{q}_{line}(\rho) + \dot{q}_{sync}(\rho), \tag{15}$$

and incorporates the power losses associated with the following contributions:

- Bremsstrahlung radiation $\dot{q}_{brem} \propto Z_{eff} n_e^2 \sqrt{T_e}$ due to Coulomb collisions, with $Z_{eff} = \left\langle \sum_j n_j Z_j^2/n_e \right\rangle$ being the plasma effective charge.
- Line radiation $\dot{q}_{line} = n_e \sum_j n_j \cdot L_{Z,j}(T_e)$ due to all j plasma impurities, with $L_{Z,j}$ being the radiative power loss function (or luminosity). In PLASMOD, the radiation loss

functions are inherited from [51], but they are also available from the ADAS database [52].

- Synchrotron radiation $\dot{q}_{\mathrm{sync}}$ (see [49] for the complete formulation) due to particle motion in the magnetic field, and ruled by $n_{\mathrm{e}}, T_{\mathrm{e}}, B_{\mathrm{t}}$ and plasma geometry figures (κ_{95}, A, R_0).

In the plasma edge, delimited by $\rho_{\mathrm{edge}} \leqslant \rho \leqslant 1$ (with ρ_{edge} being a prescribed edge location), the radiation losses are predominantly characterized by line radiation, whereas in the core region ($0 \leqslant \rho < \rho_{\mathrm{edge}}$) bremsstrahlung and synchrotron radiations represent the main contributions.

Finally, taking the total power P_x as the volume integral of the power density term $\dot{q}_x$ (with $x = \alpha$, add, rad, oh) outlined in equation (13), and summing the ions and electrons powers, the following integral power balance in the core plasma region is obtained:

$$P_\alpha + P_{\mathrm{add}} + P_{\mathrm{oh}} = P_{\mathrm{sep}} + P_{\mathrm{rad}}, \tag{16}$$

where

$$P_{\mathrm{sep}} = \int_{\mathcal{D}_{\mathrm{p}}} (\dot{q}_{\mathrm{e}} + \dot{q}_{\mathrm{i}})\, \mathrm{d}V \tag{17}$$

identifies the net power crossing the separatrix through advective and conductive transport losses. Combining the plasma thermal energy $W_{\mathrm{th}} \propto \int (n_{\mathrm{e}} T_{\mathrm{e}} + n_{\mathrm{i}} T_{\mathrm{i}})\, \mathrm{d}V$ and the definition of the global energy confinement time $\tau_{\mathrm{E}} = W_{\mathrm{th}}/P_{\mathrm{sep}}$, the H factor is calculated as $H = \tau_{\mathrm{E}}/\tau_{\mathrm{E}}^{\mathrm{IPB98(y,2)}}$, with $\tau_{\mathrm{E}}^{\mathrm{IPB98(y,2)}}$ being the IPB98(y, 2) scaling law with the radiation-corrected power term to account for a high radiation power [49]. Taking $f_{\mathrm{P2E}} = \tau_{\mathrm{p}}/\tau_{\mathrm{E}}$, as a given particle-to-energy-confinement ratio $\sim$5 [24], with τ_{p} being the particle confinement time, the overall helium inventory in the confining region $N_{\mathrm{He}} = \frac{P_\alpha}{E_\alpha}\tau_{\mathrm{p}}$ is obtained from the steady-state integral helium mass balance, where E_α is the kinetic energy associated with the alpha particles. Defining the helium fraction $c_{\mathrm{He}} = N_{\mathrm{He}}/\int n_{\mathrm{e}}\, \mathrm{d}V$, the helium density profile n_{He} is approximated as a fraction of n_{e}, such that, $n_{\mathrm{He}}(\rho) = c_{\mathrm{He}} n_{\mathrm{e}}(\rho)$. Finally, bearing in mind the plasma quasi neutrality, the fuel density profile n_{fuel} reads as

$$n_{\mathrm{fuel}} = n_{\mathrm{e}} - 2 \cdot n_{\mathrm{He}} - \sum_j Z_j n_j, \tag{18}$$

where n_j is the density profile of the impurity j with a charge number Z_j. n_j is modelled in PLASMOD through the definition of fractions c_j such that $n_j = c_j \cdot n_{\mathrm{e}}$, with c_j being either calculated or fixed, depending on the purposes. Hydrogen, argon, xenon and tungsten, along with deuterium, tritium, ^{4}He and ^{3}He represent the entirety of atomic species currently included in the PLASMOD's atomic database, consisting of charge number and radiative loss functions L_Z. Based upon the definition of a fuel mix factor f_{D}, denoting the fraction of deuterium in the fuel composition (normally it is assumed a 50/50% D/T fuel mix), the deuterium and tritium density profiles to use in equation (14), are readily calculated as $n_{\mathrm{D}} = f_{\mathrm{D}} \cdot n_{\mathrm{fuel}}$ and $n_{\mathrm{T}} = (1 - f_{\mathrm{D}})\, n_{\mathrm{fuel}}$.

Finally, the plasma pressure profile $p(\rho)$, used in equations (3) and (6) to solve the fixed-boundary equilibrium problem, reads as:

$$p = n_{\mathrm{e}} T_{\mathrm{e}} + n_{\mathrm{i}} T_{\mathrm{i}} + p_\alpha, \tag{19}$$

where, $n_{\mathrm{i}} = n_{\mathrm{fuel}} + n_{\mathrm{He}} + \sum_j n_j$ is the total ion density and p_α is the pressure of fast alpha particles.

The strong nonlinearities affecting especially the radiation losses and the transport coefficients make the system of partial differential equation (12) rather challenging in terms of its numerical resolution, thus requiring a robust iteration scheme. More details on these aspects are reported in [35].

3.3.2. 1D solver for the current diffusion equation. The 1D CDE is the conservation law of the poloidal flux $\Psi(\rho)$, derived from the longitudinal Ohm's law [36], reading as:

$$j_\parallel = \sigma_\parallel E_\parallel + j_{\mathrm{BS}} + j_{\mathrm{CD}}, \tag{20}$$

where $E_\parallel \equiv \langle \mathbf{E} \cdot \mathbf{B} \rangle / B_{\mathrm{t}}$ is the parallel electric field, $j_\parallel \equiv \langle \mathbf{J} \cdot \mathbf{B} \rangle / B_{\mathrm{t}}$ the parallel current density, $\sigma_\parallel$ the neoclassical plasma electric conductivity [53, 54], j_{BS} the parallel bootstrap current density, and j_{CD} the longitudinal CD current density. $j_\parallel$, and similarly, j_{BS} and j_{CD}, is combined with the flux surface definition of the toroidal current $I_{\mathrm{tor}}(\rho)$ [36], such that

$$I_{\mathrm{tor}}(\rho) = \int_{S_{\mathrm{tor}}} \mathbf{J} \cdot \mathrm{d}\mathbf{S} = \frac{B_{\mathrm{t}}}{2\pi} F(\rho) \int_0^{V(\rho)} \frac{j_\parallel(\rho)}{F^2(\rho)} \mathrm{d}V, \tag{21}$$

which, for $\rho = 1$, yields the total plasma current I_{p}. Analogously, replacing $j_\parallel$ in equation (21) with j_{CD} and j_{BS} would return the total CD current I_{CD} and bootstrap current I_{BS}, respectively Assuming that the vacuum toroidal field B_{t} is time-independent, the plasma loop voltage U_{loop}, used to describe the irreversible diffusive flux of Ψ through the flux surfaces ρ, is given by [36]:

$$U_{\mathrm{loop}} = -\left.\frac{\partial \Psi}{\partial t}\right|_{\rho_{\mathrm{b}}} = 2\pi B_{\mathrm{t}} \frac{E_\parallel}{F_{\mathrm{b}} g_{3,\mathrm{b}}}, \tag{22}$$

where $E_\parallel$ (usually constant over ρ [36]) can be evaluated recasting equation (20) and using the integral definitions of I_{p}, I_{CD} and I_{BS} from equation (21), such that

$$E_\parallel = \frac{I_{\mathrm{p}} - I_{\mathrm{BS}} - I_{\mathrm{CD}}}{\frac{F_{\mathrm{b}} B_{\mathrm{t}}}{2\pi} \int_0^{V_{\mathrm{p}}} \frac{\sigma_\parallel}{F^2} \mathrm{d}V}. \tag{23}$$

The neoclassical plasma conductivity $\sigma_\parallel$ and the bootstrap current density $j_{\mathrm{BS}} \propto \sqrt{r/R_0} \nabla p / B_{\mathrm{p}}$ (reference [19], p 189) are calculated from the transport profiles using Sauter's formulas [53, 54], whereas the total CD current I_{CD} scales with the injected CD power density $\dot{q}_{\mathrm{CD}}$ such that $j_{\mathrm{CD}} = \gamma_{\mathrm{CD}} / \langle n_{\mathrm{e}} \rangle \dot{q}_{\mathrm{CD}}$, where γ_{CD} defines the global normalized current drive efficiency. In the case of NBI fuelling, a scaling law reported by Johner [23] relates γ_{CD} with the volume-averaged electron temperature $\langle T_{\mathrm{e}} \rangle$, yielding values around 0.3–0.4 (10^{20} A W^{-1} m^{-2}) for DEMO temperature profiles.

Finally, based upon the calculation of $j_{\parallel}$ from $E_{\parallel}$, j_{BS} and j_{CD} in equation (20), the safety factor profile can readily be computed as:

$$q(\rho) = \frac{g_2(\rho)\, g_3(\rho)\, F(\rho)}{8\pi^3 \mu_0 I_{\mathrm{tor}}(\rho)}, \tag{24}$$

with q being used in the fixed-boundary equilibrium model (equation (6)).

3.3.3. 2D equilibrium solver. PLASMOD incorporates a 2D GSE solver implemented in the EMEQ equilibrium code [55] that is based on a three-moment approach (3M) [56]. Accordingly, the plasma configuration is assumed to be up-down symmetric and each magnetic surface can be parameterized as a function of the Grad–Shafranov shift $\Delta(\rho)$, elongation $\kappa(\rho)$ and triangularity $\delta(\rho)$. Accordingly, the boundary conditions are specified prescribing $R_0, a, \Delta_{\mathrm{E}}, \kappa_{\mathrm{E}}$ and δ_{E}, where the subscript 'E' refers to the plasma boundary, i.e., $\rho = \rho_{\mathrm{b}} = 1$.

3.3.4. 0D SOL/divertor model. The model in [49] is used to calculate the divertor heat flux q_{div} based on P_{sep} and n_{sep} from the 1D transport solver and some engineering assumptions on the divertor geometry and on flux the expansion from the mid-equatorial plane to the divertor targets. These aspects affect the wetted area in the calculation of the heat flux and depend both on the magnetic field configuration (namely on the ratio between poloidal and toroidal components) and the divertor geometry. In general, the peak heat flux q_{div} scales with the upstream parallel heat flux, such that:

$$q_{\parallel,\mathrm{up}} \propto \frac{P_{\mathrm{sep}}}{R_0 \lambda_q \left(\frac{B_{\mathrm{p}}}{B_{\mathrm{T}}}\right)_m}, \tag{25}$$

where λ_q is the power decay length (calculated employing the Eich scaling [57]) and $\left(B_{\mathrm{p}}/B_{\phi}\right)_m$ is the ratio between the poloidal and toroidal component of the magnetic field at the separatrix on the equatorial mid-plane, evaluated at $(r = R_0 + a, z = 0)$ for the outboard side and $(r = R_0 - a, z = 0)$ for the inboard side. $\left(B_{\mathrm{p}}/B_{\phi}\right)_m$ is calculated in the equilibrium module. See [49, 58] for details and references therein.

In PLASMOD, the SOL and the core regions are connected through their mass and energy flows. If a maximum heat flux $q_{\mathrm{div,max}}$ is set as input, in argon gas is seeded in the plasma edge to protect the targets by dissipating such power through radiation. In turn, this affects the impurity contents in the core, too, and influences the power output via fuel dilution.

3.3.5. Integration of PLASMOD into MIRA. The 2D equilibrium solver and the 1D core/SOL transport solvers are coupled and run iteratively in PLASMOD. From the equilibrium resolution, the 1D solver inherits the metric coefficients V', g_2, g_3 and the radial profiles ρ. The equilibrium solver gets from the transport solvers the kinetic profiles p, j_{BS}, j_{CD}, and q. Convergence criteria are placed on the iteration errors calculated for the kinetic profiles ($n_{\mathrm{e}}, T_{\mathrm{e}}$ and T_{i}) and on the safety factor to complete the iteration loop.

Apart from a set of required numerical settings (e.g., iteration errors, max number of iterations, etc), the following key input parameters are required to run a PLASMOD configuration:

- Plasma geometry: $R_0, A, \kappa_{95}, \delta_{95}, B_{\mathrm{t}}, q_{95}$.
- Plasma composition: $f_{\mathrm{D}}, f_{\mathrm{P2E}}, c_{\mathrm{H}}, c_{\mathrm{W}}, c_{\mathrm{Ar}}, c_{\mathrm{Xe}}$.
- Plasma profile properties at separatrix and pedestal: $\rho_{\mathrm{ped}}, f_{\mathrm{GW,ped}}, f_{\mathrm{GW,sep}}, T_{\mathrm{sep}}$.
- Mean location $\overline{\rho}$ and standard deviation σ_{ρ} to describe the Gaussian distribution of fueling and heating sources.
- Fixed additional heating power P_{heat} that is not modified by any of the additional constraints on P_{aux} as described below.

Additional input parameters can be set by the user to allow PLASMOD to constrain a set of plasma targets and operational limits. Some of them are fixed, whereas some others are enabled on demand. In turn, based on these specifications, PLASMOD tunes certain control parameters during the transport/equilibrium iterations to match the required conditions. These are summarized as follows:

- calculate I_{p} to match q_{95}^{t}, where the superscript 't' refers to a target value (fixed)
- calculate δ_{E} and κ_{E} to constrain δ_{95}^{t} and κ_{95}^{t} (fixed)
- adjust a to constrain the plasma volume to a target value $V_{\mathrm{p}}^{\mathrm{t}}$ (optional)
- tune P_{add} (in form of CD power) to fix the loop voltage to a target value $U_{\mathrm{loop}}^{\mathrm{t}}$ (optional)
- increase c_{Xe} and P_{add} to constrain the ratio $f_{\mathrm{LH}} = \frac{P_{\mathrm{sep}}}{P_{\mathrm{LH}}}$ within a prescribed interval given by an upper and a lower limit, $f_{\mathrm{LH,max}}$ and $f_{\mathrm{LH,min}}$, normally around 1.1–1.2 [24, 42] to ensure H-mode operation. P_{LH} is the L–H transition power (Martin's scaling law [59] employed). Accordingly, P_{add} is turned on if $f_{\mathrm{LH}} < 1.1$, while c_{Xe} is puffed if $f_{\mathrm{LH}} > 1.2$ ($f_{\mathrm{LH,max}}$ and $f_{\mathrm{LH,min}}$ are optional inputs)
- control c_{Xe} to observe the limits posed on the divertor challenging criteria expressed as $\frac{P_{\mathrm{sep}}}{R_0} < \left.\frac{P_{\mathrm{sep}}}{R_0}\right|_{\mathrm{max}} \sim 17$ MW m^{-1} [18] and/or $\frac{P_{\mathrm{sep}} B_{\mathrm{t}}}{q_{95} A R_0} \leqslant \left.\frac{P_{\mathrm{sep}} B_{\mathrm{t}}}{q_{95} A R_0}\right|_{\mathrm{max}} \sim 9.2$ MW T m^{-1} [43]. The given limits are representative values for a 2 GW fusion power machine operating in H-mode (optional)
- control P_{add} to constrain a target fusion power $P_{\mathrm{fus}}^{\mathrm{t}}$ (optional)
- increase c_{Ar} to constrain $q_{\mathrm{div}} \leqslant q_{\mathrm{div,max}}$, where $q_{\mathrm{div,max}}$ can be set as an optional input parameter.

The integration of PLASMOD into MIRA is done by passing to the pre-compiled PLASMOD routine the input files from the MIRA data structure, running PLASMOD during a MIRA run and reading the calculated scalar parameters and profiles.

The connection point between the MIRA and PLASMOD framework lies within the 2D fixed boundary equilibrium, where $p(x)$ and $q(x)$ are obtained from the 1D transport resolution. The built-in PLASMOD equilibrium solver relies on a fully analytical resolution method, hence much faster than the 2D equilibrium model based on the FEM approach. This makes it very adequate for multiple iterations with the

transport solution and that is the reason why the FEM equilibrium is not used for such purposes. On the other hand, the EMEQ solver cannot handle the asymmetric shapes of elongated plasma, unlike the 2D FEM model. Therefore, the disparities between the plasma geometries modelled by MIRA's and PLASMOD's fixed-boundary equilibrium models might lead to small (though non-negligible) inconsistencies in the integral plasma parameters. For instance, when calculating the integral power terms by integrating the kinetic profiles calculated in the PLASMOD transport solver over the 1D volume profiles calculated in the 2D FEM equilibrium solver, mismatches around 5%–10% in the integral powers have been found, for plasmas having the same value $R_0, A, \kappa_{95}, \delta_{95}$. Hence, to enhance the consistency between the elongated asymmetric plasmas modelled in the FEM equilibrium and EMEQ solvers, the constraint on the plasma volume V_p^t has been recently added to PLASMOD, and used in the following iteration scheme, which depicts the integration scheme of PLASMOD into MIRA. At each iteration step, the edge elongation and triangularities are known from the previous iteration $\left(\kappa_{X,\mathrm{u}}^{(k-1)}, \kappa_{X,\mathrm{l}}^{(k-1)}, \delta_{X,\mathrm{u}}^{(k-1)}, \delta_{X,\mathrm{l}}^{(k-1)}\right)$, as well as the pressure and safety factor profiles $\left(p^{(k-1)}, q^{(k-1)}\right)$. Accordingly, the following iterations are performed to integrate PLASMOD into MIRA:

(a) Solve 2D FEM fixed-boundary for the plasma shape and the plasma profiles from the previous iteration, $\partial\mathcal{D}_\mathrm{p}^{(k-1)}$ and $(p^{(k-1)}, q^{(k-1)})$, following all the steps in the iteration scheme reported in appendix A.1.
(b) Get $\kappa_{95}^{(k)}$, $\delta_{95}^{(k)}$ and $V_\mathrm{p}^{(k)}$ from the 2D FEM equilibrium solution.
(c) Run PLASMOD with inputs parameters $\left(\kappa_{95}^\mathrm{t}\right)^{(k)} = \kappa_{95}^{(k)}$, $\left(\delta_{95}^\mathrm{t}\right)^{(k)} = \delta_{95}^{(k)}$ and $\left(V_\mathrm{p}^\mathrm{t}\right)^{(k)} = V_\mathrm{p}^{(k)}$ to solve 1D transport + 2D equilibrium (3M) and obtain the new pressure and safety factor profiles, $p^{(k)}$ and $q^{(k)}$.
(d) Recalculate new values of $\kappa_{X,\mathrm{u}}^{(k)}, \kappa_{X,\mathrm{l}}^{(k)}, \delta_{X,\mathrm{u}}^{(k)}, \delta_{X,\mathrm{l}}^{(k)}$ to constrain $\kappa_{95}^{(k)}$ and $\delta_{95}^{(k)}$ to their absolute target values κ_{95}^t and δ_{95}^t.
(e) Update the plasma shape $\partial\mathcal{D}_\mathrm{p}^{(k-1)} \leftarrow \partial\mathcal{D}_\mathrm{p}^{(k)}$, the pressure $p^{(k-1)} \leftarrow p^{(k)}$ and the safety factor profile $q^{(k-1)} \leftarrow q^{(k)}$.
(f) Repeat all steps above until convergence on $\kappa_{95}^{(k)}, \delta_{95}^{(k)}$ and V_p^k is found.

Note that the coupled 2D fixed-boundary equilibrium + PLASMOD package is a built-in step of a whole FBE/transport problem, as outlined in step (f) of the iteration scheme reported in section 3.2.2, denoting the holistic view of the whole physics/engineering solution. The flowchart of figure 6 resembles the entirety of the fully coupled transport and FBE problem.

3.4. Plasma scenario

A FPP operating in pulsed mode relies on distinct phases, each characterized by a specific functional role. The design of the PF/CS coil systems is primarily focused on three main time frames during the pulse: plasma breakdown (BD), start of flat-top (SOF) and end of flat-top (EOF). The time evolution of the currents in the coils defines a plasma scenario [60]. Over the different scenario time frames, the PF/CS coils system shall cope with rather diverse operational demands, expressed as flux and field on radial poloidal prescribed spots.

At the plasma BD the poloidal flux on a prescribed BD point $\mathbf{X_{BD}} = (r_\mathrm{BD}, z_\mathrm{BD})$ is maximized and a max stray field area $\partial\mathcal{D}_\mathrm{BD}^\mathrm{t}$ around $\mathbf{X_{BD}}$ is targeted with the same set of current, force and field technological constraints. Every point within $\partial\mathcal{D}_\mathrm{BD}^\mathrm{t}$ is required to have a poloidal field B_p below the maximum stray field $B_\mathrm{stray}^\mathrm{max}$ (∼3 mT [12]). In more practical terms, the PF/CS coil configuration is found resolving the optimization problem of equation (7) without the flux and field contributions from the plasma, and modifying the objective function $\mathcal{L}$ such that $\mathcal{L}(\boldsymbol{I_c}) = -\Psi_\mathrm{BD}(\boldsymbol{I_c})$, where Ψ_BD is the poloidal field calculated at $\mathbf{X_{BD}}$. Note that minimizing the negative part of a function is equivalent to its maximization. Additionally, the equality constraints on the X-point are removed and the inequality constraints on a selected number of points N_BD on $\partial\mathcal{D}_\mathrm{BD}^\mathrm{t}$ (considered to be circular around $\mathbf{X_{BD}}$ with a BD area radius $\rho_\mathrm{BD} \sim 2$–3 m), such that the poloidal field on each point k is lower than the max stray field, i.e. $B_{\mathrm{p},k}(\boldsymbol{I_c}) < B_\mathrm{stray}^\mathrm{max}$, for $k = 1, \ldots, N_\mathrm{BD}$.

At SOF and EOF the complete FBE problem is solved for two prescribed plasma boundary fluxes: $\Psi_\mathrm{b,SOF}$ and $\Psi_\mathrm{b,EOF}$, respectively. Both are set as target values $\Psi_\mathrm{b}^\mathrm{t}$ in equation (8). $\Psi_\mathrm{b,SOF}$ is computed from the peak poloidal flux Ψ_BD achieved during the plasma BD and the flux consumed during the plasma ramp-up, composed of an inductive and a resistive component, Ψ_ind and Ψ_res. $\Psi_\mathrm{res} = c_\mathrm{Ejima}\mu_0 I_\mathrm{p} R_0$ and $\Psi_\mathrm{ind} = \frac{1}{2}\mu_0 l_\mathrm{i} I_\mathrm{p} r_\mathrm{ax}$ are calculated as per Ejima scaling [61], as a function of the Ejima coefficient $c_\mathrm{Ejima} \sim 0.3$–$0.4$ (input), l_i, I_p and radial location of the plasma magnetic axis r_ax, calculated from the FBE. Finally, $\Psi_\mathrm{b,SOF}$ reads as:

$$\Psi_\mathrm{b,SOF} = \Psi_\mathrm{BD} - c_\mathrm{Ejima}\mu_0 I_\mathrm{p} R_0 - \frac{1}{2}\mu_0 l_\mathrm{i} r_\mathrm{ax} I_\mathrm{p}. \tag{26}$$

The boundary flux at EOF $\Psi_\mathrm{b,EOF}$ is manually minimized from $\Psi_\mathrm{b,SOF}$ to a feasibly achievable value in line with the imposed operational plasma shaping requirements $\left(\delta_{95}^\mathrm{t}, \kappa_{95}^\mathrm{t}, R_0, A, V_\mathrm{p}\right)$ and coils technology constraints.

Once $\Psi_\mathrm{b,SOF}$ and $\Psi_\mathrm{b,EOF}$ are known, U_loop is used to determine the maximum flat-top length $\tau_\mathrm{flat}^\mathrm{max}$, i.e., the maximum time duration where a constant plasma current I_p can be maintained within a plasma pulse with a given set of PF/CS technological limits. As a first approximation $\tau_\mathrm{flat}^\mathrm{max}$ is equal to the max burn time $\tau_\mathrm{burn}^\mathrm{max}$, i.e., the timeframe where a constant fusion power P_fus is established. $\tau_\mathrm{flat}^\mathrm{max}$ is computed from the definition of U_loop of equation (22), such that:

$$\tau_\mathrm{burn}^\mathrm{max} \approx \tau_\mathrm{flat}^\mathrm{max} = \frac{\Psi_\mathrm{b,SOF} - \Psi_\mathrm{b,EOF}}{U_\mathrm{loop}}. \tag{27}$$

Note the overlapping of physics and engineering dependencies on $\tau_\mathrm{burn}^\mathrm{max}$ coming from core plasma transport and equilibrium properties $(I_\mathrm{p}, l_\mathrm{i}, n_\mathrm{e}, T_\mathrm{e}, T_\mathrm{i}, I_\mathrm{BS})$ and technological features (P_CD, coil sizes, positions and limits). Most importantly, a DEMO top-level requirement is indeed posed on long-pulse DEMO devices, such that $\tau_\mathrm{burn} \geqslant 2$ h [17].

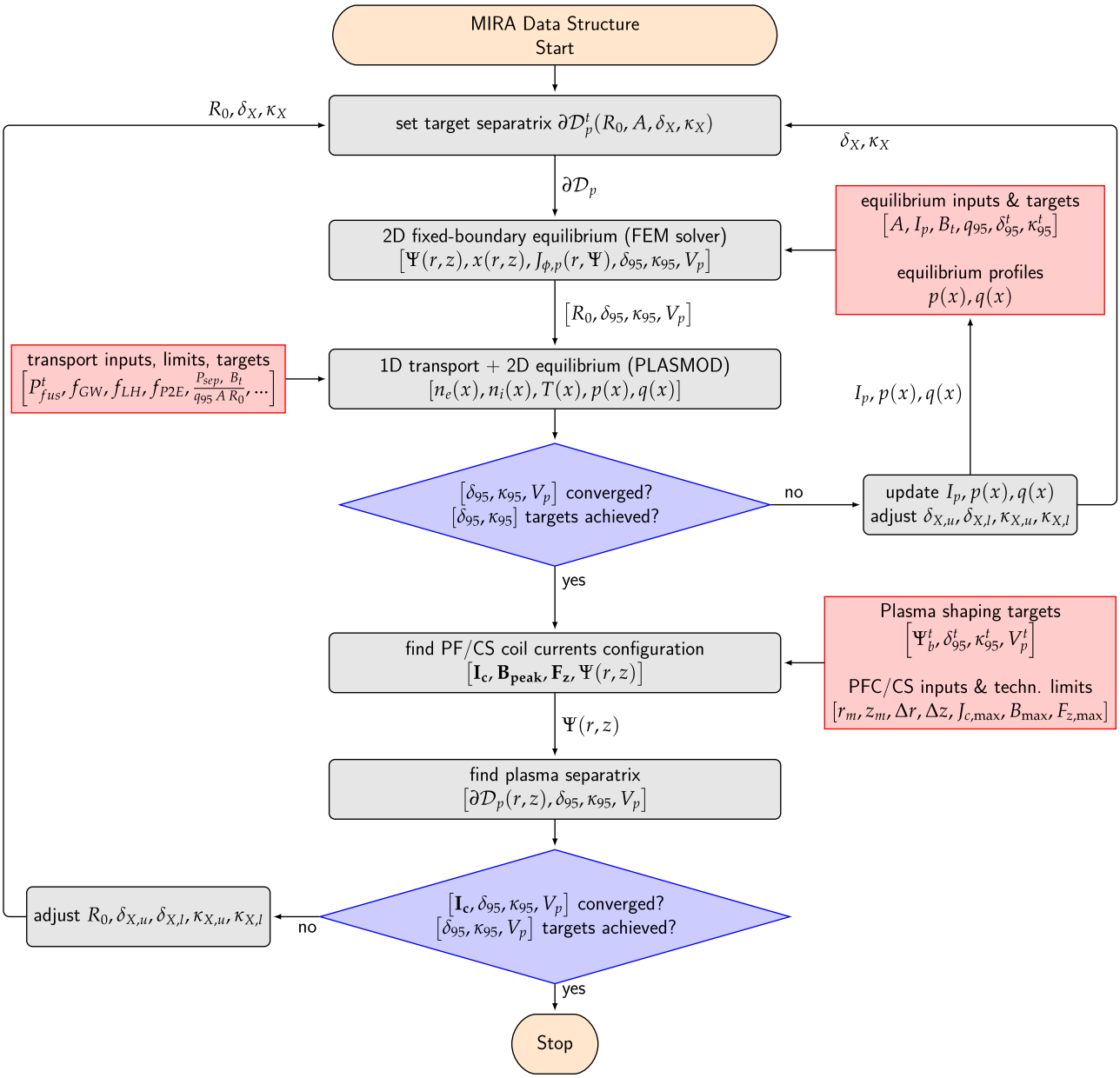

Figure 6. Flowchart for the coupling of fixed-boundary equilibrium, 1D MHD transport physics and PF/CS coil current solvers, denoting the fully coupled transport-FBE solver of MIRA. Each block is characterized by its shape: ovals relate to start and stop nodes, sharp-corner rectangles indicate inputs, round-corner-rectangles denote process steps and diamonds refer to process decisions.

3.5. Reactor neutronics

A neutron-gamma radiation transport model for tokamak configurations has been implemented in MIRA for a fast calculation of tritium breeding, nuclear heating, neutron shielding capabilities of the physical reactor components. The transport problem is addressed by solving the steady-state Boltzmann transport equation (BTE), where the distribution of the angular flux density $\psi(\boldsymbol{r}, \boldsymbol{\Omega}, E)$ in the space ($\boldsymbol{r}$), angle ($\boldsymbol{\Omega}$) and energy (E) phase space is the unknown function. In MIRA, the BTE is solved numerically discretizing E and $\boldsymbol{\Omega}$ as per multi-energy group and discrete ordinate approximations (reference [62], pp 61 and 117). Accordingly, the transport problem is solved along a selected number N of angular directions $\boldsymbol{\Omega}_{\boldsymbol{n}}$ (S_N discrete ordinate approximation), and a number G of energy groups $g = [E_g, E_{g-1}]$. As a result, the solution ψ is sought for all angular flux density scalar functions ψ_n^g defined for all $n = 1, \ldots, N$ and $g = 1, 2, \ldots, G$. Finally, the set of BTEs reads as:

$$\begin{cases} \left(\hat{\boldsymbol{H}}_n^g(\boldsymbol{\Omega}_{\boldsymbol{n}}) + \Sigma_t^g\right)\psi_n^g(r,z) = \dot{q}_{\text{ext}}^g(r,z) + \hat{\boldsymbol{L}}_n^g\left(\boldsymbol{\Omega}_{\boldsymbol{n}}, \Sigma_{s,l}^{g'\to g}\right)\psi_n^g(r,z) \\ \psi_n^g|_{\partial\mathcal{D}_-} = 0 \end{cases} \tag{28}$$

where $\hat{\boldsymbol{H}}_n^g$ and $\hat{\boldsymbol{L}}_n^g$ are the streaming first-order differential operator and the integral scattering operator of the BTE in 2D curvilinear geometry, under discrete ordinate and multi-group approximation (reference [62], pp 79 and 176). $\partial\mathcal{D}_- \{r, z \in \partial D | \boldsymbol{\Omega}_{\mathbf{n}} \cdot \mathbf{n} < 0\}$ is the inflow boundary (with

related vacuum boundary condition), and $\mathbf{n}$ is the unit outward normal field on the boundary ∂D. $\Sigma_t^g(r,z)$ is the total macroscopic nuclear cross-section and $\Sigma_{s,l}^{g'\to g}$ is the angular moment of the differential scattering macroscopic cross-section from all groups $g' \neq g$ to the group g. $\dot{q}_{\text{ext}}^g$ is the external neutron (or photon) source (assumed isotropic in the angular direction). Σ_t^g and $\Sigma_{s,l}^{g'\to g}$ depend on the atomic densities and the isotope compositions of the materials characterizing the reactor components, i.e., the volumetric fraction of each material mixture (e.g., EUROFER, coolant, breeder, etc). In general, the macroscopic cross-section Σ_x associated with the neutron interaction x is obtained by multiplying the microscopic cross-section $\sigma_{x,i}$ of the isotope i to the atomic density n_i such that

$$\Sigma_x(r,E,\mathbf{\Omega}) = \sum n_i(\boldsymbol{r}) \cdot \sigma_{x,i}(E,\mathbf{\Omega}). \tag{29}$$

The fusion-evaluated nuclear data library [63] are recommended for fusion neutronics [64] and are deployed in MIRA for neutron transport analyses.

The neutron and photon sources are calculated in the core plasma physics module from 1D transport solution as radial profiles along the normalized radial coordinate x and are mapped onto the 2D normalized flux distribution $x(r,z)$ from the 2D magnetic configuration. Hence, $\dot{q}_{\text{ext}} \equiv \dot{q}_{\text{neut}} = 4/5\dot{q}_{\text{fus}}$ for neutrons (equation (14)) and $\dot{q}_{\text{ext}} = \dot{q}_{\text{rad}}$ for photon radiations (equation (15)). The ordinates $\mathbf{\Omega_n}$ are associated with the quadrature formula used to integrate ψ_n^g over $\mathbf{\Omega}$, such that $\int \psi \,\mathrm{d}\Omega \approx \sum w_n \psi_n$. The level-symmetric quadrature set has been chosen for the resolution tokamak neutronics problem in MIRA systems analyses.

Based on the resolution of equation (28), the tritium breeding, nuclear power deposition, neutron shielding and atomic displacement damage features are calculated from reaction rates and other integral and local parameters, listed below:

- Scalar flux $\phi(r,z,E) = \int \psi(r,z,E,\mathbf{\Omega})\mathrm{d}\mathbf{\Omega}$.
- Net current $j_n = \int \boldsymbol{n}\cdot\mathbf{\Omega}\psi(r,z,E,\mathbf{\Omega})\,\mathrm{d}\mathbf{\Omega}$.
- Fast neutron flux $\Phi_{\text{fast}}(r,z) = \int_{0.1\text{MeV}}^{+\infty}\phi(r,z,E)\,\mathrm{d}E$ and total neutron flux $\Phi_{\text{fast}}(r,z) = \int_0^{+\infty}\phi(r,z,E)\,\mathrm{d}E$.
- Local volumetric reaction rate $\mathcal{R}_x(r,z) = \int_0^{+\infty}\Sigma_x(r,z,E)\,\phi(r,z,E)\,\mathrm{d}E$.

The whole neutronic model splits into two submodules:

- a two-dimensional neutron/gamma transport resolution for a plasma + SOL void domain, and
- a one-dimensional model for the radial streaming of neutron and gamma rays across the core reactor components.

3.5.1. A 2D model for the radiation transport across the torus chamber. In the 2D model, the union of plasma and SOL domains $\mathcal{D}_{\text{p}}$ and $\mathcal{D}_{\text{SOL}}$, obtained from the geometry module, is addressed as void computing domain, with $\Sigma_t^g = \Sigma_{s,l}^{g'\to g} = 0$. The domain $\mathcal{D} = \mathcal{D}_{\text{p}} \cup \mathcal{D}_{\text{SOL}}$ is enclosed by the boundary $\partial\mathcal{D} = \partial\mathcal{D}_{\text{FW}} \cup \partial\mathcal{D}_{\text{DIV}}$, where $\partial\mathcal{D}_{\text{FW}}$ and $\partial\mathcal{D}_{\text{DIV}}$ denote the FW and the divertor contours facing the plasma (see figure 7).

The 2D BTE is solved both for $\dot{q}_{\text{neut}}(r,z)$ and $\dot{q}_{\text{rad}}(r,z)$. For its numerical solution, the FEM discontinuous Galerkin method (DGM) has been deployed with a dedicated model

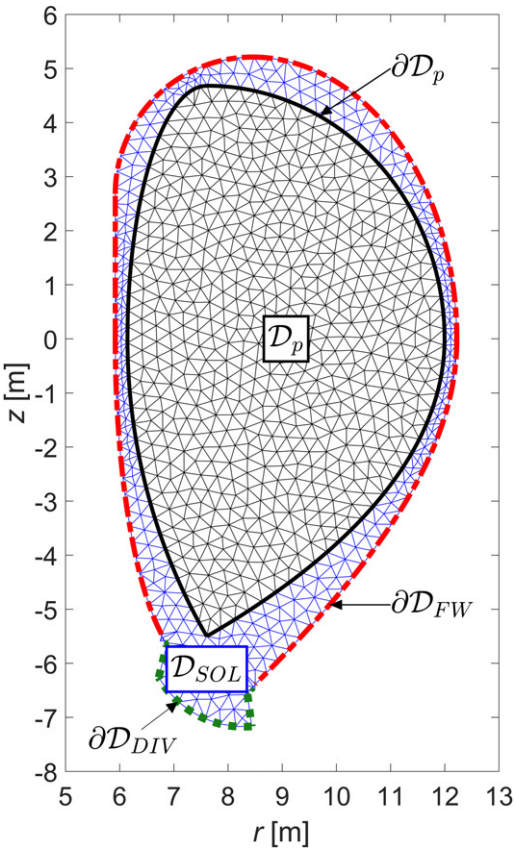

Figure 7. Graphical representation of plasma + SOL void domain used for the 2D neutron and photon radiation transport model implemented in MIRA. Reproduced with permission from [13].

implemented in FreeFEM++ and integrated into MIRA. Accordingly, the neutron and photon wall loads onto blanket first wall and divertor structures are mapped with the imposed BB and divertor geometric poloidal profiles. From the resolution of all $\psi_n(r,z)$ (group superscript omitted), and from the calculation of the net current j_n, the power load from the neutron or photon source k onto the boundary portion j (with $j = \text{FW}, \text{DIV}$) is calculated as

$$P_j^k = \int_{\partial\mathcal{D}_j} j_n^k(r,z)\,2\pi r\,\mathrm{d}l, \tag{30}$$

with $k = n,\gamma$ and $j = \text{FW},\ \text{DIV}$. Here, $\mathrm{d}l$ is the infinitesimal length along $\partial\mathcal{D}_j$. Similarly, the poloidal distribution $\Gamma_\perp^k(\alpha_w)$ of the neutron and photon power loads on a poloidal coordinate α_{w} can be defined. α_{w} is oriented counter-clockwise along the boundary $\partial\mathcal{D}$ and indicates the poloidal angular position of the infinitesimal wall area $\delta\mathcal{D}_{\text{w}}$ on FW and divertor surfaces. Accordingly, $\Gamma_\perp^k$ is given by:

$$\Gamma_\perp^k(\alpha_{\text{w}}) = \frac{\int_{\delta\mathcal{D}_{\text{w}}} j_n^k(r,z)\,2\pi r\,\mathrm{d}l}{\int_{\delta\mathcal{D}_{\text{w}}} 2\pi r\,\mathrm{d}l}, \tag{31}$$

with $0 \leqslant \alpha_{\text{w}} \leqslant 2\pi$. An upper limit of 1 MW m^{-2} [65] is set for $\Gamma_\perp^\gamma$ on the FW ($\Gamma_{\perp,\text{FW}}^\gamma$), since the heat flux from the plasma radiation represents a localized power surface deposition that

can compromise the structural integrity and cooling of the plasma-facing components.

A V & V study has been addressed to outline the major errors introduced by the model (see [13] for technical details and references therein). In short, the verification part included a comparison of a flux density distribution against some analytical solutions (e.g., for a square domain), while a separate validation study has been conducted against Monte Carlo (MC) solutions. Therein, deterministic and stochastic analyses have been carried out comparing the poloidal distribution of $\Gamma^n_\perp(\alpha_w)$ calculated for a solution domain with the plasma shape parameters and volumetric sources inherited from the EU-DEMO 2015 baseline [18] and a surrounding FW/divertor shape assumed for simplicity up-down symmetric and taking a SOL radial thickness equal to 22.5 cm, and a vertical thickness equal to 50 cm. The major goal was mainly to quantify the error arising from the spatial and angular discretization. The verification study resulted in a set of guidelines to build the 2D mesh, with a mesh refinement ensuring a numerical error (in the integral L_2 norm definition) below a certain threshold value ($\sim$0.1%). The validation study yielded the local relative error on $\Gamma^n_\perp(\alpha_w)$ against the MC solution, leading to peak local deviations below 1% for $\alpha_w \in [0, 2\pi]$. Also, a major conclusion of such a study is that at least an S_{14} approximation is necessary to have a local relative error below 1% across the α_w domain.

Furthermore, to prove the versatility of the model for its application to tokamak geometry configurations far from the EU-DEMO 2015 baseline, a wider range of values of R_0 (7.5–10.5 m) and A (2.6–3.6) were addressed using the same MC model. The analyses yielded numerical errors very close to those obtained for the EU-DEMO 2015 baseline. A detailed description of the whole validation study is reported in [13].

3.5.2. A 1D model for the radiation transport across the physical reactor components. In the 1D neutronics model, the neutron and photon streaming across the reactor components, including their material composition, is solved along the radial direction r. Accordingly, a one-dimensional cylindrical approximation is made. The solution of the BTE $\psi^g_n(r)$ is then found for all ordinates N and energy groups G. The ANISN deterministic code [66] has been interfaced with MIRA to fulfil this task. ANISN calculates the space/energy/angle neutron and photon flux density spectrum for any arbitrary radial and material composition of the core physical reactor components, including BB, VV, gaps and TF coils. The neutronic model calculates the reaction rates needed for the nuclear design of the reactor. These are inherited from the in-group scalar neutron flux $\phi_g(r) = \sum w_n \psi^g_n(r)$, where w_n indicate the weights of the discrete ordinates quadrature formula. The radial profiles of $\phi_g(r)$ are properly mapped onto a 2D radial/vertical grid, such that $\phi^{1D}_g(r) \rightarrow \phi^{2D}_g(r,z)$. From $\phi^{2D}_g(r,z)$, all relevant reaction rates are calculated. In particular, the following key parameters are calculated in the MIRA's neutronics module.

The tritium breeding ratio (TBR) is a key reactor design parameter and is defined as:

$$\mathrm{TBR} = \frac{1}{\mathcal{B}_p}\int_{\mathcal{D}_{BZ}} \mathcal{R}_{nt}(r,z) 2\pi r \,\mathrm{d}r\,\mathrm{d}z, \tag{32}$$

with $\mathcal{R}_{nt} = \sum_g \Sigma^g_{n\rightarrow T}\phi_g$ indicating the local tritium production rate, $\Sigma^g_{n\rightarrow T}$ the macroscopic tritium breeding reactions from neutron captures of ^{6}Li and ^{7}Li atoms, $\mathcal{D}_{BZ}$ the breeding zone (BZ) domain and $\mathcal{B}_p \propto P_{fus}$ the tritium burn-up in the plasma. A key DEMO requirement is posed on the TBR for DEMO [67], for as the so-called target TBR $\mathrm{TBR}_t \geqslant 1.15$ needs to be achieved to attain tritium self-sufficiency. This value includes a design margin from the required TBR TBR_r, i.e., the TBR at the interface between the T extraction systems and the tritium plant. Such a design margin accounts for non-breeding components which deplete the T breeding, such as limiters, auxiliary heating systems and diagnostics.

The nuclear heating deposition R^m_{heat} into the materials of the reactor component reads as:

$$R^m_{heat} = \int_{\mathcal{D}_m} \mathcal{R}^m_{heat} 2\pi r \,\mathrm{d}r\,\mathrm{d}z, \tag{33}$$

with $\mathcal{R}^m_{heat}(r,z) = \sum k^g_{heat}(r)\,\phi_g(r,z)$ being the nuclear power density, k^g_{heat} the KERMA factor (kinetic energy released in materials), and $\mathcal{D}_m$ the domain of the component m.

Neutron shielding requirements are observed to protect the superconducting coils and to limit the neutron irradiation damage to structural and functional materials. The shielding limits associated with the TF coils operation [68] are posed on the peak volumetric heating $\mathcal{R}^{TFC}_{heat,peak} \leqslant 50\ \mathrm{W\,m^{-3}}$ and on the peak fast neutron flux $\phi^{TFC}_{fast,peak} \leqslant 10^9\ \mathrm{cm^{-2}\,s^{-1}}$, defined as:

$$\phi^{TFC}_{fast,peak} = \sum_{g_{0.1}}^{g_{14}} \phi_g\left(r^{IB}_{TFC}\right), \tag{34}$$

where r^{ib}_{TFC} indicates the innermost radial location of the TF coil's conducting region, and $g_{0.1}$ and g_{14} the group indexes envelop the energy interval between 0.1 MeV and 14.1 MeV, identifying the fast neutron spectrum [69].

A V & V study has been conducted to quantify the major error arising from the approximations taken in the 1D model, as well (see [13] for implementation details and references). These are:

- numerical error associated with the radial nodalization, discrete ordinates quadrature formula and multi-group energy approximation,
- cylindrical geometry against actual toroidal tokamak topology and,
- material mixture homogenization.

In actual 3D tokamak reactor configurations, the neutron/gamma streaming is affected by radial, poloidal and toroidal heterogeneities, which in a homogenized model cannot depict. There are also neutron streaming effects through void gaps in the toroidal direction which have to be accounted for by the actual three-dimensional geometry. To assess each error contribution dedicated simulation campaigns have been carried out. However, of key importance are the overall uncertainties affecting the TBR and the nuclear heating in BB, VV and TFC, as well as the peak nuclear power density and fast neutron fluence in the inboard TFC for shielding purposes. The

Table 1. Top-level requirements and major design features of the EU-DEMO 2017 baseline.

EU-DEMO top-level requirements
Net electric power $\dot{W}_{\text{net}} \sim 300$–$500$ MW [1, 79]
Tritium self-sufficiency, $\text{TBR}_{\text{t}} \geqslant 1.15$ [67]
Inductive long pulse operation mode, $\tau_{\text{burn}} \geqslant 2$ h [1, 79]
EU-DEMO major design features
Single-null divertor configuration and 16 TF coils/reactor sectors [2]
Plasma major radius $R_0 = 8.94$ m, aspect ratio $A = 3.1$ [2]
Fusion power $P_{\text{fus}} \sim 2000$ MW and additional heating power $P_{\text{add}} \sim 50$ MW
Two driving blanket designs [80]: helium-cooled pebble beds (HCPB) [81, 82] and water-cooled lithium lead (WCLL) [83, 84]
Two BoP/PCS for the two aforementioned BB designs, with $\eta_{\text{gross}} \sim 37.7\%$ for HCPB [77] and $\eta_{\text{gross}} \sim 35\%$ for WCLL [77]
Low-temperature TF and PF coils' superconductors, with Nb_3Sn superconducting material in TF coils and CS elements, and NbTi in the PF coils. For such a coil technology, $B_{\text{max}} = 12.23$ T for the TF coils [85], $B_{\text{max}} = 13.7$ T for the CS [85, 86]) and $B_{\text{max}} = 5.7$ T for PF coils [29]
Wall plug efficiency $\eta_{\text{add}} = 40\%$ [18, 79]

V & V study for the 1D model has been conducted against MC solution, consisting of three major parts:

- Comparison against a dedicated 1D MC solution on a radial and material mix inherited from the EU-DEMO 2015 baseline [70] (HCPB blanket concept), to measure the error associated with the numerical approximation.
- Comparison against a dedicated 2D MC model to evaluate the uncertainties introduced by the cylindrical approximation (against toroidal) for the same reactor configuration.
- Comparison against the 3D heterogeneous MC neutronics model of the same EU-DEMO baseline [69, 71].

The V & V study showed a global error of around +8% for the TBR ('+' denotes an overestimation from the reference MC solution), while the nuclear power density at the inner interface of the TF coil WP yields peak local errors around + 38%. Generally, the one-dimensionality yields the deviation of the solution to progressively increasing moving from the plasma centre outward. As a result, both local and integral parameters are more accurate in the vicinity of the plasma domain. The integral and local parameters in the BB are therefore affected by smaller errors. The largest share of the overall nuclear heat deposition derives from that in FW and BZ, where the gap between approximated and exact solutions is approximately +3%–4%. Moving towards the outer BB regions (e.g., manifolds), the error goes up to +20%–30%. In the VV and TFC regions, deviations up to 50%–70% are found. As a result, moving further from the BB, the limitations of the cylindrical approximation become more relevant for toroidal geometry. Accordingly, a full 2D reactor model would be needed if more accurate estimates on the heat deposition to VV and TFC are needed for design purposes. On the other hand, the power contribution of such components to the overall plant power balance is rather small (∼30 MW), hence do not play a crucial role for DEMO plant integral design purposes.

3.6. Toroidal magnetic field configuration

The toroidal magnetic field generated by the TF coils is characterized in MIRA in terms of peak toroidal field ripple on the plasma separatrix, static in-plane and out-of-plane Lorentz force acting on the TF coils and the stored magnetic energy. From integral Ampere's law, assuming that the toroidal field $B_\phi \sim 1/r$ in the plasma region, for a given number of TF coils N_{TFC}, the current to operate in each coil to obtain $B_\phi = B_{\text{t}}$ at $r = R_0$ can be expressed as:

$$I_{\text{c,TFC}} = \frac{1}{N_{\text{TFC}}} \frac{2\pi R_0}{\mu_0} B_{\text{t}}. \tag{35}$$

From the TF coil current and a given superconducting cable design (subject to current and field limits), the total number of turns can be calculated. Hence, the cross-sectional area of the coil's WP, too. The WP cable layout and the radial-poloidal TF shape determine the three-dimensional magnetic field distribution. For a prescribed radial/poloidal and radial/toroidal TF

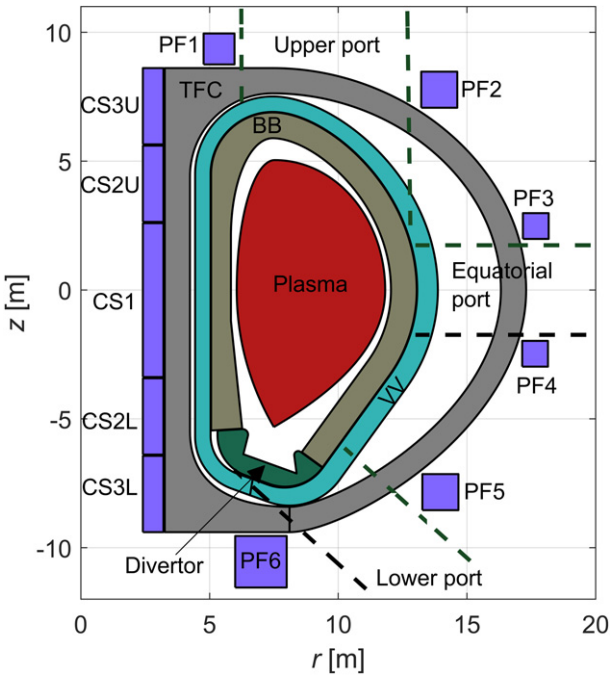

Figure 8. 2D sketch of the EU-DEMO 2017 reactor, as per MIRA geometry module.

Table 2. Calculated plasma geometry and magnetic equilibrium parameters of the EU-DEMO 2017 baseline: comparison between MIRA and PROCESS.

Parameter variable (unit)	MIRA	PROCESS	Deviation (%)	Type
Major radius R_0 (m)	8.938	8.938	0	I
Aspect ratio A (—)	3.1	3.1	0	I
Minor radius a (m)	2.883	2.883	0	O
Elongation at 95% flux κ_{95} (—)	1.6501	1.6500	+0.004	DT ≈ 1.65
Triangularity at 95% flux δ_{95} (—)	0.333 04	0.333 00	+0.013	DT ≈ 0.333
Plasma volume V_p (m^3)	2380	2466	−3.5	O
Plasma cross-sectional area A_p (m^2)	43.81	44.85	−2.3	O
Plasma toroidal surface A_t (m^2)	1352	1419	−4.7	O
Plasma perimeter l_p (m)	24.55	26.02	−5.7	O
Toroidal field at plasma centre B_t (T)	5.31	4.89	+8.6	O
Safety factor at 95% flux q_{95} (—)	3.22	3.00	+7.3	OL $\geqslant 3.0$
Safety factor on the axis q_0 (—)	1.0	1.0	+0.0	OL $\geqslant 1.0$
Plasma current I_p (MA)	19.33	19.08	+1.3	O
Average poloidal field $\overline{B}_p$ (T)	1.22	0.92	+32.0	O
Poloidal plasma beta β_p (%)	92.7	114.1	−18.7	O
Toroidal plasma beta β_t (%)	3.38	4.05	−16.5	O
Normalized beta β_N (%)	2.66	2.89	−8.1	OL $\leqslant 3.51$
Plasma internal inductance l_i (—)	0.88	1.10	−19.9	O

coil geometric and current density configuration $\boldsymbol{J}$, the magnetic field $\mathbf{B}$ at any spatial location in $\mathbf{r}(x, y, z)$ is calculated in MIRA via Biot–Savart equation, reading as:

$$\mathbf{B}(\mathbf{r}) = \frac{\mu_0}{4\pi}\int_{\mathcal{D}_j} \frac{\mathbf{J}\left(\mathbf{r}'\right) \times \left(\mathbf{r} - \mathbf{r}'\right)}{\left|\mathbf{r} - \mathbf{r}'\right|^3} \mathrm{d}\mathbf{r}', \tag{36}$$

with $\mathrm{d}\mathbf{r}'$ denoting the differential volume of any current-carrying element and $\mathcal{D}_j$ the volume domain where $\mathbf{J}$ is defined. The Biot–Savart solver EFFI [72] has been integrated into MIRA and is deployed for 3D magnetostatic analysis. EFFI computes the three-dimensional electromagnetic field distribution for any arbitrary toroidal and poloidal coils system, based on the resolution of equation (36). Also, it allows for the calculation of the Lorentz static forces and mutual inductances.

Based on a 3D mapping of $\mathbf{B}$, the toroidal field ripple measures the oscillations of the toroidal field along the toroidal direction between two adjacent coils, and it is calculated as:

$$\delta_{\mathrm{TF}}\left(\mathbf{p}_k\right) = \frac{\max\left(B_\phi\left(\mathbf{p}_k;\phi\right)\right) - \min\left(B_\phi\left(\mathbf{p}_k;\phi\right)\right)}{\max\left(B_\phi\left(\mathbf{p}_k;\phi\right)\right) + \min\left(B_\phi\left(\mathbf{p}_k;\phi\right)\right)}, \tag{37}$$

where $\mathbf{p}_k = (r_k, z_k)$ indicates any the point k on the radial/poloidal plane and ϕ is the toroidal coordinate defined in the interval $\left[0, \frac{2\pi}{N_{\mathrm{TFC}}}\right]$. Large toroidal field ripples have negative effects on the plasma stability, potentially causing losses of fast alpha particles [3]. Therefore, an upper limit for the peak TF ripple $\delta_{\mathrm{TF,peak}} < 0.6\%$ is currently set for DEMO [18], with $\delta_{\mathrm{TF,peak}}$ denoting the peak value of the set of points $\mathbf{p}_k$ taken on the plasma separatrix. Note that in DEMO this limit is predicated on the use of ferromagnetic inserts placed between the inner and the outer VV shells to reduce it to a smaller value of 0.3% [73]. Since these effects are not yet accounted for, the former, more conservative value is taken as maximum TF ripple on the plasma separatrix.

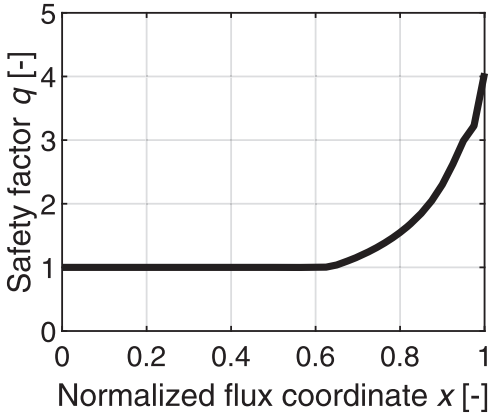

Figure 9. Safety factor profile $q(x)$ of the EU-DEMO 2017 baseline, as per MIRA/PLASMOD transport simulation.

Large static Lorentz forces on the TF structures arise from large fields and current densities. These, in turn, split into the hoop (or in-plane) forces and bending (or out-of-plane) forces. The hoop forces emerge from the interactions of the TF coil current with its magnetic field, whereas the bending forces come from the magnetic coupling of TF currents and the poloidal magnetic field from the PF coils. The volumetric Lorentz forces $\boldsymbol{f}_{\mathbf{L}} = \mathbf{J} \times \mathbf{B}$ is therefore decomposed into radial and vertical in-plane components $f_{x,\mathrm{L}}$ and $f_{y,\mathrm{L}}$ and toroidal/out-of-plane component $f_{y,\mathrm{L}}$, such that $\boldsymbol{f}_{\mathbf{L}} = \hat{\boldsymbol{n}}_{\boldsymbol{x}} f_{x,\mathrm{L}} + \hat{\boldsymbol{n}}_{\boldsymbol{z}} f_{z,\mathrm{L}} + \hat{\boldsymbol{n}}_{\boldsymbol{y}} f_{y,\mathrm{L}}$.

Three integral forces are calculated to depict the static radial, vertical and toroidal loads exerted onto the TF coils.

Table 3. Calculated plasma profiles and impurity parameters of the EU-DEMO 2017 baseline: comparison between MIRA and PROCESS.

Parameter variable (unit)	MIRA	PROCESS	Deviation (%)	Type
Electron density on axis $n_{e,0}$ (10^{19} m^{-3})	10.1	10.4	−3.1	O
Greenwald fraction at pedestal $f_{GW,ped}$ (—)	0.85	0.85	+0.0	OL $\leqslant 0.85$
Electron density at pedestal $n_{e,ped}$ (10^{19} m^{-3})	6.40	6.21	+3.0	O
Greenwald fraction at separatrix $f_{GW,sep}$ (—)	0.5	0.5	+0.0	OL $\leqslant 0.5$
Density at separatrix $n_{e,sep}$ (10^{19} m^{-3})	3.76	3.65	+3.1	O
Volume-averaged electron density $\langle n_e \rangle$ (10^{19} m^{-3})	7.62	7.91	−3.7	O
Electrons temperature on axis $T_{e,0}$ (keV)	32.14	26.67	+20.5	O
Ions temperature on axis $T_{i,0}$ (keV)	27.83	26.67	+4.4	O
Electron/ions temperature at pedestal n_{ped} (keV)	5.36	5.50	−2.5	O
Normalized coordinate of n_e, T_e, T_i pedestal height ρ_{ped} (—)	0.94	0.94	+0.0	I
Electrons/ions temperature at separatrix n_{sep} (keV)	0.10	0.10	+0.0	O
Volume-averaged electrons temperature $\langle T_e \rangle$ (keV)	12.40	12.82	−3.2	O
Volume-averaged ions temperature $\langle T_i \rangle$ (keV)	12.01	12.82	-6.3	O
Particle-to-energy confinement ratio f_{P2E} (—)	5.000	7.106	−29.6	I
Plasma effective charge Z_{eff} (—)	1.912	2.179	−12.2	O
Fuel concentration c_{fuel} (—)	0.871	0.782	+11.7	O
He concentration c_{He} (—)	0.049	0.100	−50.4	O
Xe concentration c_{Xe} (—)	2.29×10^{-4}	3.47×10^{-4}	−34.0	O
Ar concentration c_{Ar} (—)	1.29×10^{-3}	n.a.	n.a.	O
W concentration c_W (—)	5.0×10^{-5}	5.0×10^{-5}	+0.0	I

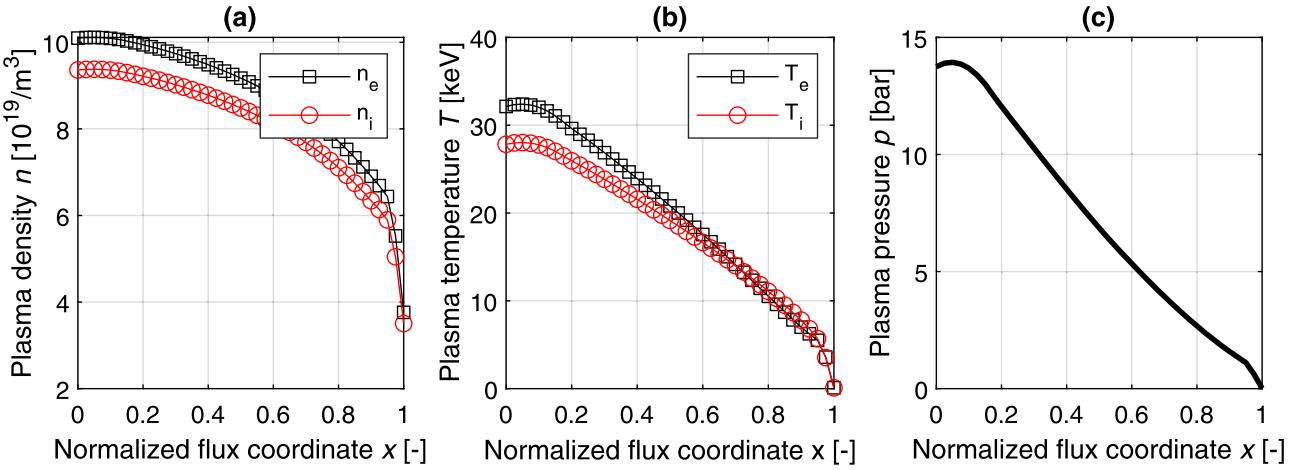

Figure 10. Plasma profiles of the EU-DEMO 2017 baseline, as per MIRA/PLASMOD transport simulation: (*a*) electrons and ions densities, (*b*) electrons/ions temperature, (*c*) total plasma pressure.

These are:

$$F_{x,\mathrm{TFC}} = \int_{\mathcal{D}_{\mathrm{TFC}}} f_{x,\mathrm{L}}\, \mathrm{d}\mathbf{r},$$
$$F_{v,\mathrm{TFC}} = \frac{\left(F^{\mathrm{up}}_{z,\mathrm{TFC}} + \left|F^{\mathrm{down}}_{z,\mathrm{TFC}}\right|\right)}{2}, \qquad (38)$$
$$F_{\mathrm{b,TFC}} = \frac{\left(F^{\mathrm{up}}_{y,\mathrm{TFC}} + \left|F^{\mathrm{down}}_{y,\mathrm{TFC}}\right|\right)}{2}.$$

The integral radial force $F_{x,\mathrm{TFC}}$ represents the net inward centering force that pushes each TF coil towards the tokamak axis, and denotes the predominant component. The vertical force $F_{v,\mathrm{TFC}}$ is outlined as the averaged value between the two vertical forces pulling the top and bottom half-coil up and down, $F^{\mathrm{up}}_{z,\mathrm{TFC}}$ and $F^{\mathrm{down}}_{z,\mathrm{TFC}}$, and leads to an internal tensile load which is mostly borne by the steel jacketing structure of the coil conductor. The vertical force applied to the top or bottom portion of the TF coil domain $\mathcal{D}_j$ reads as $F^{j}_{z,\mathrm{TFC}} = \int_{\mathcal{D}_j} f_{z,\mathrm{L}}\, \mathrm{d}\mathbf{r}$, where $j = \mathrm{up, down}$ refers to the top or bottom portion of the coil. The same approach is adopted to evaluate the bending force $F_{\mathrm{b,TFC}}$, with $F^{j}_{y,\mathrm{TFC}} = \int_{\mathcal{D}_j} f_{y,\mathrm{L}}\, \mathrm{d}\boldsymbol{r}$, which produces a perpendicular force on the coil along the toroidal direction and a torque about the mid-plane. This bending moment is to be counteracted the outer inter-coil structures. Radial, vertical and bending forces denote important inputs to the mechanical characterization of the TF coils, still to be addressed in the MIRA package.

Assuming that all N_{TFC} coils are carried by the same current $I_{\mathrm{c,TFC}}$, the energy stored in the entire TF system is given by

$$E_{m,\mathrm{TFC}} = \frac{1}{2} I^2_{\mathrm{c,TFC}} \sum_j \sum_i \mathcal{M}_{i,j}, \qquad (39)$$

Table 4. Calculated plasma power and confinement parameters of the EU-DEMO 2017 baseline: comparison between MIRA and PROCESS.

Parameter variable (unit)	MIRA	PROCESS	Deviation (%)	Type
Total fusion power P_{fus} (MW)	2000.0	1998.0	+0.1	DT ≈ 2000
Neutron fusion power P_{neut} (MW)	1598.2	1597.0	+0.1	O
Alpha fusion power P_{α} (MW)	400.1	399.1	+0.3	O
Additional heating power P_{add} (MW)	49.9	50.0	+0.2	DT ≈ 50
Fusion gain Q (—)	39.8	39.3	+1.2	O
Normalized CD efficiency γ_{CD} (10^{20} A (W m^2)$^{-1}$)	0.3	0.3	+0.0	I
Ohmic heating power P_{OH} (MW)	0.2	0.8	−71.8	O
Power across separatrix P_{sep} (MW)	124.7	156.4	−20.3	O
Total radiation power P_{rad} (MW)	325.6	275.2	+18.3	O
Synchrotron radiation power P_{syn} (MW)	29.3	16.6	+76.3	O
Bremsstrahlung radiation power P_{brem} (MW)	51.8	72.0	−28.1	O
Line radiation power P_{line} (MW)	244.5	186.5	+31.1	O
Divertor challenging criterion $P_{\mathrm{sep}}B_{\mathrm{t}}/(q_{95}AR_0)$ (MW T m^{-1})	7.4	9.2	−19.3	OL ⩽ 9.2
Divertor challenging criterion P_{sep}/R_0 (MW m^{-1})	14.0	17.5	−20.3	OL ⩽ 17.5
Divertor heat flux q_{div} (MW m^{-2})	10.0	n.a.	n.a.	OL ⩽ 10
LH transition power P_{LH} (MW)	103.9	107.5	−3.3	O
Energy confinement time τ_{E} (s)	2.5	3.9	−34.6	O
H factor H (—)	0.9	1.1	−18.0	O
LH transition factor f_{LH} (—)	1.2	1.5	−17.5	OL⩾ 1.2
Helium particle-to-energy confinement time f_{P2E} (—)	5.0	7.1	−29.6	I

Table 5. Calculated plasma current and flux balance parameters of the EU-DEMO 2017 baseline: comparison between MIRA and PROCESS.

Parameter variable (unit)	MIRA	PROCESS	Deviation (%)	Type
Plasma resistance R_{p} (Ohm)	1.83×10^{-9}	4.41×10^{-9}	−58.4	O
Plasma self-inductance L_{p} (H)	1.77×10^{-5}	1.55×10^{-5}	+14.4	O
Plasma loop voltage U_{loop} (mV)	20.4	42.2	−51.7	O
Bootstrap current fraction f_{BS} (—)	0.31	0.39	−19.4	O
CD current fraction f_{CD} (—)	0.11	0.11	+0.6	O
Inductive current fraction f_{ind} (—)	0.58	0.50	+14.8	O
Ejima coefficient c_{Ejima} (—)	0.3	0.3	+0.0	I
Resistive flux consumption at RU Ψ_{res} (Wb)	65.12	64.28	+1.31	O
Inductive flux consumption at RU Ψ_{ind} (Wb)	95.3	117.4	−18.8	O
Poloidal flux at plasma BD on axis Ψ_{BD} (Wb)	307.2	347.6	−11.6	O
Poloidal flux swing at flat-top—SOF $\Delta\Psi_{\mathrm{b}}$ (Wb)	297.5	304.3	−2.3	O
Maximum plasma burn time $\tau_{\mathrm{burn}}^{\mathrm{max}}$ (h)	4.02	2.21	+81.9	DT ⩾ 2

where $\mathcal{M}_{i,j}$ denote the (i, j) element of the mutual inductance matrix $\hat{\boldsymbol{\mathcal{M}}}$ between all magnetically-coupled TF coils i and j. Note that for $j = i$, $\mathcal{M}_{i,i} = L_i$, with L_i being the self-inductance of the coil i.

The stored energy is a key input to the design of the superconducting cable for quench protection criteria. Also, from a 3D spatial resolution of the magnetic quantities, precise estimations of field, force and energy are obtained for the plasma, PF/CS and TF coil system, which is a considerable upgrade for fusion systems analysis tools. Further modelling aspects related to spatial arrangement and the sizing of superconducting cables, coils casing and electrical insulators of TF and PF coils are normally part of the engineering features tackled in SCs (e.g. [4, 74]). These have been cornered in the MIRA frame, too, with a detailed description on this subject outlined in [13]. However, these modelling insights have no impact on the results here presented, as the focus is primarily devoted to plasma physics, reactor neutronics and plant integral modelling. Therefore, they are not reported in the paper.

3.7. Plant integral power balance

MIRA includes a steady-state plant power balance model to compute the key power flows, the fusion power generated in the plasma domain to the net electric power. The total thermal power $\dot{Q}_{\mathrm{th}}$ employed for conversion into electricity is defined as:

$$\dot{Q}_{\mathrm{th}} = \dot{Q}_{\mathrm{BB}} + \dot{Q}_{\mathrm{DIV}} + \dot{Q}_{\mathrm{VV}}, \tag{40}$$

where $\dot{Q}_{\mathrm{BB}}$, $\dot{Q}_{\mathrm{DIV}}$ and $\dot{Q}_{\mathrm{VV}}$ indicate the total thermal power deposited in BB, divertor and VV. $\dot{Q}_{\mathrm{BB}}$ results from the surface heating of plasma radiation P_{FW}^{γ} (equation (30)) and nuclear heating power $R_{\mathrm{heat}}^{\mathrm{BB}}$ (equation (33)), both calculated in the

neutronic module. Hence,

$$\dot{Q}_{\mathrm{BB}} = P^{\gamma}_{\mathrm{FW}} + R^{\mathrm{BB}}_{\mathrm{heat}}. \tag{41}$$

The total radiation power P_{rad} from the steady-state plasma power balance (equation (16)), splits into a FW and a divertor share, both evaluated in the 2D neutronic model, such that $P_{\mathrm{rad}} = P^{\gamma}_{\mathrm{FW}} + P^{\gamma}_{\mathrm{DIV}}$. The divertor needs to recover the power across the separatrix P_{sep} (from charged particles), the nuclear heating power from neutron radiation $R^{\mathrm{DIV}}_{\mathrm{heat}}$ and the power from plasma radiation $P^{\gamma}_{\mathrm{DIV}}$. Thus,

$$\dot{Q}_{\mathrm{div}} = P^{\gamma}_{\mathrm{DIV}} + P_{\mathrm{sep}} + R^{\mathrm{DIV}}_{\mathrm{heat}}. \tag{42}$$

Due to the one-dimensional approximation in the reactor physical components, the neutronics module does not compute the nuclear heating deposition in the divertor. Therefore, an input energy multiplication factor $\mathrm{EMF}_{\mathrm{DIV}}$, derived from detailed 3D DEMO MC transport analyses, is adopted to calculate $R^{\mathrm{DIV}}_{\mathrm{heat}}$, from the total neutron power load from the plasma core P^{n}_{DIV}, outlined in. equation (30). Accordingly, $R^{\mathrm{DIV}}_{\mathrm{heat}} = \mathrm{EMF}_{\mathrm{DIV}} \cdot P^{n}_{\mathrm{DIV}}$. Finally, $\dot{Q}_{\mathrm{VV}}$ accounts only for nuclear heating power deposition, i.e., $\dot{Q}_{\mathrm{VV}} \equiv R^{\mathrm{VV}}_{\mathrm{heat}}$.

The gross electric power reads as

$$\dot{W}_{\mathrm{gross}} = \eta_{\mathrm{gross}} \cdot \dot{Q}_{\mathrm{th}}, \tag{43}$$

where η_{gross} relates to the gross electric efficiency, being a prescribed input to the model inherited from existing DEMO plant layouts [75, 76], including primary heat transport system (PHTS), energy storage system and power conversion system (PCS). Finally, the net electric power $\dot{W}_{\mathrm{net}}$ is the remainder of $\dot{W}_{\mathrm{gross}}$ reduced by the total electric recirculating power $\dot{W}_{\mathrm{rec}}$, given by the sum of the following major electric consumptions. Thus

$$\dot{W}_{\mathrm{net}} = \dot{W}_{\mathrm{gross}} - \dot{W}_{\mathrm{rec}}, \tag{44}$$

where

$$\dot{W}_{\mathrm{rec}} = \dot{W}_{\mathrm{pump}} + \dot{W}_{\mathrm{add}} + \dot{W}_{\mathrm{cryo}} + \dot{W}_{\mathrm{aux}}. \tag{45}$$

As a first approximation, these are linked to the total thermal power $\dot{Q}_{\mathrm{th}}$ as follows:

- $\dot{W}_{\mathrm{pump}} \propto \dot{Q}^{3}_{\mathrm{th}}$ is the coolant pumping power to carry the high-pressure coolants through BB, divertor and VV structures (∼110 MW in helium-cooled PHTS and ∼30 MW in water-cooled PHTS [77]).
- $\dot{W}_{\mathrm{add}} = \eta_{\mathrm{add}} \cdot P_{\mathrm{add}}$ as the additional heating power supplied to the additional heating systems, with $\eta_{\mathrm{add}} \sim 0.4$ being the wall-plug efficiency [18].
- $\dot{W}_{\mathrm{cryo}} = f_{\mathrm{cryo}} \cdot \dot{Q}_{\mathrm{th}}$, is the total cryogenic power (coils, vacuum, etc), estimated approximately 20–30 MW for a 2000 MW thermal power [18], where f_{cryo} is a user-defined input, typically around 0.8–1.3%.
- $\dot{W}_{\mathrm{aux}}$ is the electric power for additional electricity demands for other auxiliary plant systems, such as magnets power supply, tritium handling, diagnostics and any consumptions to operate buildings or other plant facilities. Currently, only speculative assumptions can be done on this specific term. In MIRA, a fraction f_{aux} is taken as a user-defined parameter to scale linearly $\dot{W}_{\mathrm{aux}}$ to $\dot{Q}_{\mathrm{th}}$ such that $\dot{W}_{\mathrm{aux}} = f_{\mathrm{aux}} \cdot \dot{Q}_{\mathrm{th}}$. Here, f_{aux} is set to 3.7%, as adopted in the PROCESS DEMO 2015 baseline [18].

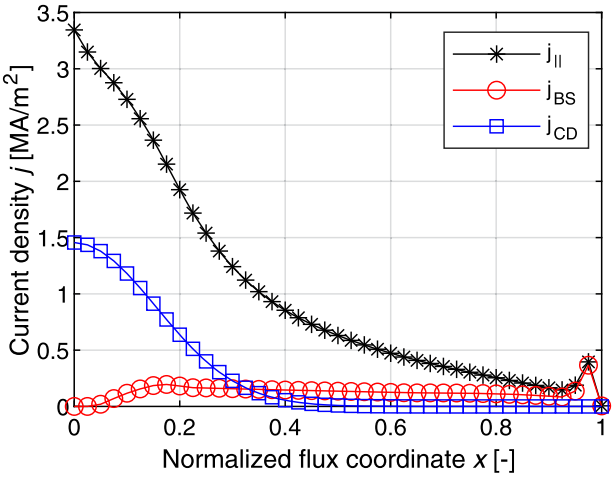

Figure 11. Plasma parallel current density profiles of the EU-DEMO 2017 baseline, as per MIRA/PLASMOD transport simulation.

A minimum net electric power of around 300–500 MW is set as a top-level requirement for the EU-DEMO plant [1]. The model is rather simplified in terms of mathematical sophistication (0D, steady-state integral energy balance). However, the terms in the balance equations related to the thermal powers are based on a consolidated modelling frame, where the radiation power distribution between BB and divertor and the nuclear heating in the reactor components are calculated from 2D/1D neutron/gamma transport solutions.

4. MIRA analysis of the EU-DEMO 2017 baseline

Currently, MIRA is primarily suited to analyse fusion reactor baselines that are generated by fast SC such as PROCESS and SYCOMORE. The major target is to inherit such reactor baselines and verify the fulfilment of the top-level requirements, plasma operational limits and technological constraints, as shown in figure 1. Possibly, design optimization around a DEMO baseline can be performed by parametrizing certain reactor parameters. The MIRA approach has been first applied to the EU-DEMO 2015 originating from the PROCESS SC [13]. The study showed that by relying on more sophisticated physics and engineering models, some of the key requirements and operational limits were not satisfied, such as plasma burn time and TF ripple. Also, nontrivial dependencies between flux swing for pulsed operation, reactor neutronics, and magnets engineering figures were highlighted. The goal of this section is to repeat a similar study on the most up-to-date EU-DEMO 2017 baseline [2, 78], generated by the PROCESS SC and referred hereafter to as 'baseline'.

4.1. Input configuration of the EU-DEMO 2017 baseline

The MIRA baseline analysis has been carried out by inheriting from the DEMO baseline the same plasma sizes, fusion power and additional heating power, and relying on the same

Table 6. Plasma BD and flat-top configurations of the EU-DEMO 2017 baseline. The parameters are reported for the plasma BD, SOF and EOF.

Parameter variable (unit)	BD	SOF	EOF	Type
Poloidal flux at plasma BD Ψ_{BD} (Wb)	307.15	n.a.	n.a.	O
Peak stray field in the BD region B_{stray}^{max} (mT)	2.99	n.a.	n.a.	OL $\leqslant 3$
Plasma BD point/r-coordinate r_{BD} ($\mathbf{X_{BD}}$) (m)	8.938	n.a.	n.a.	DT ≈ 8.938
Plasma BD point/z-coordinate z_{BD} ($\mathbf{X_{BD}}$) (m)	0.0	n.a.	n.a.	DT ≈ 0.0
Poloidal flux at plasma magnetic axis Ψ_{ax} (Wb)	n.a.	306.2	8.6	O
Poloidal flux at plasma boundary Ψ_b (Wb)	n.a.	+146.6	−150.9	O
Plasma magnetic axis/r-coordinate r_{ax} (**A**) (m)	n.a.	9.339	9.343	O
Plasma magnetic axis/z-coordinate z_{ax} (**A**) (m)	n.a.	0.230	0.238	O
Poloidal flux at plasma boundary Ψ_b (Wb)	n.a.	+146.55	−150.95	O
Plasma lower X-point/r-coordinate r_{X_l} ($\mathbf{X_l}$) (m)	n.a.	7.49	7.49	DT ≈ 7.49
Plasma lower X-point/z-coordinate z_{X_l} ($\mathbf{X_l}$) (m)	n.a.	−5.32	−5.32	DT ≈ -5.32
Plasma upper (inactive) X-point/r-coordinate r_{X_u} ($\mathbf{X_u}$) (m)	n.a.	7.02	7.02	O
Plasma upper (inactive) X-point/z-coordinate z_{X_u} ($\mathbf{X_u}$) (m)	n.a.	6.12	6.12	O
Plasma major radius R_0 (m)	n.a.	8.931	8.928	DT ≈ 8.938
Plasma minor radius a (m)	n.a.	2.889	2.894	DT ≈ 2.883
Plasma volume V_p (m^3)	n.a.	2375.8	2394.6	DT ≈ 2383
Plasma triangularity δ_{95} (—)	n.a.	0.332	0.328	DT ≈ 0.333
Plasma elongation κ_{95} (—)	n.a.	1.652	1.659	DT ≈ 1.652
Peak current density in CS coils $J_{c,CS}$ (MA m^{-2})	12.49	+8.59	−12.49	$\lvert TL\rvert \leqslant 12.5$
Peak current density in PF coils $J_{c,PFC}$ (MA m^{-2})	9.50	+10.60	−9.12	$\lvert TL\rvert \leqslant 12.5$
Peak field in CS coils $B_{peak,CS}$ (T)	12.46	6.09	11.03	TL $\leqslant 13.7$
Peak field in PF coils $B_{peak,PFC}$ (T)	5.69	5.60	3.56	TL $\leqslant 5.7$
Peak field in TF coils $B_{peak,TFC}$ (T)	11.65	11.75	11.71	TL $\leqslant 12.23$
Peak vertical force in PF coils $F_{z,peak}^{PF}$ (MN)	−430.8	−103.1	−233.3	$\lvert OL\rvert \leqslant 450$
Total vertical force in CS stack F_z^{CS} (MN)	+102.1	+4.94	+181.5	$\lvert OL\rvert \leqslant 300$
Peak separation force in CS stack $F_{z,peak}^{CS,sep}$ (MN)	+102.02	+126.5	+181.5	$\lvert OL\rvert \leqslant 350$
Upper out-of-plane force on TF coil $F_{y,TFC}^{up}$	+0.5	+28.8	+15.3	O
Lower out-of-plane force on TF coil $F_{y,TFC}^{down}$	−9.1	−81.4	−46.6	O
Average TF coil bending force $F_{b,TFC}$ (MN)	4.8	55.2	30.9	O

technological and plant integration features. These assumptions allow for a consistent comparison by systems, including the plasma and all the physical reactor components and plant systems addressed in this study. In summary, the main design requirements and key design features are listed in table 1.

The 2D reactor build generated in the geometry module is displayed in figure 8. This reactor sketch has been obtained from a set of geometry primitives implemented ad-hoc to reproduce the 2D radial/poloidal cross-section of the 3D DEMO CAD model [87]. In such a way, the 2D geometries used by the FBE, neutronics and TF engineering modules are adherent to the realistic DEMO reactor configurations. The poloidal field coils system is composed of six PF coils and five CS elements. The CS stack, in turn, consists of two upper elements, two lower elements and one central element. The full list of radial/vertical size and location of all the eleven PF/CS coils is reported in [22]. Notice that these represent only the initial guess used by the geometry module, as minor shifts are applied based on the TF coil shape and VV ports space allocation.

The space reservation of the BB system results from a multi-layer composition of different BB subsystems, each characterized by a given radial and vertical thickness and material composition inherited from the specific HCPB [82] and WCLL designs [84]. For both blanket concepts, these subsystems are 2 mm tungsten armour layer, 25 mm FW, the BZ, and the manifold region. Both BB systems share the same space allocation, whose overall radial inboard and outboard thicknesses are 80 and 100 cm, respectively.

In the HCPB blanket, the breeding material (∼20% vol in the BZ region) is composed of a ceramic breeder mixture of Li_4SiO_4 + 35 mol% Li_2TiO_3 (with 60% ^{6}Li enrichment) embedded in prismatic blocks of $Be_{12}Ti$ acting as neutron multiplier (∼55% vol). The low-activation Eurofer steel is used as structural material and its volumetric composition in the BZ is approximately 15% vol. The remainder (∼10% vol) is attributed to high-pressure helium as cooling fluid (80 bar, 300 °C–500 °C inlet/outlet temperatures). The BZ in the DEMO 2017 WCLL deploys a liquid metal lead-lithium eutectic alloy (labelled PbLi) with a 90% ^{6}Li enrichment as breeding and neutron multiplying material (∼80% vol), Eurofer as structural material (∼15% vol) and approximately 5% volume of high-pressure cooling water (155 bar, 285 °C–325 °C inlet/outlet temperature). This set of specifications is relevant to the characterization of the neutron cross-section data and radial build needed to execute the neutronic module (section 3.5).

The parameters associated with the divertor geometry are initially set to match the 3D DEMO CAD configuration

and adjusted by the geometry module based on the separatrix profile from the FBE solution. The VV is a double-shell stainless structure cooled in the inter-space by low-pressure water, whose overall inboard and outboard widths are 60 and 80 cm, respectively, and a with a global steel/water material composition of 60/40% vol [87]. The TF coil is based on a radial/vertical space reservation replicating the 2D envelope from the 3D CAD model and incorporates a rectangular current-carrying WP embedded in a stainless-steel casing structure. The WP extends by 124 cm toroidally and 82 cm radially [86], and the TF coil's overall inboard and outboard thicknesses are 98 cm each [78]. A 2.4 m-wide gap separates the outer TF coil leg from the VV in the outboard region.

4.2. Output configuration of the EU-DEMO 2017 baseline

In this section, the results associated with the physics and engineering parameters introduced in section 3 are reported and analysed in terms of deviation from the PROCESS baseline, outlining the major modelling differences between the two approaches. Normally, a table is reported for each subsection and a column is devoted to the relative deviation between MIRA and the baseline from PROCESS. When a direct comparison is not applicable, a mark 'n.a.' is reported, instead. Also, the column 'type' indicates whether a parameter is an input (I), design target (DT), operational limit (OL), technological limit (TL) or output (O). In the case of DT, OL or TL, the value associated with its upper/lower limit or equality constraint is reported therein.

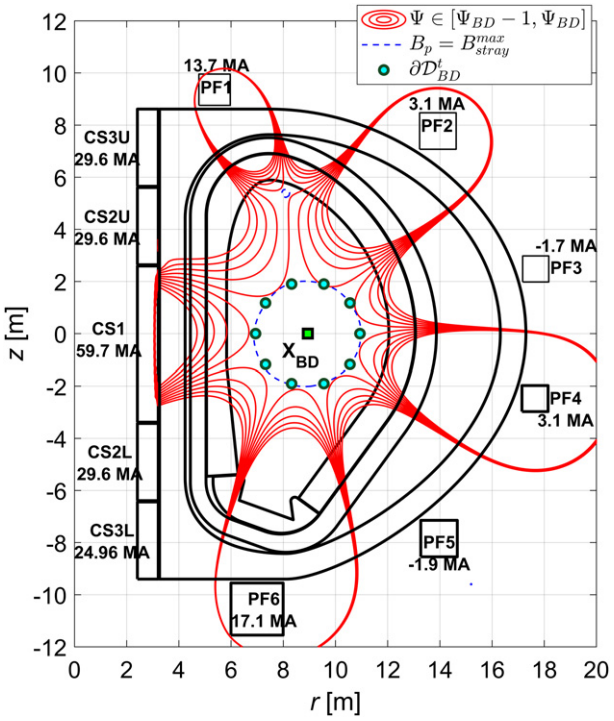

Figure 12. Calculated spatial magnetic configurations of the EU-DEMO 2017 baseline at plasma BD. The solid lines indicate iso-flux contours within the flux interval defined by $[\Psi_{BD}-1$ Wb, $\Psi_{BD}]$. The dashed line relates to the iso-field line at B^{max}_{stray} and the circle markers indicate the target max stray field area, such that $B_p \leqslant B^{max}_{stray}$.

4.2.1. MIRA core/SOL physics configuration of the EU-DEMO 2017 baseline. The core/SOL physics configuration has been obtained by observing the plasma operational limits elucidated in section 3.3, and imposing design targets on fusion and additional heating power listed in table 1. In summary, the plasma operational limits selected for the EU-DEMO 2017 baseline include: $q_{95} \geqslant 3$ to prevent kink and sawtooth MHD instabilities, $f_{GW,ped} \leqslant 0.85$ to prevent thermal instabilities, $f_{LH} \geqslant 1.2$ to control the power exhaust necessary to operate in H-mode regime, $P_{sep}B_t/(q_{95}AR_0) \leqslant 9.2$ MW T m^{-1} to limit the power exhaust for divertor protection purposes, and $\beta_n \leqslant 4 \cdot l_i$ to prevent pressure-driven MHD instability modes. The primary goal of this subsection is not benchmarking MIRA against PROCESS, but rather highlighting the impact of the modelling assumptions in the tokamak physics area when performing reactor systems analysis. Indeed, the 1D MHD transport solver PLASMOD has been successfully integrated into PROCESS [35]. Nevertheless, the EU-DEMO 2017 baseline has been generated still relying on the 'old' 0D plasma physics approach, which makes this comparative study in line with the goals of this study.

The plasma geometry and equilibrium properties are listed in table 2. All the imposed design targets and operational limits are fulfilled for this configuration, with large accuracy for plasma elongation and triangularity. The largest deviations are found for l_i and the average poloidal field $\overline{B}_p$, where the two-dimensional effects from the equilibrium resolution play a decisive role. Note that a reliable estimation of l_i is essential to the calculation of the inductive flux consumption at plasma ramp-up (equation (26)), hence, for the maximum flat-top length τ^{max}_{flat} (equation (27)).

The safety factor q_{95} has been identified in MIRA as the maximum value matching the target fusion power ($P_{fus} \approx 2000$ MW) and allowing for a maximum additional heating power ($P_{add} \leqslant 50$ MW). In the baseline, q_{95} has been used as an iteration variable in the ITER plasma current scaling formula [88]. In MIRA, instead, q_{95} is also set as an iteration value but its value is matched from the 2D equilibrium and 1D transport solutions (equations (1) and (12)). Furthermore, the gap on q_{95} is also influenced by the relative difference found for B_t. In PROCESS, B_t is an iteration variable entering both in plasma physics and coils engineering constraining conditions, such as peak field and stress limit. In MIRA, only the peak field at the inboard TF conductor (including the ripple effects and the smaller field contribution from the PF coils) is used to compute B_t (equation (5)), explaining also the larger margin on the TF coil peak field in the baseline (see table 9). A similar deviation of q_{95} and B_t justify the very small offset found for I_p, such that they balance off one another. The profile of $q(x)$ is displayed in figure 9. The noticeable flattening in the plasma core is driven by the continuous sawtooth model implemented in PLASMOD which prevents it from falling below one.

The properties related to the plasma profiles and impurity are listed in table 3, while the electrons and ions densities, temperatures and total plasma pressure profiles are displayed

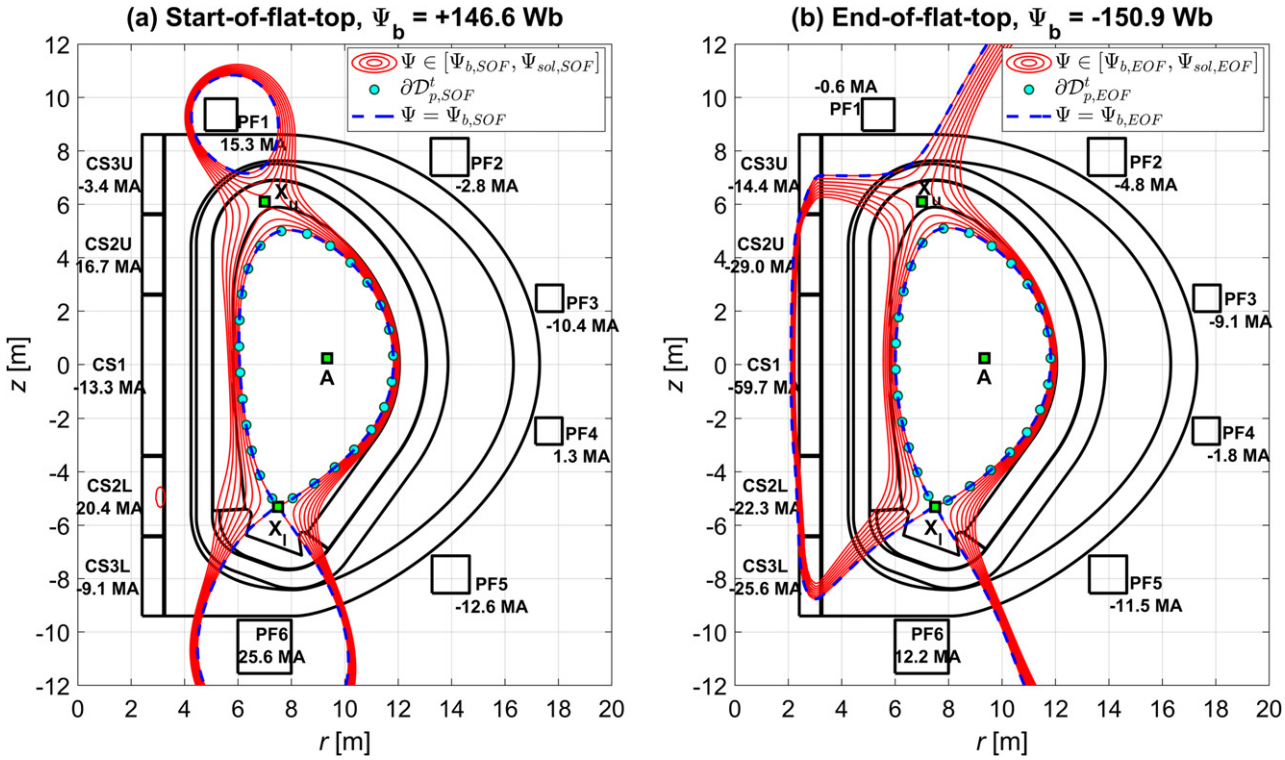

Figure 13. Calculated spatial magnetic configurations of the EU-DEMO 2017 baseline at start-of-flat-top (*a*) and end-of-flat-top (*b*). Both plots include the iso-flux contours of the SOL region, i.e. defined within the interval $[\Psi_b, \Psi_{sol}]$ with $\Psi_{sol} = \Psi(r = R_0 + a, z = 0)$, i.e. on the FW outboard mid-equatorial plane.

in figure 10. The average density and temperature present a deviation from the baseline below 4%, mostly because of the constraining condition posed on the fusion power. The baseline considers electrons and ions with the same temperature, whereas a two-fluid transport model is adopted in the 1D PLASMOD transport solver. Therefore, apart from one-dimensional effects arising from the transport problem itself (e.g., radial and highly nonlinear dependencies affecting the transport coefficients), a two-fluid approach accounting for the electron–ion equipartition power (equation (13)) presents an additional sophistication in the modelling framework which lead to the reported deviations.

Considerable deviations (∼30%–50%) have been obtained for the plasma dilution and impurity parameters, in particular for the xenon and helium concentrations. The xenon concentration at the pedestal is adjusted by PLASMOD to control the power exhausted limits posed on P_{sep} both from H-mode operation and divertor protection purposes (see calculated plasma power properties of table 4).

In this case, the f_{LH} limit drives the final value of c_{Xe}, with f_{LH} equating its lower bound, unlike $P_{sep}B_t/q_{95}AR_0$, rather below its upper limit. The computed helium concentration deviates because of the different values assumed for f_{P2E} (input in MIRA, iteration variable with a lower limit of five in PROCESS) and because of the different τ_E emerging from the 1D transport resolution. The argon concentration is not given in the baseline because the divertor challenging criterion is uniquely observed to limit the power load to the divertor targets [3]. In MIRA (through PLASMOD), the implemented SOL physics module has also retro-feedback to the plasma dilution in the plasma core, affecting its overall mass and charge configuration.

While a good agreement is found for P_{fus} and P_{add} (because of their equality constraints), P_{sep} is nearly 20% above and P_{rad} is 18% below the baseline. A combination of effects explains such deviations, primarily including:

- density and temperature profiles (calculated from 1D transport in PLASMOD, while in the baseline it is obtained from a profile parametrization and 0D power balance)
- confinement time τ_E (deduced from the transport solution instead of the ITER IPB98(y, 2) scaling law),
- P_{line}, where a combination of deviations found in the plasma impurity, in the profiles and (possibly) in the different set of radiation power loss functions used to calculate L_Z jointly lead to a 31% overestimation.

The H-factor is found nearly 20% below the baseline. However, the substantial difference is that while in MIRA (through PLASMOD) H is calculated, in the PROCESS baseline it is an input and it is used as a global iteration variable.

The plasma current and poloidal flux properties are listed in table 5. The major deviations are observed for the plasma resistance R_p (∼60% smaller) and bootstrap current fraction (∼20% smaller), mostly because of the gaps observed in the profile figures and plasma dilution (Z_{eff}). Also, f_{BS} is calculated from actual 1D profiles, whereas in a 0D SC fashion is usually computed via scaling formulas (e.g., Sauter's [46] or Wilson's [88] scaling law).

Table 7. Calculated core neutron/photon radiation parameters of the EU-DEMO 2017 baseline: comparison between MIRA and PROCESS.

Parameter variable (unit)	MIRA HCPB/WCLL	PROCESS HCPB	Deviation (%)	Type
Neutron radiation power to FW P^{n}_{FW} (MW)	1519	1413	+7.5	O
Neutron radiation power to divertor P^{n}_{div} (MW)	77	183	−57.9	O
Average neutron heat flux to FW $\Gamma^{n}_{\mathrm{FW,av}}$ (MW m^{-2})	1.03	1.01	+2.2	O
Average neutron heat flux to divertor $\Gamma^{n}_{\mathrm{div,av}}$ (MW m^{-2})	0.38	1.02	−62.7	O
Peak neutron heat flux to FW $\Gamma^{n}_{\mathrm{FW,peak}}$ (MW m^{-2})	1.48	n.a.	n.a.	O
Peak neutron heat flux to divertor $\Gamma^{n}_{\mathrm{div,peak}}$ (MW m^{-2})	0.70	n.a.	n.a.	O
Photon radiation power to FW P^{γ}_{FW} (MW)	304	243	+25.1	O
Photon radiation power to divertor $P^{\gamma}_{\mathrm{div}}$ (MW)	21.2	32	−33.8	O
Average photon heat flux to FW $\Gamma^{\gamma}_{\mathrm{FW,av}}$ (MW m^{-2})	0.21	0.17	+23.5	O
Average photon heat flux to divertor $\Gamma^{\gamma}_{\mathrm{div,av}}$ (MW m^{-2})	0.10	0.17	−41.2	O
Peak photon heat flux to FW $\Gamma^{\gamma}_{\mathrm{FW,peak}}$ (MW m^{-2})	0.24	0.59	−59.3	OL $\leqslant 1$
Peak photon heat flux to divertor $\Gamma^{\gamma}_{\mathrm{div,peak}}$ (MW m^{-2})	0.20	n.a.	n.a.	O

All these combined effects lead to a nearly twice smaller V_{loop}, and, considering also the deviation observed for l_{i} and Ψ_{BD} (acting on the inductive flux consumption in $\Psi_{\mathrm{b,SOF}}$ of equation (26)), this ultimately leads to a maximum burn time $\tau^{\mathrm{max}}_{\mathrm{burn}}$ that is almost twice as large as the baseline. This result confirms again the impact of the physics and engineering modelling assumptions on the systems design and the fulfilment of the major design requirements and engineering constraints. Furthermore, it shows the importance of having at disposal inter-disciplinary systems/design tools that are based on 1D and 2D physics and engineering modelling sophistication. A deviation of nearly 11% observed for Ψ_{BD} is purely attributed to two-dimensional interconnections between CS/PF coils and maximum stray field constraints, depicted by two-dimensional field shaping and control limits accounted in coil current solver.

The current density profiles are displayed in figure 11. Note the peak of j_{BS} at pedestal height, confirming the benefits of depicting the radial phenomena in the core transport physics modelling.

4.2.2. MIRA engineering configuration of the EU-DEMO 2017 baseline. This subsection outlines the calculated engineering parameters associated with the plasma scenario analysis, reactor neutronics, toroidal field configuration, and plant power balance (sections 3.4–3.7).

The plasma scenario properties are listed in table 6. The plasma shaping requirements and coils technological limits are fully met for the identified pulse time frames. In particular, the plasma major and minor radii are constrained within one-centimetre tolerance at the flat-top, and V_{p}, $\kappa_{95}$and δ_{95} deviate from their design targets with less than 2% tolerance from the target values. Also, all the radial and vertical coordinates of the BD and flat-top magnetic nulls $\mathbf{X_{BD}}$ and $\mathbf{X_{I}}$ match the constrained values. Note also the positions of the magnetic axis $\mathbf{A}$ and the inactive magnetic null $\mathbf{X_u}$ which remain steady between the SOF and EOF. This results from constraining at the EOF $B_r(\mathbf{X_u}) = B_z(\mathbf{X_u}) = 0$, with $r_{X_{\mathrm{u}}}$ and $z_{X_{\mathrm{u}}}$ calculated at the SOF such that $\mathbf{X_u}$ lays outside the BB region, in the attempt of reducing large heat fluxes in the upper part of the FW [65]. These two conditions are posed as additional linear constraints in the EOF configuration for the coil current solution of equation (7).

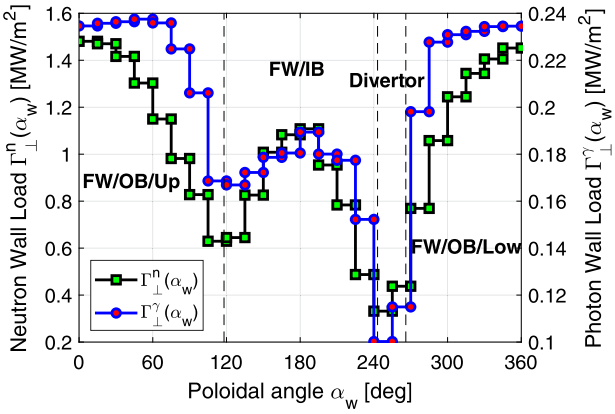

Figure 14. Calculated poloidal distribution of neutron and photon radiation wall load $\Gamma^{n/\gamma}_{\perp}(\alpha_{\mathrm{w}})$ of the EU-DEMO 2017 baseline.

Only the peak current density, magnetic fields and vertical forces are reported in table 6, while the full list of coil current, field and vertical forces is reported in appendix B (see table 11). The technological limits of the CS and the PF coils influence the outcome of the coils current for the BD and the EOF plasma configuration. At plasma BD, the maximum current density is engaged in all CS elements but CS3L and the maximum magnetic field is reached in PFC1. At plasma EOF, the current density in the CS elements poses the limiting conditions to the poloidal flux swing for maximizing τ_{flat}. The lower current limit is indeed carried by CS1 and CS2U and CS3L are also close to reaching the saturation values.

The magnetic configurations at the plasma BD, SOF and EOF are visualized in figures 12 and 13. The coils currents and names are also displayed on top of each coil. Each plot includes a set of circle markers indicating target contours, depending on the analysed time frame. In the plasma BD, the target BD region $\partial\mathcal{D}^{\mathrm{t}}_{\mathrm{BD}}$ is overlapped to the $B_{\mathrm{p}} = B^{\mathrm{max}}_{\mathrm{stray}}$ iso-field line, showing that the latter envelopes the former. A similar approach is chosen to have a graphical comparison of the target plasma separatrix $\partial\mathcal{D}^{\mathrm{t}}_{\mathrm{p}}$ (needed to meet the shaping requirements on κ_{95}, δ_{95}, R_0, a and V_{p}) and the iso-flux contour of $\Psi = \Psi_{\mathrm{b}}$.

Table 8. Calculated core reactor neutronics parameters of the EU-DEMO 2017 baseline (HCPB and WCLL blanket designs): comparison between MIRA and PROCESS.

Parameter variable (unit)	MIRA HCPB/WCLL	PROCESS HCPB	Deviation (%)	Type
Tritium breeding ratio TBR (—)	1.22/1.17	n.a.	n.a.	DT $\geqslant$ 1.15
Peak fast neut. flux, TFC $\Phi^{\mathrm{TFC}}_{\mathrm{fast,peak}}$ (cm^{-2} s^{-1})	6.2×10^{8}/7.8×10^{7}	2.2×10^{8}	181.8	TL $\leqslant 10^{9}$
Peak nuclear heating, TFC $\mathcal{R}_{\mathrm{heat,peak}}$ (W m^{-3})	38.2/4.8	20.6	85.4	TL $\leqslant$ 50
BB nuclear heating power $R^{\mathrm{BB}}_{\mathrm{heat}}$ (MW)	2037/1769	1826	11.6	O
Divertor nuclear heating power $R^{\mathrm{DIV}}_{\mathrm{heat}}$ (MW)	137.9	183	-24.6	O
VV nuclear heating power $R^{\mathrm{VV}}_{\mathrm{heat}}$ (MW)	53.1/7.2	4.1	1195.1	O

The peak magnetic fields and the toroidal bending forces have been also reported in table 6 because they are both influenced by the poloidal magnetic field; hence they are subject to variations during a plasma pulse. The smallest value is observed at BD, where the field contribution from the plasma is not present. Overall, the PF coils and plasma contribute approximately to 1% of the overall value of $B_{\mathrm{peak,TFC}}$. Note also the variations of $F_{\mathrm{b,TFC}}$ and of the upper and lower out-of-plane forces throughout the pulse frames, which, if not accounted for, might lead to stress fatigue issues.

The calculated parameters associated with the core neutron and photon wall loading figures (section 3.5.1) are listed in table 7. The 2D radiation transport model allows for a detailed poloidal mapping of the core neutron and photon plasma powers among the plasma-facing components, with a visible impact on the power repartition between divertor and FW. For a total neutron fusion power P_{neut}, the calculated neutron power to the divertor P^{n}_{div} is nearly 60% smaller than the baseline. Similar conclusions can be drawn for the photon radiation power P_{rad}, including also the differences found in core physics results (table 4). These aspects have a direct impact on the overall plant thermo-dynamic efficiency since the thermal powers transferred to the divertor and the BB ultimately have a different grade when converted into electricity [77]. It also shows again the benefits from refining the spatial sophistication of the engineering models at a systems analysis level. Similarly, the calculated average and the peak heat fluxes account for volumetric 2D profiles of $\dot{q}_{\mathrm{rad}}$ and $\dot{q}_{\mathrm{neut}}$ and for the 2D shape of the FW and divertor. In a simplified 0D approach, instead, these are obtained by fixing input peaking factors, defined as the ratio between peak and average heat fluxes. Figure 14 displays the poloidal distributions of plasma core neutron and photon wall loads on FW along the poloidal angle α_{w} oriented counter-clockwise from the outboard mid-equatorial plane. These aspects explain the differences from the baseline obtained for the average and peak neutron and photon heat fluxes.

The computed neutronic features from the core transport model (section 3.5.2) are reported in table 8 for HCPB and the WCLL BB designs. The PROCESS baseline, instead, refers only to the HCPB design.

Large deviations have been found for the local peak values associated with the shielding limits ($\Phi^{\mathrm{TFC}}_{\mathrm{fast,peak}}$ and $\mathcal{R}_{\mathrm{heat,peak}}$) and the total heat deposition in the VV ($R^{\mathrm{VV}}_{\mathrm{heat}}$). Different modelling sophistication (and most likely different input assumptions that could not be fully verified) explain such deviations.

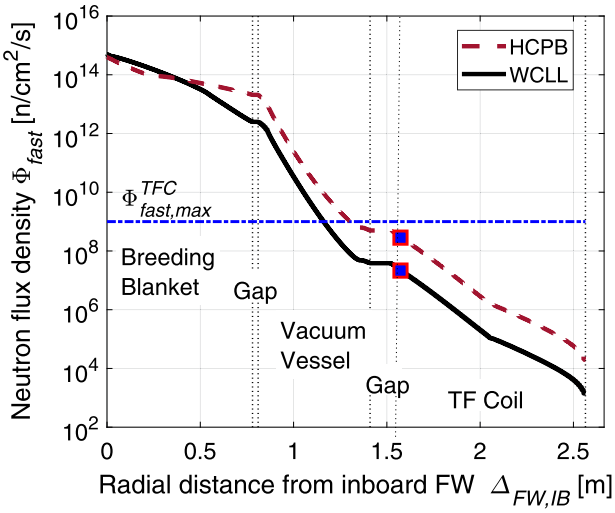

Figure 15. Neutronics configuration of the DEMO 2017 baseline (HCPB and WCLL blanket designs) as per MIRA analyses: fast neutron flux density Φ_{fast} vs radial distance from inboard FW $\Delta_{\mathrm{FW,ib}}$.

Nevertheless, the values calculated as per MIRA neutronic analysis resemble the results emerging from the detailed 3D MC simulations for EU-DEMO HCPB and WCLL designs [71, 89]. Furthermore, in terms of global impact on the overall plant performances, the power deposition to the VV represents a smaller share of the overall thermal input to the PCS.

As shown by the reported values of TBR, $\Phi^{\mathrm{TFC}}_{\mathrm{fast,peak}}$ and $\mathcal{R}_{\mathrm{heat,peak}}$, the HCPB design solution features better tritium breeding and energy multiplication performances, due to the larger neutron multiplications in the beryllium multiplying material. On the other hand, in terms of shielding the hierarchies between the two BBs are inverted, with the WCLL blanket yielding flux densities that are one order of magnitude lower. The WCLL blanket performs better shielding performances because of a larger neutron moderation capacity of water and elastic scattering of Pb compared to beryllium. Figure 15 displays the radial profile of the fast neutron flux Φ_{fast} on the inboard side from the reactor. The radial coordinate is measured from the inboard FW towards the tokamak axis. In both blankets, the prescribed design targets and limits are met. However, in the case of the HCPB, the nuclear heating and fast neutron fluence are relatively close to their technological limit.

Having at disposal a neutronic module with the possibility to arbitrarily prescribe the material composition and the

Table 9. Calculated TF coil electromagnetic parameters of the EU-DEMO 2017 baseline: comparison between MIRA and PROCESS results.

Parameter variable (unit)	MIRA	PROCESS	Deviation (%)	Type
Number of TF coils N_{TFC} (—)	16	16	0.0	I
Total TF coil current $I_{\mathrm{c,TFC}}$ (MA)	14.79	13.65	+8.4	O
Peak field in TF coils $B_{\mathrm{peak,TFC}}$ (T)	11.75	11.05	+6.3	TL $\leqslant$12.23
Peak TF ripple on separatrix $\delta_{\mathrm{TF,peak}}$ (%)	0.69	0.60	+15.0	OL $\leqslant$ 0.60
TF coil radial centering force $F_{x,\mathrm{TFC}}$ (MN)	−892.3	n.a.	n.a.	O
TF coil vertical separating force $F_{v,\mathrm{TFC}}$ (MN)	553.1	448.2	+23.5	O
Peak average TF coil bending force $F_{\mathrm{b,TFC}}$ (MN)	55.2	n.a.	n.a.	O
Total stored energy in TF coils system $E_{m,\mathrm{TFC}}$ (GJ)	121.4	125.0	−2.9	O

radial layout allows incorporating the two driver BB designs in the baseline analysis. These can be compared not only in terms of their breeding, heating and shielding responses but also in terms of their holistic behaviour. For this baseline analysis, the two blankets have been assigned with the same space reservation, but the different breeding and shielding capabilities of the HCPB and WCLL blankets could be potentially exploited to optimize other global reactor figures of merits. As previously addressed in the EU-DEMO 2015 baseline analysis [13], a reactor configuration based on a reduced inboard blanket thickness has been proposed to exploit the breeding and shielding margins and maximize the plasma burn time. In the EU-DEMO 2017 baseline analysed in this study, in light of the large margin of $\tau_{\mathrm{burn}}^{\mathrm{max}}$ (table 5), the inboard VV thickness could be increased to enhance the shielding margin for the HCPB.

The MIRA simulation results associated with the current, field, force and energy operating conditions of the TF coils system are reported in table 9.

The offset from the baseline on the TF coil current is primarily driven by the deviation obtained for B_{t} (table 2), which, in turn, explains the 6.3% overestimation in $B_{\mathrm{TFC,peak}}$. The technological is fully met, including also the effects of the TF ripple, which tend to increase the peak magnetic field in the inboard leg.

The peak TF ripple on the plasma separatrix $\delta_{\mathrm{TF,peak}}$ has been found 15% larger than the baseline and does not fulfil the imposed upper limit, set to 0.6% (0.3% if the ferromagnetic inserts in the VV are included). In particular, the peak value is identified slightly above the mid-plane on the outer region of the plasma, since, around this area, the TF coils approach the plasma, by reducing the poloidal distance from it (see red square marker of figure 16). Simultaneously, moving along the plasma separatrix, the TF coils tend to come closer among themselves, reducing the effects of the TF ripple. The alternating behaviour of the distance of the coil from the separatrix and tightness of the coils determine the poloidal distribution displayed in figure 16, showing the TF ripple amplitude for a sufficiently large number of points selected in the plasma separatrix $\partial\mathcal{D}_{\mathrm{p}}$ at plasma SOF (where the peak value has been found).

The deviation from the baseline is attributed to differences in the spatial representation of the magnetostatic model, where

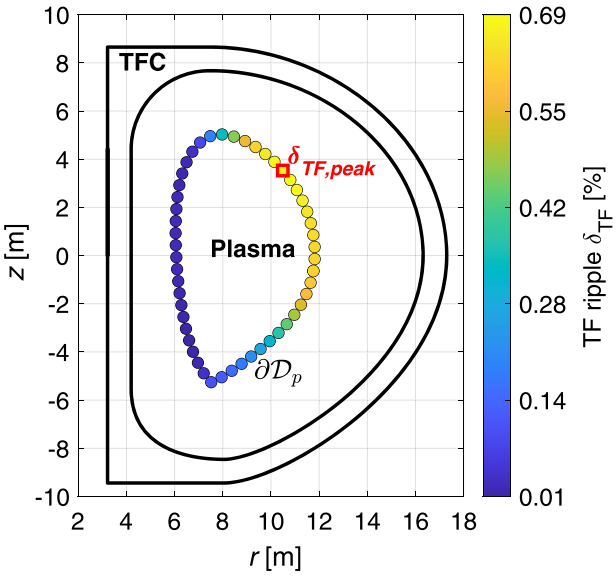

Figure 16. TF ripple poloidal distribution on the plasma separatrix calculated for the EU-DEMO 2017 baseline as per MIRA magnetostatic analysis. The red square marker denotes the poloidal location of the peak TF ripple.

both realistic elongated plasma shapes and detailed 3D magnetic field distribution are addressed in MIRA. A similar outcome of peak TF ripple has also emerged from the EU-DEMO 2015 baseline analysis [13], with practically identical values from MIRA and PROCESS. As previously demonstrated, a convenient mitigating solution to meet the 0.6% operational limit would be moving outwards the outboard TF coils. In the MIRA analysis of the EU-DEMO 2015 baseline, it was shown that a 22 cm outer expansion of the TF coil's outboard leg would guarantee achieving the tolerable value. However, the 2017 baseline operates with two TF coils less than the 2015s, hence requiring even a large widening. Overall, a design modification to either number of TF coils or shape is required to satisfy the limits. Possibly, by integrating within the same design package an ad-hoc TF coil shape optimizer, similarly to the BLUEPRINT design code [14]. Note that having at disposal a three-dimensional mapping of the TF ripple can also provide valuable insights for detailed transport codes designed to calculate the fast particle losses (for instance by diffusion) in a rippled toroidal field distribution (e.g. [90]).

Table 10. Calculated parameters related to the main plant power balance features of the EU-DEMO 2017 baseline: comparison between MIRA and PROCESS results.

Parameter variable (unit)	MIRA HCPB/WCLL	PROCESS HCPB	Deviation (%)	Type
Total thermal power $\dot{Q}_{\mathrm{th}}$ (MW)	2552/2238	2432.3	−4.9	O
Gross electric power $\dot{W}_{\mathrm{gross}}$ (MW)	963.4/783.5	987.9	−2.4	O
Gross electric efficiency η_{gross} (%)	37.7/35.0	40.6	−7.1	I
Total electric pumping power $\dot{W}_{\mathrm{pump}}$ (MW)	145.3/24.1	234.5	−37.8	O
Wall-plug efficiency η_{add} (%)	40/40	40	+0.0	I
CD auxiliary heating power $\dot{W}_{\mathrm{add}}$ (MW)	125.0/125.0	125	+0.0	O
Cryogenic electric power $\dot{W}_{\mathrm{cryo}}$ (MW)	33.2/29.1	40.4	−17.8	O
Electric power for plant auxiliary systems $\dot{W}_{\mathrm{aux}}$ (MW)	94.4/82.7	88	+7.3	O
Recirculating power $\dot{W}_{\mathrm{rec}}$ (MW)	399.9/257.9	487.9	−17.8	O
Net electric power $\dot{W}_{\mathrm{net}}$ (MW)	565.4/522.6	500	+13.0	DT $\sim$ 300–500

The computed plant power balance specifications are listed in table 10, both for HCPB and WCLL blanket configurations The requirement on the net electric power $\dot{W}_{\mathrm{net}}$ is verified for both BB concepts, with a good agreement between MIRA and PROCESS for almost all power terms, with exception of the coolant pumping power $\dot{W}_{\mathrm{pump}}$, primarily due to different input assumptions (both MIRA and PROCESS scale $\dot{W}_{\mathrm{pump}}$ from $\dot{Q}_{\mathrm{th}}$ based on reference DEMO BoP design values). Regardless of the input parameters, it is worth mentioning that a steady-state power balance approach based on simple scaling laws of $\dot{Q}_{\mathrm{th}}$ to calculate $\dot{W}_{\mathrm{cryo}}$, and $\dot{W}_{\mathrm{pump}}$, and the definition of a gross electric efficiency η_{gross} to estimate $\dot{W}_{\mathrm{gross}}$ is a rather simplified approach for crude estimations of the net electric power. However, aiming to a higher fidelity in fusion reactors' systems analysis tools, a time-dependent power flow modelling approach shall be incorporated. Ideally, the energy flows during all the plasma pulse phases shall be accounted for, as well as a more elaborate engineering view of the key plant subsystems devoted to the plant operation and electricity production (e.g., auxiliary heating, PCSs, etc).

5. Conclusions and outlook

The inter-disciplinary, multi-fidelity reactor design tool MIRA has been developed to fill the gaps between systems and detailed design codes, used for the conceptual design of DEMO and future FPPs. MIRA incorporates numerical models for the utmost physics and engineering tokamaks problems, such as 2D free-boundary magnetic equilibrium, 1D MHD plasma transport, quasi 2D neutron radiation transport and 3D magnetostatic solvers.

The MIRA approach has been applied so far by performing full systems analyses to the EU-DEMO 2015 and 2017 baselines, generated by the PROCESS SC. The analyses have illustrated that strong modelling simplifications influence the overall design of the reactor. In particular, a twice smaller loop voltage has been found when replacing a 0D core physics approach based on a fixed H-mode plasma profiles parametrization with the 1.5D MHD transport/equilibrium solver PLASMOD, successfully integrated into MIRA. Ultimately, this has a major impact on the plasma burn time (nearly twice larger than the baseline's), where a two-hour top-level requirement is set for DEMO. Also, the 0.6% TF ripple operational limit is being exceeded when deploying a three-dimensional magnetostatic Biot–Savart solver and realistic plasma shapes.

Advanced reactor analyses have highlighted non-trivial interdependencies between different reactor systems, where component-specific features have deep implications on other systems, too. The holistic and refined systems design approach implemented in MIRA has great potential to improve the conceptual design process of DEMO and FPPs. Accordingly, multiple design solutions already scanned and filtered by fast SCs like PROCESS can be further validated and being fed as inputs to systems/design codes based on a higher fidelity, such as MIRA and BLUEPRINT.

Further modelling work is required to improve the fidelity of the existing models and to implement some relevant missing ones. In particular, the following key physics and engineering areas require additional modelling efforts, as listed below:

- Optimization of TF and PF coils shape, position and number. A TF/PF coils solver that finds one or more optimal configurations with respect to plasma shaping capabilities and other coils engineering criteria (e.g. stored energy), is currently under development.
- Dynamic fuel and power cycle models. A devoted model is being developed to map, in a flexible and fully time-dependent manner, the major fuel and plasma impurities mass flows, as well as the energy distribution within the entire FPP.
- Plant availability, to calculate the plant availability factor in relation to the calculated components lifetime and the consequent remote maintenance schemes.
- Fully 2D neutronics model, to refuse the cylindrical approximation in the transport resolution and improve the accuracy of TBR and nuclear heating deposition.
- Stress analysis in TF and PF coils structures. A complete magnet module shall include as well a stress analysis tool to verify the major stress criteria on the TF coil steel casing, on the TF and PF cable steel jacketing and the turn insulation.

- A fully automated solver to find feasible plant design solutions minimizing or maximizing any given figure of merits at reactor scales.

Most of the activities listed above are already part of the ongoing EUROfusion theory, simulation, validation and verification task 14 ('multi-fidelity SC for DEMO'), launched in 2021. In this task, the reactor design codes MIRA and BLUEPRINT are currently being merged into a reference EU reactor design code, named BLUEMIRA.

Acknowledgments

We would like to thank Dr U. Fischer and Dr Y. Qiu for their worthwhile aid regarding the neutron transport modelling part; Dr G. Pattabhi Vishnuvardhan (KIT) and R. Heller (KIT) for their help and advice on magnets systems modelling; Dr M. Coleman (EUROfusion) for his advice and expertise on fusion reactors' system modelling. KIT is a member of the Helmholtz Association of German Research Centres and this work was developed under the KIT-FUSION program funding.

List of Symbols

Latin Symbols

a	Plasma minor radius
A	Plasma aspect ratio
A_p	Plasma poloidal cross-section area
A_t	Plasma toroidal surface
B_ϕ	Toroidal magnetic field
$B_{\mathrm{max},i}$	Maximum allowed magnetic field in the coil i
B_p	Poloidal magnetic field
$B_{\mathrm{peak},i}$	Peak magnetic field in coil i
B_r	Radial magnetic field
B_stray	Magnetic stray field at plasma BD
$B_\mathrm{stray}^\mathrm{max}$	Maximum allowed magnetic stray field at plasma BD
B_t	Toroidal field at plasma centre
B_z	Vertical magnetic field
c_Ejima	Ejima coefficient
c_Ar	Plasma argon concentration
c_He	Plasma helium concentration
c_Xe	Plasma xenon concentration
c_W	Plasma tungsten concentration
$\mathcal{D}_\mathrm{p}$	Plasma domain in the (r, z) poloidal region
$\mathcal{D}_\mathrm{c}$	PF/CS coils domain in the (r, z) poloidal region
$\mathcal{D}_0$	Vacuum domain in the (r, z) poloidal region
$E_{m,\mathrm{TFC}}$	Total stored energy in TF coils system
f_aux	Ratio of $\dot{W}_\mathrm{aux}$ to $\dot{Q}_\mathrm{th}$
f_BD	Bootstrap current fraction
f_CD	CD fraction
f_cryo	Ratio of $\dot{W}_\mathrm{cryo}$ to $\dot{Q}_\mathrm{th}$
f_D	Fraction of deuterium in the D/T fuel mix
$f_\mathrm{GW,ped}$	Greenwald density fraction at pedestal top
$f_\mathrm{GW,sep}$	Greenwald density fraction at separatrix
f_ind	Current inductive fraction
LH	$P_\mathrm{sep}/P_\mathrm{LH}$ ratio
f_P2E	Particle-to-energy confinement time ratio
FF'	Poloidal current gradient term in the GSE's current density formulation
F_b	Covariant component of the toroidal magnetic field B_ϕ at plasma boundary
$F_\mathrm{b,TFC}$	Bending out-of-plane force exerted on the TF coil
$F_{x,\mathrm{TFC}}$	Inward centering force exerted on the TF coil
$F_{v,\mathrm{TFC}}$	Vertical separation force exerted on the TF coil
$F_{z,i}$	Vertical force in the PF/CS coil i
$F_{z,\mathrm{max}}^\mathrm{PF}$	Maximum allowed vertical forces on single PF coils
$F_{z,\mathrm{peak}}^\mathrm{PF}$	Peak vertical force in all PF coils
F_z^CS	Total vertical force in the CS stack
$F_{z,\mathrm{max}}^\mathrm{CS}$	Maximum allowed total vertical force in the CS stack
$F_{z,\mathrm{max}}^\mathrm{CS,sep}$	Maximum allowed separation force in the CS stack
$F_{z,\mathrm{peak}}^\mathrm{CS,sep}$	Peak separation force in the CS stack
g_2	Metric coefficient of the poloidal flux configuration $g_2 = \left\langle \lvert\nabla V\rvert^2/r^2 \right\rangle$
g_3	Metric coefficient of the poloidal flux configuration $g_3 = \left\langle 1/r^2 \right\rangle$
H	Plasma H-mode factor
I_BS	Plasma bootstrap current
$I_\mathbf{c}$	PF/CS coils currents
$I_{\mathrm{c},i}$	Total current in coil i
I_CD	Plasma current drive
I_p	Plasma current
$j_\parallel$	Parallel current density
j_BS	Parallel bootstrap current density
j_CD	Parallel CD current density
$J_\mathrm{c,max}$	Maximum allowed current density in the PF/CS coils
J_ϕ	Toroidal current density
$J_{\phi,\mathrm{c}}$	Toroidal current density in the PF/CS coils region
$J_{\phi,\mathrm{p}}$	Toroidal current density in the plasma region
l_i	Plasma internal inductance
l_p	Plasma perimeter
L_p	Plasma self-inductance
n_e	Plasma electrons density profile
e,0	Plasma electrons density at axis
$n_\mathrm{e,ped}$	Plasma electrons density at pedestal top
$n_\mathrm{e,sep}$	Plasma electrons density at separatrix
n_GW	Greenwald density
n_j	Plasma density profile of the atom j ($j =$ He, D, T, Xe, Ar)
n_i	Plasma ion density profile
N_TFC	Number of TF coils (and sectors)
p	Total plasma pressure profile
p'	Pressure gradient term in the GSE's current density formulation
P_add	Additional heating power
P_α	Alpha power
P_brem	Bremsstrahlung radiation power
P_div^γ	Photon radiation power to divertor
P_div^n	Neutron radiation power to divertor
P_FW^γ	Photon radiation power to FW

P^n_{FW}	Neutron radiation power to FW
$\boldsymbol{P}_{\mathrm{fus}}$	Total fusion power
$\boldsymbol{P}_{\mathrm{line}}$	Line radiation power
$\boldsymbol{P}_{\mathrm{LH}}$	L–H threshold power
$\boldsymbol{P}_{\mathrm{neut}}$	Neutron fusion power
$\boldsymbol{P}_{\mathrm{oh}}$	Ohmic heating power
$\boldsymbol{P}_{\mathrm{rad}}$	Total radiation power
$\boldsymbol{P}_{\mathrm{sep}}$	Power transported across the separatrix
$\frac{P_{\mathrm{sep}}B_{\mathrm{t}}}{q_{95}AR_0}$	Divertor challenging criterion
$\boldsymbol{P}_{\mathrm{sync}}$	Synchrotron radiation power
$\boldsymbol{q}_{\mathrm{div}}$	Heat flux to divertor plates
$\dot{q}_{\mathrm{fus}}$	Volumetric fusion power density profile
$\dot{q}_{\mathrm{neut}}$	Volumetric neutron fusion power density profile
$\dot{q}_{\mathrm{rad}}$	Volumetric radiation power density profile
$\boldsymbol{q}$	Plasma safety factor profile
$\boldsymbol{q}_{\mathrm{b}}$	Plasma safety factor at plasma boundary
$\boldsymbol{q}_{95}$	Plasma safety factor at 95% poloidal flux surface
$\boldsymbol{Q}$	Fusion gain
$\dot{Q}_{\mathrm{BB}}$	Total thermal power in breeding blanket
$\dot{Q}_{\mathrm{div}}$	Total thermal power in divertor
$\dot{Q}_{\mathrm{th}}$	Total thermal power for electricity conversion
$\dot{Q}_{\mathrm{VV}}$	Total thermal power in the vacuum vessel
$\boldsymbol{r}$	Radial coordinate in the curvilinear coordinate system (r, ϕ, z)
$\boldsymbol{r}_{\mathrm{ax}}$	Radial coordinate of the plasma magnetic axis
$\boldsymbol{r}_{\mathrm{BD}}$	Radial coordinate of the plasma breakdown point
$r_{X_{\mathrm{l}}}$	Radial coordinate of the plasma lower X-point
$r_{X_{\mathrm{u}}}$	Radial coordinate of the inactive plasma upper X-point
$\boldsymbol{r}_{\mathrm{WP,ib}}$	Innermost radial coordinate of the TF coil's winding pack on the inboard leg
$\boldsymbol{R}_0$	Plasma major radius
R^m_{heat}	Total nuclear heating power into component m
$\mathcal{R}^{\mathrm{TFC}}_{\mathrm{heat,peak}}$	Peak volumetric heating in the TF coil's winding pack region
$\boldsymbol{R}_{\mathrm{p}}$	Plasma resistance
$\boldsymbol{T}_{\mathrm{e}}$	Plasma electrons temperature profile
$\langle T_{\mathrm{e}} \rangle$	Volume-averaged temperature of plasma electrons
$\boldsymbol{T}_{\mathrm{e,0}}$	Plasma electrons temperature at axis
$\boldsymbol{T}_{\mathrm{i}}$	Plasma ions temperature profile
$\langle T_{\mathrm{i}} \rangle$	Volume-averaged temperature of plasma ions
$\boldsymbol{T}_{\mathrm{i,0}}$	Plasma ions temperature at axis
$\boldsymbol{T}_{\mathrm{ped}}$	Plasma electrons/ions temperature at pedestal top
$\boldsymbol{T}_{\mathrm{sep}}$	Electrons/ions temperature at separatrix
$\mathrm{TBR}_{\mathrm{t}}$	Target tritium breeding ratio
$\boldsymbol{U}_{\mathrm{loop}}$	Plasma loop voltage
$\boldsymbol{V}$	Plasma volume profile
$\boldsymbol{V}'$	Plasma volume gradient profile
$\boldsymbol{V}_{\mathrm{p}}$	Plasma volume
$\dot{W}_{\mathrm{add}}$	Additional heating power supplied to the additional heating systems
$\dot{W}_{\mathrm{aux}}$	Electric power for additional electricity demands for other auxiliary plant systems
$\dot{W}_{\mathrm{cryo}}$	Electric cryogenic power consumption
$\dot{W}_{\mathrm{gross}}$	Gross electric power
$\dot{W}_{\mathrm{net}}$	Net electric power
$\dot{W}_{\mathrm{pump}}$	Electric coolant pumping power
$\dot{W}_{\mathrm{rec}}$	Total recirculation electric power
$\boldsymbol{W}_{\mathrm{th}}$	Plasma thermal energy
$\boldsymbol{x}$	Normalized poloidal flux coordinate
$\mathbf{BD}$	Breakdown point (r_{BD}: radial coordinate, z_{BD}: vertical coordinate)
$\mathbf{X_l}$	Lower plasma X-point ($r_{X_{\mathrm{l}}}$: radial coordinate, $z_{X_{\mathrm{l}}}$: vertical coordinate)
$\mathbf{X_u}$	Upper inactive plasma X-point ($r_{X_{\mathrm{u}}}$: radial coordinate, $z_{X_{\mathrm{u}}}$: vertical coordinate)
$\boldsymbol{z}$	Vertical coordinate in the curvilinear coordinate system (r, ϕ, z)
$\boldsymbol{z}_{\mathrm{ax}}$	Vertical coordinate of the plasma magnetic axis
$\boldsymbol{z}_{\mathrm{BD}}$	Vertical coordinate of the plasma breakdown point
$z_{X_{\mathrm{l}}}$	Vertical coordinate of the plasma lower X-point
$z_{X_{\mathrm{u}}}$	Vertical coordinate of the inactive plasma upper X-point
$\boldsymbol{Z}_{\mathrm{eff}}$	Plasma effective charge

Greek symbols

β_{p}	Poloidal plasma beta
β_{N}	Normalized plasma beta
β_{t}	Toroidal plasma beta
γ_{CD}	Normalized CD efficiency
$\Gamma^k_{\perp}$	Poloidal distribution of the normal heat flux of the radiation source k (with $k = n, \gamma$)
$\Gamma^k_{j,\mathrm{av}}$	Average heat flux of radiation $k = n, \gamma$ onto plasma-facing component $j = \mathrm{FW}, \mathrm{div}$
$\Gamma^k_{j,\mathrm{peak}}$	Peak heat flux of radiation $k = n, \gamma$ onto plasma-facing component $j = \mathrm{FW}, \mathrm{div}$
$\delta_{\boldsymbol{X},\mathrm{l}}$	Lower plasma triangularity at separatrix
$\delta_{\boldsymbol{X},\mathrm{u}}$	Upper plasma triangularity at separatrix
δ_{TF}	Toroidal field ripple
δ_{95}	Plasma triangularity at 95% flux surface
$\delta_{\mathrm{TF,peak}}$	Peak toroidal field ripple on plasma separatrix
$\Delta \boldsymbol{r_i}$	Radial width of the PF/CS coil i
$\Delta \boldsymbol{z_i}$	Vertical width of the PF/CS coil i
$\partial \mathcal{D}^{\mathrm{t}}_{\mathrm{BD}}$	Boundary of the target stray field area
$\partial \mathcal{D}_{\mathrm{p}}$	Calculated plasma boundary
$\partial \mathcal{D}^{\mathrm{t}}_{\mathrm{p}}$	Target plasma boundary
η_{add}	Wall-plug efficiency
η_{gross}	Gross electric efficiency
$\kappa_{\boldsymbol{X},\mathrm{l}}$	Lower plasma elongation at separatrix
$\kappa_{\boldsymbol{X},\mathrm{u}}$	Upper plasma elongation at separatrix
$_{95}$	Plasma elongation at 95% flux surface
μ_0	Vacuum magnetic permeability
ρ	Normalized toroidal flux coordinate
ρ_{BD}	Radius of breakdown area
ρ_{ped}	Normalized flux coordinate at the pedestal top
$\tau^{\mathrm{max}}_{\mathrm{burn}}$	Maximum available plasma burn time
τ_{E}	Plasma energy confinement time
τ_{p}	Particle confinement time
ϕ	Scalar flux density
$\phi^{\mathrm{TFC}}_{\mathrm{fast,peak}}$	Peak fast neutron flux in TF coil's winding pack region
Φ	Toroidal magnetic flux
Φ_{b}	Toroidal magnetic flux at plasma boundary
Φ_{fast}	Fast scalar neutron flux

ψ	Neutron flux density
Ψ	Poloidal magnetic flux
Ψ_{b}	Poloidal magnetic flux at plasma boundary
$\Psi_{\mathrm{b,EOF}}$	Poloidal magnetic flux, plasma boundary, EOF
$\Psi_{\mathrm{b,SOF}}$	Poloidal magnetic flux, plasma boundary, SOF
Ψ_{BD}	Poloidal magnetic flux at plasma breakdown
Ψ_{res}	Resistive poloidal flux consumption at plasma ramp-up
Ψ_{ind}	Inductive poloidal flux consumption at plasma ramp-up

List of Acronyms

BB	Breeding Bbanket
BD	Breakdown
BoP	Balance of plant
BTE	Boltzmann transport equation
BZ	Breeding zone
CD	Current drive
CDE	Current diffusion equation
CS	Central solenoid
DGM	Discontinuous Galerkin method
DT	Design target
EOF	End-of-flat-top
FBE	Free-boundary equilibrium
FEM	Finite element method
FPP	Fusion power plant
GSE	Grad–Shafranov equation
HCPB	Helium-cooled pebble beds
I	Input
MC	Monte Carlo
MIRA	Modular integrated reactor analysis
NBI	Neutral beam injection
PCS	Power conversion system
PF	Poloidal field
PFC	Poloidal field coil
PHTS	Primary heat transfer system
O	Output
OL	Operational limit
R & C	Requirements and constraints
RU	Ramp-up
SC	Systems code
SOF	Start-of-flat-top
TBR	Tritium breeding ratio
TF	Toroidal field
TL	Technological limit
VV	Vacuum vessel
V & V	Verification and validation
WCLL	Water-cooled lithium-lead
WP	Winding pack

Appendix A.

A.1. Resolution of the 1D flux surface-averaged Grad–Shafranov equation

The mathematical approach adopted to compute p' and FF' is derived from [25] and slightly readapted to the MIRA structure for solving the fixed-boundary equilibrium problem. The method consists of solving the 2D GSE and its 1D flux-surface-averaged iteratively. The flux-surface average of equation (1) for $J_\phi \equiv J_{\phi,\mathrm{p}}$ reads as:

$$\frac{\partial}{\partial V}\left(g_2\frac{\partial \Psi}{\partial V}\right) = -4\pi^2\mu_0\frac{\partial p}{\partial \Psi} - 4\pi^2 g_3 F\frac{\partial F}{\partial \Psi}, \tag{A.1}$$

where $V(\Psi)$ indicates the plasma volume profile, $g_2(\Psi) = \left\langle |\nabla V|^2/r^2 \right\rangle$ and $g_3(\Psi) = \left\langle 1/r^2 \right\rangle$ are metric coefficients of the poloidal flux configuration $\Psi(r,z)$, and $\langle\cdot\rangle$ indicates the flux-surface averaging operator such that for any flux-surface function f $\langle f\rangle = \frac{\partial}{\partial V}\int f\,\mathrm{d}V \equiv \oint f\frac{\mathrm{d}l}{B_{\mathrm{p}}}/\oint\frac{\mathrm{d}l}{B_{\mathrm{p}}}$, where the line integral is performed on the poloidal contour enclosing a flux surface. $B_{\mathrm{p}} = \frac{|\nabla\Psi|}{2\pi r}$ outlines the poloidal magnetic field. Both metric coefficients are calculated from the 2D profile of Ψ, obtained from the 2D resolution of the GSE.

Recalling that $q = -\partial\Phi/\partial\Psi$, the covariant F can be also expressed as $F = -2\pi H/g_3$ [25], with $H = \partial\Phi/\partial V$ and Φ being the toroidal magnetic flux. Then, assuming that p and q are known from 1D MHD transport and CDEs, and that g_2, g_3 and V are derived from a 2D poloidal flux profile $\Psi(r,z)$ (2D GSE), the 1D flux-averaged GSE can be recast into the following heterogeneous first-order ordinary differential equation in the new variable $y = \left(\frac{H}{q}\right)^2$

$$\begin{cases} \dfrac{\partial y}{\partial x}\left(\dfrac{g_2}{2} + 8\pi^4\dfrac{q^2}{g_3}\right) + y\left(\dfrac{\partial g_2}{\partial x} + 8\pi^4\dfrac{\partial}{\partial x}\left(\dfrac{q^2}{g_3^2}\right)\right) = -4\pi^2\mu_0\dfrac{\partial p}{\partial x} \\ y(x=1) = y_{\mathrm{b}} \equiv \left(\dfrac{H_{\mathrm{b}}}{q_{\mathrm{b}}}\right)^2 = \left(\dfrac{F_{\mathrm{b}}g_{3,\mathrm{b}}}{q_{\mathrm{b}}2\pi}\right)^2 \end{cases}, \tag{A.2}$$

where q_{b} and $g_{3,\mathrm{b}}$ indicate the values of q and g_3 at the plasma boundary ($x = 1$) and $F_{\mathrm{b}} = R_0 B_{\mathrm{t}}$. Equation (A.2) admits the following analytical solution:

$$y(x) = \mathrm{e}^{-\int_1^x A(u)\mathrm{d}u}\left(y_b + \int_1^x \mathrm{e}^{\int_1^x A(u)\mathrm{d}u}P(v)\,\mathrm{d}v\right), \tag{A.3}$$

with

$$A(x) = \frac{\frac{\partial g_2}{\partial x} + 8\pi^4\frac{\partial}{\partial x}\left(\frac{q^2}{g_3^2}\right)}{\frac{g_2}{2} + 8\pi^4\frac{q^2}{g_3}} \quad \text{and} \quad P(x) = -\frac{4\pi^2\mu_0\frac{\partial p}{\partial x}}{\frac{g_2}{2} + 8\pi^4\frac{q^2}{g_3}}. \tag{A.4}$$

$H(x) = q(x)\sqrt{y(x)}$ and FF' can be obtained by combining equation (A.1) with the definition of q, leading to

$$FF' = -\frac{\mu_0}{g_3}\frac{\partial p}{\partial \Psi} + \frac{1}{4\pi^2 g_3}\frac{\partial}{\partial V}\left(g_2\frac{H}{q}\right). \tag{A.5}$$

Finally, using the flux-surface averaged definition of the poloidal flux $\Psi(x)$

$$\Psi(x) = -\int_0^{V(x)}\frac{H}{q}\mathrm{d}V, \tag{A.6}$$

p' is then calculated as $p' = \partial p/\partial\Psi$.

A proper iteration scheme is needed to iterate the resolution of the 2D GSE (equation (1)) and 1D flux-surface averaged (equation (A.1)). For the ith iteration step, the 2D poloidal

flux distribution is known from the previous iteration (Ψ^{i-1}). For the first step ($i = 1$), Ψ^0 is initialized imposing a flat current density $J_{\phi,\mathrm{p}}$ calculated from a given plasma current I_p, which can be either set manually or initialized via ITER-based scaling laws (e.g. [88]). Then, the following operations are performed in the appearing order:

(a) calculate $x^i(\Psi^{i-1})$ from equation (4)
(b) calculate $V^i\left(\Psi^{i-1}\right)$, $g_2^i\left(\Psi^{i-1}\right)$ and $g_3^i\left(\Psi^{i-1}\right)$ from the 2D poloidal flux computed in the previous iteration (Ψ^{i-i})
(c) use V^i, g_2^i and g_3^i, $p(x)$ and $q(x)$ to calculate $y^i(x)$ (equation (A.3)) and $H^i(x)$,
(d) update $\Psi(x)$ (equation (A.6))
(e) calculate $\left(p'\right)^i$ and $\left(FF'\right)^i$
(f) repeat steps (c)–(e) until convergence on $\Psi_\mathrm{ax} = \Psi(x = 0)$ and the toroidal flux at plasma boundary $\Phi_\mathrm{b} = \int_0^{V_\mathrm{p}} H\,\mathrm{d}V$ is reached
(g) map the 1D profiles $\left(p'\right)^i$ and $\left(FF'\right)^i$ onto the 2D grid of $x^i(\Psi^{i-1})$ to calculate the new 2D distribution of $J^i_{\phi,\mathrm{p}}$
(h) solve the 2D GSE (equation (2)) with $J_\phi \equiv J^i_{\phi,\mathrm{p}}$ to update $\Psi^{i-1} \leftarrow \Psi^i$
(i) repeat all steps from (a) to (h) until convergence on the values $\Psi(r, z)$ on all the 2D plasma mesh nodes is reached.

An under-relaxation on g_2 and g_3 between the outer iterations (that is where V, g_2 and g_3 are updated on the previous flux profile) is recommended to ensure convergence and to mitigate the diverging effects of g_2 at the plasma boundary [25]. Note that within this iteration level, the plasma current I_p can be also used to constrain the equilibrium solution, such that

$$I_\mathrm{p} = \left(\frac{g_2 g_3 F}{8\pi^3 \mu_0 q}\right)_\mathrm{b}, \tag{A.7}$$

where the subscript 'b' indicates that g_2, g_3 q, and F are all computed at the plasma boundary.

The mathematical implementation of the model and the iteration scheme has been verified through code-to-code comparisons with the PLASMOD transport solver for several DEMO cases with varying major radius and aspect ratios. The results yielded relative errors in the L_2 norm sense of g_2, g_3, p', FF', V, Ψ and Φ profiles always below 10^{-3}.

A.2. Derivation of the Green's functions of the Grad–Shafranov elliptic operator

The coefficients $\mathcal{G}_{\Psi,k,i}$ and $\mathcal{G}_{\Psi,k,p}$ outlined in equation (9) are the Green's functions of the Grad–Shafranov elliptic operator and are calculated at all locations $k = (r_k, z_k)$ from the numerical solution $\Psi^{(i)}(r_k, z_k)$ of equation (2). These are obtained by 'enabling' each coil i separately. As a result, the current density $J_\phi^{(i)}(r, z)$ is defined as:

$$J_\phi^{(i)}(r,z) = \begin{cases} \dfrac{I_{\mathrm{c},i}}{A_i} & \forall\ (r,z) \in \mathcal{D}_{\mathrm{c},i} \\ 0 & \forall\ (r,z) \notin \mathcal{D}_{\mathrm{c},i} \end{cases}, \tag{A.8}$$

with A_i being the cross-section area of the coil i and $\mathcal{D}_i$ the enclosing space domain. Accordingly, the Green functions $\mathcal{G}_{\Psi,k,i}$ is calculated normalizing $\Psi^{(i)}(r_k, z_k)$ on the ith coil's current I_i (for this specific purpose set to one), leading to:

$$\mathcal{G}_{\Psi,k,i}(r_k, z_k) = \frac{\Psi^{(i)}(r_k, z_k)}{I_{\mathrm{c},i}}. \tag{A.9}$$

Note that, replacing the subscript 'i' with 'p' and setting $J_{\Phi,i} \equiv J_{\phi,p}\ \forall\ (r, z) \in \mathcal{D}_p$ ad zero elsewhere, the Green's functions associated with the plasma current are automatically obtained. The same logic can be applied to $B_r^{(i)}$ and $B_z^{(i)}$ to derive the field's Green's functions constants $\mathcal{G}_{B_r,k,i}$, $\mathcal{G}_{B_z,k,i}$, $\mathcal{G}_{B_r,k,p}$, and$\mathcal{G}_{B_z,k,p}$, recalling that $B_r = -\frac{1}{2\pi r}\frac{\partial \Psi}{\partial z}$ and $B_z = \frac{1}{2\pi r}\frac{\partial \Psi}{\partial r}$. In this case, the partial derivatives are calculated numerically in the FEM solver from the 2D distribution of Ψ.

If all toroidal currents are approximated by a set of current filaments (or loops), the Green's functions can be also calculated analytically from the Biot–Savart equation. Accordingly, $\mathcal{G}_{\Psi,k,i} = \frac{1}{I_{\mathrm{c},i}} \cdot \sum_{n=1}^{N_i} \mathcal{G}_{\Psi,k,n}(r_k, z_k, R_n, Z_n) \cdot I_{n,i}$ where R_n and Z_n are the radial and vertical coordinate of the current filament n within the coil i, $I_{n,i}$ is the current, $\mathcal{G}_{\Psi,k,n}$ is the Green's function coefficient calculated at the poloidal location (r_k, z_k), and N_i the total number of filaments of the coil i. The expressions of $\mathcal{G}_{\Psi,k,n}, \mathcal{G}_{B_r,k,n}$ and $\mathcal{G}_{B_z,k,n}$ can be found in [13, 16]. However, while the filamentary theory is valid for regions far from the current filament, singularities are found for $r_k \to R_n$ and $z_k \to Z_n$. The derivation of the Green's function from the FEM solution of the GSE avoids such a diverging behaviour and is therefore preferred for the coils' current resolution in the implemented FBE model.

The coefficients $\mathcal{G}_{F_z,j\to i}$ and $\mathcal{G}_{F_z,p\to i}$ (outlined in equation (11) to compute the vertical force $F_{z,i}$ acting on the coil i) are calculated resolving equation (2) for every coil pair (i, j) and (i, p). These read as:

$$\begin{aligned}\mathcal{G}_{F_z,j\to i} &= \frac{F_{z,j\to i}}{I_{\mathrm{c},i} \cdot I_{\mathrm{c},j}} \equiv -\frac{F_{z,i\to j}}{I_{\mathrm{c},i} \cdot I_{\mathrm{c},j}} \\ &= -\frac{1}{I_{\mathrm{c},i} \cdot I_{\mathrm{c},j}} \int_{\mathcal{D}_i} J_\phi^{(i,j)} \cdot B_r^{(i,j)} \cdot 2\pi r\,\mathrm{d}r\,\mathrm{d}z,\end{aligned} \tag{A.10}$$

with $F_{z,j\to i}$ being the vertical force exerted on the coil i from the coil j, $B_r^{(i,j)}$ the radial magnetic field distribution from the current density $J_\phi^{(i,j)}$ operated in the coil pair (i, j), given by:

$$J_\phi^{(i,j)}(r,z) = \begin{cases} \dfrac{I_{\mathrm{c},i}}{A_i} & \forall\ (r,z) \in \mathcal{D}_{\mathrm{c},i} \\ \dfrac{I_{\mathrm{c},j}}{A_j} & \forall\ (r,z) \in \mathcal{D}_{\mathrm{c},j} \\ 0 & \forall\ (r,z) \notin \mathcal{D}_{\mathrm{c},i} \wedge \forall (r,z) \notin \mathcal{D}_{\mathrm{c},j} \end{cases}. \tag{A.11}$$

Appendix B. PFC/CS currents, peak magnetic fields and vertical forces of the EU-DEMO 2017 baseline

Table 11 lists the full set of PF and CS coils currents, peak magnetic fields and vertical forces at the plasma BD, start-of-flat-top (SOF) and end-of-flat-top (EOF) calculated in the MIRA FBE solver (section 3.2.2) for the EU-DEMO 2017

Table 11. Evaluated BD, SOF and EOF PF/CS coils current, peak field and vertical forces configurations of the EU-DEMO 2017 baseline.

Parameter variable (unit)	BD	SOF	EOF	Type
Total current in coil CS3U $I_{c,CS3U}$ (MA)	+29.61	−3.41	−14.4	$\|TL\| \leqslant 29.61$
Total current in coil CS2U $I_{c,CS2U}$ (MA)	+29.61	+16.72	−29.0	$\|TL\| \leqslant 29.61$
Total current in coil CS1 $I_{c,CS1}$ (MA)	+59.71	−13.29	−59.71	$\|TL\| \leqslant 59.72$
Total current in coil CS2L $I_{c,CS2L}$ (MA)	+29.60	+20.36	−22.3	$\|TL\| \leqslant 29.6$
Total current in coil CS3L $I_{c,CS3L}$ (MA)	+24.94	−9.13	−25.5	$\|TL\| \leqslant 29.6$
Total current in coil PF1 $I_{c,PF1}$ (MA)	+13.68	+15.27	−0.6	$\|TL\| \leqslant 18.0$
Total current in coil PF2 $I_{c,PF2}$ (MA)	+3.06	−2.78	−4.8	$\|TL\| \leqslant 24.5$
Total current in coil PF3 $I_{c,PF3}$ (MA)	−1.75	−10.38	−9.1	$\|TL\| \leqslant 12.5$
Total current in coil PF4 $I_{c,PF4}$ (MA)	+3.11	+1.26	−1.8	$\|TL\| \leqslant 12.5$
Total current in coil PF5 $I_{c,PF5}$ (MA)	−1.88	−12.63	−11.5	$TL \leqslant \pm 24.5$
Total current in coil PF6 $I_{c,PF6}$ (MA)	+17.08	+25.64	+12.2	$TL \leqslant \pm 50.0$
Peak magnetic field in coil CS3U $B_{peak,CS3U}$ (T)	12.04	3.92	8.2	$TL \leqslant 13.7$
Peak magnetic field in coil CS2U $B_{peak,CS2U}$ (T)	12.35	5.31	10.6	$TL \leqslant 13.7$
Peak magnetic field in coil CS1 $B_{peak,CS1}$ (T)	12.46	4.87	11.1	$TL \leqslant 13.7$
Peak magnetic field in coil CS2L $B_{peak,CS2L}$ (T)	12.22	6.10	9.5	$TL \leqslant 13.7$
Peak magnetic field in coil CS3L $B_{peak,CS3L}$ (T)	10.95	5.08	8.7	$TL \leqslant 13.7$
Peak magnetic field in coil PF1 $B_{peak,PF1}$ (T)	5.70	5.60	1.1	$TL \leqslant 5.7$
Peak magnetic field in coil PF2 $B_{peak,PF2}$ (T)	0.86	1.22	1.70	$TL \leqslant 5.7$
Peak magnetic field in coil PF3 $B_{peak,PF3}$ (T)	0.69	4.06	3.56	$TL \leqslant 5.7$
Peak magnetic field in coil PF4 $B_{peak,PF4}$ (T)	1.09	0.70	0.91	$TL \leqslant 5.7$
Peak magnetic field in coil PF5 $B_{peak,PF5}$ (T)	0.60	3.83	3.48	$TL \leqslant 5.7$
Peak magnetic field in coil PF6 $B_{peak,PF6}$ (T)	4.20	5.51	2.54	$TL \leqslant 5.7$
Vertical force in coil PF1 $F_{z,PF1}$ (MN)	−430.82	−103.03	−11.09	$\|OL\| \leqslant 450$
Vertical force in coil PF2 $F_{z,PF2}$ (MN)	−24.80	−22.40	−80.52	$\|OL\| \leqslant 450$
Vertical force in coil PF3 $F_{z,PF3}$ (MN)	+14.53	+58.77	−43.28	$\|OL\| \leqslant 450$
Vertical force in coil PF4 $F_{z,PF4}$ (MN)	−1.47	−21.75	+30.95	$\|OL\| \leqslant 450$
Vertical force in coil PF5 $F_{z,PF5}$ (MN)	−16.43	+42.18	+155.81	$\|OL\| \leqslant 450$
Vertical force in coil PF6 $F_{z,PF1}$ (MN)	+356.97	+40.94	−233.28	$\|OL\| \leqslant 450$
Vertical separation force in CS stack $F^{sep}_{z,CS}$ (MN)	+102.02	+128.96	+181.50	$\|OL\| \leqslant 350$
Total vertical force in CS stack $F^{tot}_{z,CS}$ (MN)	+102.02	+4.94	+181.50	$\|OL\| \leqslant 300$

baseline. The column 'type' indicates whether a parameter is an operational limit (OL) or a technological limit (TL), with the value associated with its upper/lower limit or equality constraint reported therein.

ORCID iDs

F. Franza https://orcid.org/0000-0002-6950-0447
E. Fable https://orcid.org/0000-0001-5019-9685
I.A. Maione https://orcid.org/0000-0003-0224-9195

References

[1] Donné A.J.H. 2019 *Phil. Trans. R. Soc.* A **377** 20170432
[2] Federici G. *et al* 2018 *Fusion Eng. Des.* **136** 729–41
[3] Kovari M., Kemp R., Lux H., Knight P., Morris J. and Ward D.J. 2014 *Fusion Eng. Des.* **89** 3054–69
[4] Kovari M., Fox F., Harrington C., Kembleton R., Knight P., Lux H. and Morris J. 2016 *Fusion Eng. Des.* **104** 9–20
[5] Reux C. *et al* 2015 *Nucl. Fusion* **55** 073011
[6] Jaboulay J.-C., Li Puma A. and Arroyo J.M. 2013 *Fusion Eng. Des.* **88** 2336–42
[7] Li-Puma A., Jaboulay J.-C. and Martin B. 2014 *Fusion Eng. Des.* **89** 1195–200
[8] Dragojlovic Z., Raffray A.R., Najmabadi F., Kessel C., Waganer L., El-Guebaly L. and Bromberg L. 2010 *Fusion Eng. Des.* **85** 243–65
[9] Hong B.G., Lee D.W., Kim S.-K. and Kim Y. 2008 *Fusion Eng. Des.* **83** 1615–8
[10] Nakamura M., Kemp R., Utoh H., Ward D.J., Tobita K., Hiwatari R. and Federici G. 2012 *Fusion Eng. Des.* **87** 864–7
[11] Franza F., Boccaccini L.V., Fisher U., Gade P.V. and Heller R. 2015 *Fusion Eng. Des.* **98–99** 1767–70
[12] Franza F., Landman I.S. and Pestchanyi S. 2018 *Fusion Eng. Des.* **136** 309–13
[13] Franza F. 2019 Development and validation of a computational tool for fusion reactors' system analysis *PhD Thesis* Karlsruhe Institute of Technology (KIT) (https://publikationen.bibliothek.kit.edu/1000095873)
[14] Coleman M. and McIntosh S. 2019 *Fusion Eng. Des.* **139** 26–38
[15] Coleman M., Hörstensmeyer Y. and Cismondi F. 2019 *Fusion Eng. Des.* **141** 79–90
[16] Coleman M. and McIntosh S. 2020 *Fusion Eng. Des.* **154** 111544
[17] Federici G., Biel W., Gilbert M.R., Kemp R., Taylor N. and Wenninger R. 2017 *Nucl. Fusion* **57** 092002
[18] Wenninger R. *et al* 2017 *Nucl. Fusion* **57** 016011
[19] Zohm H. 2015 *Magnetohydrodynamic Stability of Tokamaks* (New York: Wiley)
[20] Villone F., Barbato L., Mastrostefano S. and Ventre S. 2013 *Plasma Phys. Control. Fusion* **55** 095008
[21] Hecht F. 2012 *J. Numer. Math.* **20** 251–66

[22] Albanese R., Ambrosino R., Castaldo A. and Loschiavo V.P. 2018 *Fusion Eng. Des.* **133** 163–72
[23] Johner J. 2011 *Fusion Sci. Technol.* **59** 308–49
[24] Fable E., Angioni C., Siccinio M. and Zohm H. 2018 *Fusion Eng. Des.* **130** 131–6
[25] Fable E., Angioni C., Ivanov A.A., Lackner K., Maj O., Yu S., Medvedev S., Pautasso G. and Pereverzev G. V. 2013 *Nucl. Fusion* **53** 033002
[26] Kessel C.E. *et al* 2009 *Nucl. Fusion* **49** 085034
[27] Koslowski H.R. 2006 *J. Fusion Sci. Technol.* **49** 147–54
[28] Zheng S.B., Wootton A.J. and Solano E.R. 1996 *Phys. Plasmas* **3** 1176
[29] Zani L., Mossang E., Tena M., Serries J.-P. and Cloez H. 2005 *IEEE Trans. Appl. Supercond.* **15** 3506–9
[30] Zani L. *et al* 2016 *IEEE Trans. Appl. Supercond.* **26** 1–5
[31] Tikhonov A.N. *et al* 1995 *Numerical Methods for the Solution of Ill-Posed Problems* (Dordrecht: Springer) (https://doi.org/10.1007/978-94-015-8480-7)
[32] Potra F.A. and Wright S.J. 2000 *J. Comput. Appl. Math.* **124** 281–302
[33] Atanasiu C.V., Günter S., Lackner K. and Miron I.G. 2004 *Phys. Plasmas* **11** 3510
[34] Mukhovatov V. *et al* 2003 *Plasma Phys. Control. Fusion* **45** A235
[35] Rivas J.C., Fable E., Kemp R., Lux H. and Wenninger R. 2018 *Fusion Eng. Des.* **136** 1125–9
[36] Pereverzev G. and Yushmanov Y. 2002 *ASTRA User Manual, IPP Report 5/98* (Max-Planck-Institute for Plasma Physics)
[37] Erba M., Aniel T., Basiuk V., Becoulet A. and Litaudon X. 1998 *Nucl. Fusion* **38** 1013
[38] Janky F., Fable E., Treutterer W. and Zohm H. 2017 *Fusion Eng. Des.* **123** 555–8
[39] Fable E., Wenninger R. and Kemp R. 2017 *Nucl. Fusion* **57** 022015
[40] Angioni C., Fable E., Greenwald M., Maslov M., Peeters A.G., Takenaga H. and Weisen H. 2009 *Plasma Phys. Control. Fusion* **51** 124017
[41] Greenwald M., Terry J.L., Wolfe S.M., Ejima S., Bell M.G., Kaye S.M. and Neilson G.H. 1988 *Nucl. Fusion* **28** 2199–207
[42] Zohm H. *et al* 2013 *Nucl. Fusion* **53** 073019
[43] Siccinio M., Federici G., Kembleton R., Lux H., Maviglia F. and Morris J. 2019 *Nucl. Fusion* **59** 106026
[44] Snyder P.B., Groebner R.J., Hughes J.W., Osborne T.H., Beurskens M., Leonard A.W., Wilson H.R. and Xu X.Q. 2011 *Nucl. Fusion* **51** 103016
[45] Troyon F., Gruber R., Saurenmann H., Semenzato S. and Succi S. 1994 *Plasma Phys. Control. Fusion* **26** 209–15
[46] Sauter O. *et al* 1997 *Phys. Plasmas* **4** 1654–64
[47] Bosch H.-S. and Hale G.M. 1992 *Nucl. Fusion* **32** 611
[48] Bosch H.-S. and Hale G.M. 1993 *Nucl. Fusion* **33** 1919
[49] Siccinio M., Fable E., Angioni C., Saarelma S., Scarabosio A. and Zohm H. 2018 *Nucl. Fusion* **58** 016032
[50] Friedberg J-P. 2007 *Plasma Physics and Fusion Energy* (Cambridge: Cambridge Unversity Press)
[51] Post D.E., Jensen R.V., Tarter C.B., Grasberger W.H. and Lokke W.A. 1977 *At. Data Nucl. Data Tables* **20** 397–439
[52] Lux H., Kemp R., Ward D.J. and Sertoli M. 2015 *Fusion Eng. Des.* **101** 42–51
[53] Sauter O., Angioni C. and Lin-Liu Y.R. 1999 *Phys. Plasmas* **6** 2834
[54] Sauter O., Angioni C. and Lin-Liu Y.R. 2002 *Phys. Plasmas* **9** 5140
[55] Zakharov L.E. 1979 *Plasma Physics and Controlled Nuclear Fusion Research* (Innsbruck, 23–30 August 1978) vol 1 (Vienna: IAEA) p 689 (https://www.iaea.org/publications/3309/plasma-physics-and-controlled-nuclear-fusion-research-1978-proceedings-of-an-international-conference-innsbruck-23-30-aug-1978)
[56] Takeda T. and Tokuda T. 1991 *J. Comput. Phys.* **93** 1–107
[57] Eich T. *et al* 2013 *Nucl. Fusion* **53** 093031
[58] Wenninger R.P. *et al* 2014 *Nucl. Fusion* **54** 114003
[59] Martin Y.R. and Takizuka T. (the ITPA CDBM H-mode Threshold Data Group) 2008 *J. Phys.: Conf. Ser.* **123** 012033
[60] Ambrosino G. *et al* 2005 *IEEE Control Syst. Mag.* **25** 76–92
[61] Ejima S., Callis R.W., Luxon J.L., Stambaugh R.D., Taylor T.S. and Wesley J.C. 1982 *Nucl. Fusion* **22** 1313–9
[62] Lewis E.E. and Miller W.M. 1984 *Computational Methods of Neutron Transport* (New York: Wiley)
[63] International Atomic Energy Agency, Nuclear Data Service 2021 FENDL-3.2: fusion evaluated nuclear data library ver.3.2 (https://nds.iaea.org/fendl/index.html) (last accessed on 08 November 2021)
[64] Fischer U., Angelone M., Bohm T., Kondo K., Konno C., Sawan M., Villari R. and Walker B. 2014 *Nucl. Data Sheets* **120** 230–4
[65] Maviglia F. *et al* 2017 *Fusion Eng. Des.* **124** 385–90
[66] Engle W.W. 1967 A user manual for ANISN, a one-dimensional discrete ordinates transport code with anisotropic scattering *Technical Report K-1693* Union Carbide Corporation
[67] Fischer U., Boccaccini L.V., Cismondi F., Coleman M., Day C., Hörstensmeyer Y., Moro F. and Pereslavtsev P. 2020 *Fusion Eng. Des.* **155** 111553
[68] Fischer U., Bachmann C., Palermo I., Pereslavtsev P. and Villari R. 2015 *Fusion Eng. Des.* **98–99** 2134–7
[69] Pereslavtsev P., Lu L., Fischer U. and Bitz O. 2014 *Fusion Eng. Des.* **89** 1979–83
[70] Hernández F.A., Pereslavtsev P., Kang Q., Norajitra P., Kiss B., Nádasi G. and Bitz O. 2017 *Fusion Eng. Des.* **124** 882–6
[71] Pereslavtsev P., Fischer U., Hernandez F. and Lu L. *Fusion Eng. Des.* **124** 910–4 2017
[72] Sackett S.J. 1975 Calculation of electromagnetic fields and forces in coil systems of arbitrary geometry *Report, UCRL-77244* (Lawrence Livermore Laboratory)
[73] Villone F. 2016 *Final Report on Deliverable PMI-5.3.3 (Toroidal Field Ripple Analysis) EFDA_D_2M97UY* (EUROfusion) (http://idm.euro-fusion.org/?uid=2M97UY)
[74] Duchateau J.-L., Hertout P., Saoutic B., Artaud J.-F., Zani L. and Reux C. 2014 *Fusion Eng. Des.* **89** 2606–20
[75] Bubelis E., Hering W. and Perez-Martin S. 2018 *Fusion Eng. Des.* **136** 367–71
[76] Martelli E., Giannetti F., Caruso G., Tarallo A., Polidori M., Barucca L. and Del Nevo A. 2018 *Fusion Eng. Des.* **136** 828–33
[77] Barucca L. *et al* 2021 *Fusion Eng. Des.* **169** 112504
[78] Wenninger R. 2017 *DEMO1 Reference Design—2017 March (EU DEMO1 2017)—PROCESS Full Output EFDA_D_2NDSKT* (EUROfusion) (https://idm.euro-fusion.org/?uid=2NDSKT)
[79] Federici G. *et al* 2019 *Nucl. Fusion* **59** 066013
[80] Federici G., Boccaccini L., Cismondi F., Gasparotto M., Poitevin Y. and Ricapito I. 2019 *Fusion Eng. Des.* **141** 30–42
[81] Hernandez F.H. *et al* 2019 *Fusion Sci. Technol.* **75** 352–64
[82] Hernandez F.H. *et al* 2020 *Fusion Eng. Des.* **157** 111614
[83] Del Nevo A. *et al* 2017 *Fusion Eng. Des.* **124** 682–6
[84] Martelli E. *et al* 2018 *Int. J. Energy Res.* **42** 27–52
[85] Corato V. *et al* 2018 *Fusion Eng. Des.* **136** 1597–604
[86] Zani L. *et al* 2019 *IEEE Trans. Appl. Supercond.* **29** 1–5
[87] Bachmann C. *et al* 2018 *Fusion Eng. Des.* **136** 87–95
[88] Wilson H.R. 1992 *Nucl. Fusion* **32** 257–63
[89] Moro F., Del Nevo A., Flammini D., Martelli E., Mozzillo R., Noce S. and Villari R. 2018 *Fusion Eng. Des.* **136** 1260–4
[90] Putvinskij S.V., Tubbing B.J.D., Eriksson L.-G. and Konovalov S.V. 1994 *Nucl. Fusion* **34** 495